

Personal Deployable Safety Restraint System (POD SRS)

A Thesis

Presented in Partial Fulfillment of the Requirements for the Degree
Master of Science in the Graduate School of The Ohio State
University

By

Shuting Wang, B.E.

Graduate Program in Mechanical Engineering

The Ohio State University

2020

Master's Examination Committee:

Dr. Marcelo Dapino, Advisor

Dr. Haijun Su

© Copyright by

Shuting Wang

2020

Abstract

The emergence of autonomous cars presents a new need for innovative smart restraint systems that modify or supplement the seat belts and airbags used in current vehicles. Because of the asymmetry of seat belts and instabilities of middle airbags between passengers, conventional restraint systems do not provide passengers with reliable protection in a side-impact crash.

This thesis presents concepts for smart, reconfigurable buckles and latches for self-deployed net safety restraint systems that complement existing seat belts. This thesis also covers materials selection and mechanism exploration.

Kevlar, as a high strength and high modulus fabric material with thermal stability, is suitable for protective high-impact restraint systems. Tensile tests have been done on plain-weave Kevlar 49 fabrics to determine its maximum strength. Bulk properties of Kevlar 49 were then calibrated and validated for further use in crash simulation software LS-DYNA using material card MAT234.

Reversible adhesion that involves arrays of nano hairs or mushroom-type extrusions is proven to have a high disengagement tensile strength. Commercially-available 3M™ Dual Lock™ products were chosen for benchmarking their dynamic tensile disengagement strength, dynamic shear strength and T-peel strength. Similar lab-made locking and unlocking mechanisms were then investigated. A metal pin dual lock was fabricated and was found to be three times stronger than plastic 3M™ Dual

Lock[™], although it was less durable. A smart latch with compliant mechanism was 3D printed and evaluated by a conceptual design tool called DAS-2D and validated utilizing compliant mechanism theory.

Acknowledgments

I would like to thank Prof. Marcelo Dapino for providing me an opportunity to work in the Smart Materials and Structures Laboratory. His support and help over the last two years helped me advance this project forward and deepened my understanding in research.

I would like to acknowledge Sheng Dong and Emily Nutwell from the Simulation Innovation and Modeling Center for their generous help on simulation. I would like to thank the members of the SMSL team and the Smart Vehicle Concepts Center. Specifically, I would like to thank Leon Headings, Venkata Siva Chillara and Yitong Zhou for step-by-step hands-on training of prototyping and testing. I would also like to thank Tommie Blackledge for proofreading this thesis.

A special thanks also extends to other SMSL team members Arun Ramanathan, Ismail Nas, Sai Siddhartha Vemula and Brad Losey for their support.

Vita

August 11, 1996 Born - Jiaxing, Zhejiang, China

June, 2018 B.E. Material Forming and Control
Engineering, Harbin Institute of
Technology, China

August, 2018 - present Graduate Research Associate,
The Ohio State University,
Columbus, OH.

Fields of Study

Major Field: Mechanical Engineering

Table of Contents

	Page
Abstract	ii
Acknowledgments	iv
Vita	v
List of Tables	ix
List of Figures	x
1. Introduction	1
1.1 Motivation	1
1.2 Problem Description	7
1.3 Thesis Organization	13
2. Background	15
2.1 Material Properties	15
2.1.1 Commonly Used Materials for Seat Belts	15
2.1.2 Woven Design of Fabrics	16
2.2 Reversible Adhesion	18
2.2.1 Adhesion Strength of Reversible Adhesion	18
2.3 Testing Standards	22
2.3.1 Testing Standard for Dry Fabrics – Tensile Test	23
2.3.2 Testing Standard for Hook and Loop – Shear Test	24
2.3.3 Testing Standard for Hook and Loop – T-peel Test	25
2.4 Modeling of Nonlinear Materials	26
2.4.1 Modeling of Kevlar	26
2.4.2 Kevlar in LS-DYNA	28

3.	Testing and Simulation Results	32
3.1	Dry Fabric Tensile Testing	32
3.2	Simulation Verification of Fabric Testing	37
3.3	Actuation by Coiled Fishing Line	47
4.	Characterization of Latching Mechanisms	50
4.1	Tests for 3M™ Dual Lock™	50
4.1.1	Disengagement Test	52
4.1.2	Shear Test	53
4.1.3	Peel Test	55
4.2	Metal Dual Lock	57
4.2.1	Steel Pin Lock Fabrication	57
4.2.2	Comparison of Metal and Plastic Dual Lock	61
4.2.3	Discussion	62
4.3	2D Bistable Compliant Mechanism Lock	62
4.3.1	Mushroom-type Compliant Mechanism	62
4.3.2	Ratchet Compliant Mechanism	64
4.3.3	Theoretical Equations of a 2D Compliant Mechanism	66
4.3.4	2D Compliant Mechanism in DAS-2D	77
5.	Summary and Future Work	80
5.1	Summary	80
5.2	Contributions	81
5.3	Future Work	81
	Appendices	83
A.	LS-DYNA Setup	83
A.1	Pre-processing	84
A.1.1	Mesh-ShapeM	84
A.1.2	Boundary Conditions	85
A.1.3	Material Type	87
A.1.4	Control	88
A.1.5	Hourglass Energy	88
A.1.6	Output	90
A.1.7	Run the Model	93
A.2	Post-processing	95

B.	MATLAB Calculations	99
B.1	Cross-sectional Area of Kevlar 49 Yarn	99
B.2	Potential Energy, Torque and Force Calculation	100
	Bibliography	103

List of Tables

Table	Page
2.1 Material properties used in LS-DYNA.	31
3.1 Properties of Kevlar 49.	32
3.2 Mechanical properties of aramid fibers.	35
3.3 Parameters used in MAT234 for Kevlar 49.	40
3.4 Optimal values of EKA and EKB for various strain rates.	45
3.5 Testing results and simulation.	47
4.1 3M™ Dual Lock™ stem density combinations.	51
4.2 Strength of 3M™ Dual Lock™ and hook and loop. [4]	52
4.3 Results of disengagement test of 250:250 3M™ Dual Lock™.	54
4.4 Comparison of experimental dynamic shear strength with literature. .	55
4.5 Result of shear test of 250:250 3M™ Dual Lock™.	57
4.6 Result of peel test of 250:250 3M™ Dual Lock™.	57
4.7 Laser cutting material comparison.	59
4.8 Result of pull test of metal pin lock.	61
4.9 Dimensions of slider-rocker mechanism.	69

List of Figures

Figure	Page
1.1 Effect of seat direction, seating position and seating angle in frontal collisions. [21]	1
1.2 Floating center-mounted airbags under side impact. [41]	2
1.3 Summary of recommended injury criteria for the SNPRM (Supplemental Notice of Proposed Rulemaking). [5]	3
1.4 Relative head center of gravity (CG) displacement using GHBMF FE model using seat arrangement A compared to cadaver test, (a) horizontal, and (b) vertical. [17]	5
1.5 Thorax measurement locations (three chest band (CB) levels). [11] .	6
1.6 Initial modulus of industrial filament yarns versus nylon and polyester. [4]	7
1.7 First concept design with deployable net.	9
1.8 Second concept design with smart buckle.	9
1.9 Third concept design with deployable net.	10
1.10 Coiled nylon 6,6 sewing thread (a) nontwisted, (b) after coiling by twist insertion, (c) a two-ply muscle, (d) braided two-ply muscle, and (e) mandrel coiled muscle. [14]	11
1.11 A textile woven from polyester, cotton, and silver-plated nylon yarn. [14]	11

1.12	(a) Woven fabric made from coiled fishing line, (b) stitches made by sewing the coiled fishing line into a polymer sheet, and (c) machine-knitted textile. [13]	12
1.13	Fabric woven from coiled fishing line (extending vertically). [24]	12
1.14	Force versus temperature of a wire-wrapped artificial muscle made by coiling fishing line. [15]	13
2.1	Seat belt tensile test. [28]	16
2.2	(a) Schematic view of matt, twill and combined weaves; (b) breaking strength of seat belts with different material structure; and (c) elongation of the seat belt samples with different material structures where N represents polyamide (nylon), P for polyester, T for 2/2 twill, M for 2/2 matt and C for 2/2matt-plain combo. [46]	17
2.3	(a) Wing-locking device of the beetle, (b,c) SEM images of microtrichia on the cuticular surface with two different magnifications, and (d) schematic of folding and unfolding states of the wing-locking device. [31]	19
2.4	Concept and fabrication of the bio-inspired microneedle adhesive. [42]	19
2.5	Shape memory reversible bonding. [27]	20
2.6	Nanoadhesive inspired by gecko feet. [23]	20
2.7	SEM and optical images of dry adhesive tips. [34]	21
2.8	(b - d) SEM images of mushroom-shaped pillars with different aspect ratios: (b) 2:1, (c) 3:1, and (d) 6:1. [40]	21
2.9	(a) Illustration of engaging pillar-to-pillar contact and adhesion measurement, (b–d) Three possible interlocking modes: (b) interdigitation, (c) indenting, and d) interweaving. [3]	22
2.10	(a) Kevlar cloth specimen following a tensile SHB test, (b) Kevlar yarn specimen following a tensile SHB test, and (c) stress strain curve from a tensile SHB test on Kevlar cloth. [12]	23

2.11	(a) Tensile test on Kevlar 29 in warp and weft direction testing, and (b) tensile specimens after tensile test. [39]	24
2.12	Shear direction definitions from D5169	25
2.13	T-peel direction definitions from D5170.	26
2.14	Fabric level, yarn level, and filament level model. [19]	27
2.15	Kevlar modeled in (a) yarn level. [9], and (b) filament level. [30]	27
2.16	Representative volume cell (RVC) of fabric. [19]	28
2.17	Ballistic simulation results compared with experiments on Kevlar fabric. [1]	29
2.18	Kevlar 49 warp direction uniaxial stress-strain results. [45]	30
2.19	Three-element viscoelastic model. [16]	30
3.1	Kevlar samples (a) after tensile test, (b) after extended tensile test.	33
3.2	Kevlar 29 tensile test of 8 by 1 inch. [10]	34
3.3	Force-strain curve of Kevlar 49 - one-inch wide.	34
3.4	Kevlar tensile test load-crosshead curve, load-elongation curve and stress-strain curve.	36
3.5	Trellis mechanism (a) initial state, (b) slightly stretched in bias direction, and (c) stretched to locking. [16]	39
3.6	Measurement of volume of Kevlar samples.	43
3.7	Ratio of warp yarns and weft yarns.	43
3.8	Lateral contact factor α as a function of braid angle θ . [16]	45
3.9	Kevlar 49 force-displacement curve in LS-DYNA for the tensile test.	47
3.10	Fabrication of self-coiling fishing line, (a) not twisted, and (b) twisted.	48

3.11	Fabrication of mandrel-coiling fishing line, (a) before heat treatment, and (b) after heat treatment.	49
4.1	3M™ Dual Lock™ stripes and type 170, 250 and 400.	50
4.2	Sample arrangement and disengagement test fixture.	53
4.3	Samples for the shear test.	56
4.4	(a-c) T-peel test sequence, and (d-f) disengagement test sequence. . .	56
4.5	Layers of unaligned pin lock.	58
4.6	Initial steel pin lock fabrication process: (a) insert pins into the foam, (b) fill resin and then rubber in the gaps of foam wall and cure, and (c) engage pins.	58
4.7	Steel pin lock fabrication process (a) prepare pin and cardboard, (b) insert pin into cardboard and foam, and (c) fill resin in the gaps of cardboard and cure.	60
4.8	Steel pin lock with contact area of (a) 1 by 1 inch, (b) 0.5 by 0.5 inch, and (c) 1 by 0.5 inch.	60
4.9	First design of four-bar linkage with modified sharp edges.	62
4.10	Physical bistable latch.	63
4.11	Physical symmetric bistable latch.	64
4.12	Second design of four-bar linkage with modified ratchet and teeth (a) ratchet, and (b) two rows of teeth.	65
4.13	Physical ratchet latch.	65
4.14	Modified ratchet latch.	66
4.15	Short-beam pseudo rigid body illustration and physical latch in (a) stable position, also the initial position, (b) instable position, and (c) second stable position after snap-through.	67

4.16	Slider rocker mechanism abstraction: four-torsional-spring assumption.	67
4.17	(a) Initial angle position, and (b) vector loop.	68
4.18	Instance center of different links, denoted as I_{ij} , $i, j = 1, 2, 3, 4$	70
4.19	Potential energy (V) versus θ_3 and torque (T) on L_3 versus θ_3 when (a) $k_1 = 26.60$ Nm/rad, (b) $k_1 = 266$ Nm/rad, and (c) $k_1 = 2660$ Nm/rad.	73
4.20	Potential energy (V) versus θ_3 - varying k_1	74
4.21	Potential energy (V) versus θ_3 - varying k_3	74
4.22	Potential energy (V) versus θ_3 - varying k_4	75
4.23	Slider rocker mechanism abstraction: one-torsional-spring assumption.	76
4.24	Potential energy (V) versus θ_3 and torque (T) on L_3 versus θ_3 - one- spring assumption.	76
4.25	Force (F) vs θ_3	77
4.26	Potential energy (V) versus θ_3 and torque (T) on L_3 versus θ_3 - one- spring assumption.	78
4.27	Four-bar linkage bistable model (a) potential energy and torque, and (b) deformed position.	79
4.28	Four-bar linkage bistable model - undeformed position.	79
4.29	Bistable model in (a) stable position 1, also the initial position, (b) instable position, and (c) second stable position after snap-through. .	79
A.1	Select element type and specify geometry	84
A.2	Remesh	85
A.3	Create a fixed boundary	86
A.4	Create a displacement boundary	86

A.5	Define a load curve	87
A.6	MAT234 for Kevlar fabric	88
A.7	Define termination time	89
A.8	Define timestpe	89
A.9	Hourglass control	90
A.10	Define database outputs	91
A.11	Define database d3plot	91
A.12	Define database extent binary	91
A.13	Define coordinate vector	92
A.14	Define *SECTION_SHELL	92
A.15	Model checking	93
A.16	Start LS-DYNA Solver	94
A.17	Select number of CPU utilized	94
A.18	Open the binary plot	96
A.19	Check energy ratio	96
A.20	Plot resultant force	97
A.21	Plot history data – x displacement of the moving end	98

Chapter 1: Introduction

1.1 Motivation

There is a need to develop new vehicle safety restraint systems that are capable of protecting occupants during impacts from different directions and other difficult loading conditions. Future autonomous vehicles will create further restraint needs associated with reconfigurable seating positions.

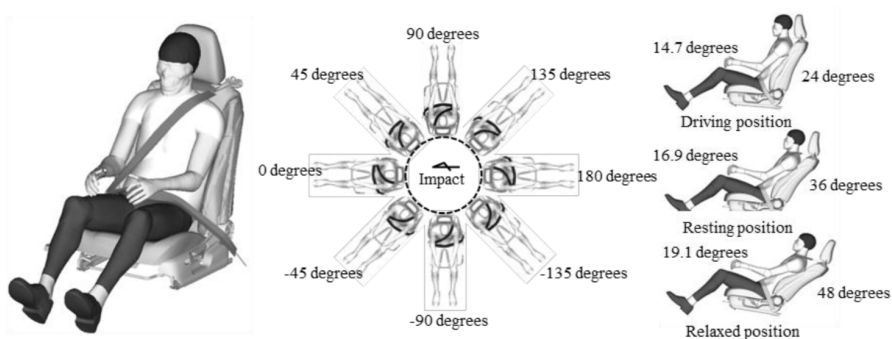


Figure 1.1: Effect of seat direction, seating position and seating angle in frontal collisions. [21]

Kitagawa et al. [21] investigated the effect of seat direction (forward, rearward and lateral facing in 45 degree increments), seating position (driving position, resting

position and relaxed position) and seating angle on post-mortem human subjects (PMHS) in front seats with or without seat belts to simulate frontal collisions (see Figure 1.1). A new restraint system should be able to protect occupants in the most vulnerable seating position.

Apart from the need for a new restraint system, three-point seat belts are insufficient in a side-impact collision scenario. Center-mounted airbags are ineffective because they float when deployed. Tests of center-mounted airbags under side impacts shown in Figure 1.2 reveal the problem.

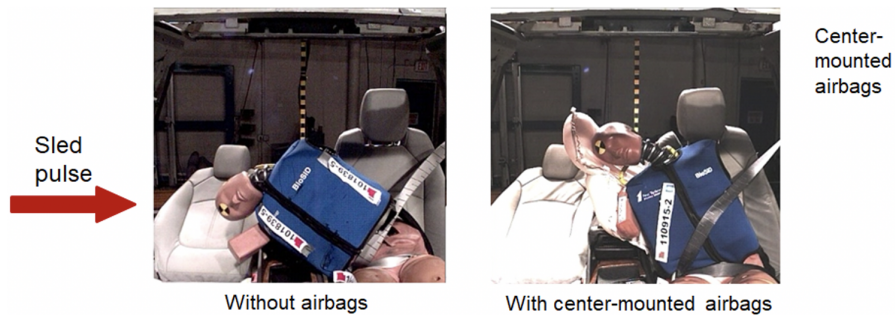


Figure 1.2: Floating center-mounted airbags under side impact. [41]

Three most common human body parts that are investigated in frontal, side, and rear-side impact collisions are the head, neck, and chest. Head displacement and acceleration data are exported from the simulation to assess injury severity. Chest deflection and compression are normally measured by choosing chest band levels.

To evaluate occupant safety in a restraint system, injury criteria (head, neck and torso) developed by Eppinger et al. [5] are commonly used, as shown in Figure 1.3. Prasad et al. [33] concluded that the data on which these criteria are built were first

Recommended Criteria	Large Male	Mid-Sized Male	Small Female	6 YO Child	3 YO Child	1 YO Infant
Head Criteria: HIC (15 msec)	700	700	700	700	570	390
Neck Criteria: SNPRM Nij	1.0	1.0	1.0	1.0	1.0	1.0
Critical Intercept Values						
Tension and Compression (N)	5440	4500	3370	2800	2120	1465
Flexion (Nm)	415	310	155	93	68	43
Extension (Nm)	166	125	62	39	27	17
Thoracic Criteria						
1. Chest Acceleration (g)	55	60	60	60	55	50
2. Chest Deflection (mm)	70 (2.8 in)	63 (2.5 in)	52 (2.0 in)	40 (1.6 in)	34 (1.4 in)	30 (1.2 in)
Lower Ext. Criteria:						
Femur Load (kN)	12.7	10.0	6.8	NA	NA	NA

Figure 1.3: Summary of recommended injury criteria for the SNPRM (Supplemental Notice of Proposed Rulemaking). [5]

developed in the 1980s and that there was little change in head and chest injury criteria.

Injury severity can be measured by head injury with Head Injury Criteria (HIC),

$$HIC = \max\left(\frac{1}{t_2 - t_1} \int_{t_1}^{t_2} a(t) dx\right)^{2.5} (t_2 - t_1), \quad (1.1)$$

where t_2 and t_1 are any two arbitrary times during the acceleration pulse.

In 1986, the time interval over which HIC [20] was calculated was limited to 36 msec. The current Federal Motor Vehicle Safety Standard (FMVSS) No. 208 frontal protection standard sets the critical value of HIC at 1000 for the mid-sized male dummy using a 36 msec maximum time interval.

Injury severity can be measured by neck injury with three neck injury criteria. The first Neck Injury Criterion (NIC) was determined by Bostrom et al. [2], which used the relative velocity of head acceleration,

$$NIC = 0.2a_{rel} + v_{rel}^2 < 15 \frac{m^2}{s^2}. \quad (1.2)$$

The threshold is 15. The normalized neck injury criteria brought up by Eppinger et al. [5], called “ N_{ij} ,” establishes critical limits for all four possible modes of neck loading; tension or compression combined with either flexion (forward) or extension (rearward) bending moment. The N_{ij} is defined as the sum of the normalized loads and moments, i.e.,

$$N_{ij} = \frac{F_Z}{F_{int}} + \frac{M_Y}{M_{int}}. \quad (1.3)$$

where F_Z is the axial load, F_{int} is the critical intercept value of load used for normalization, M_Y is the flexion/extension bending moment, and M_{int} is the critical intercept value for moment used for normalization [2].

The third criterion is called the N_{km} criterion [36]. This criterion considers horizontal shear force F_x and bending moment in the sagittal plane at the occipital condyle,

$$N_{km} = \frac{F_x}{F_{int}} + \frac{M_y}{M_{int}}, \quad (1.4)$$

Chest injury severity can be defined by Combined Thoracic Index (CTI) [2],

$$CTI = \frac{A_{max}}{A_{int}} + \frac{D_{max}}{D_{int}}, \quad (1.5)$$

where A_{max} and D_{max} are the maximum observed acceleration and deflection, and A_{int} and D_{int} are the corresponding maximum allowable intercept values.

Hassan et al. [17] investigated the impact of seat belt, headrest and seat stiffness on occupant response in rear-end collisions, using GHBM (Global Human Body Models

Consortium) 50th percentile male FE model. Head displacement was measured both horizontally and vertically. It can be seen from Figure 1.4 that the maximum head displacement occurs within 200 milliseconds, which means the deployment time of the restraint system is critical to resist a 200 millimeter displacement. However, existing front center airbags did not provide sufficient resistance to the head.

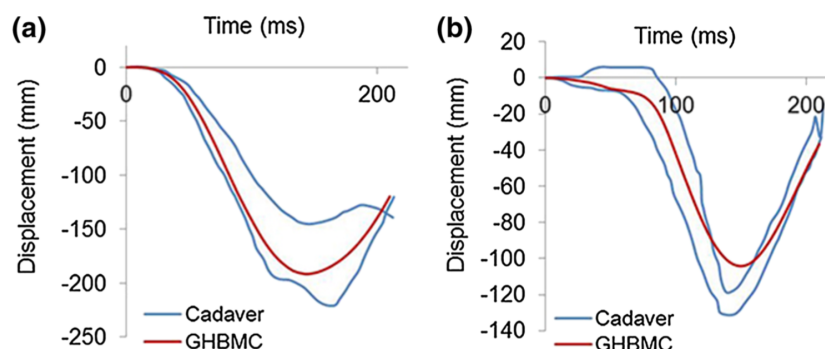


Figure 1.4: Relative head center of gravity (CG) displacement using GHBMC FE model using seat arrangement A compared to cadaver test, (a) horizontal, and (b) vertical. [17]

Gierczycka et al. [11] studied side impacts on thorax responses. Three chest band levels and an additional location corresponding to a middle chest band were measured to collect full chest deflection. Spine kinematics were also tracked. Three locations of chest band levels can be seen in Figure 1.5. Zaseck et al. [43] also chose chest band levels to investigate the influence of rib fracture on chest deflection and chest compression of a GHBMC-50O model.

Current three-point seat belts made of nylon can be less effective when autonomous driving becomes more common. Passengers in the car including the driver, though

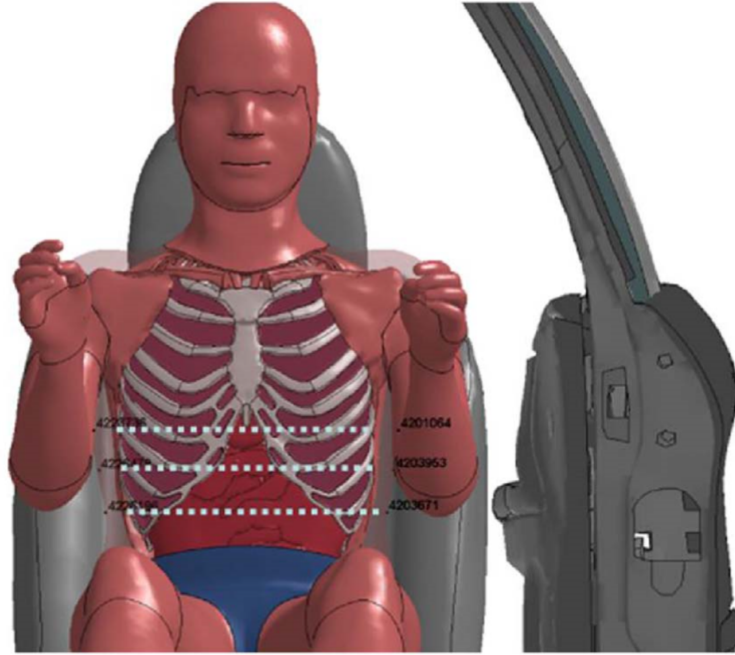


Figure 1.5: Thorax measurement locations (three chest band (CB) levels). [11]

no drivers might exist when fully driverless car comes to reality, have more freedom to utilize the time and space during the ride such as sitting or having a meeting. The seat belts may need to be supplemented by a novel restraint system made of stronger materials than nylon to deal with situations with higher safety risks. Kevlar, as a high strength and high modulus fabric material, is known for its application in body armor. Given that high impact is created when a car crash occurs, the high energy absorption capabilities of Kevlar make it an excellent candidate for restraint systems. The exceptional thermal stability of Kevlar also exceeds industrial nylon or polyester, retaining its tensile strength during 100 °F to 400 °F conditions (see Figure 1.6). In Figure 1.6, gpd means "grams per denier" and $1 \text{ tex} = 9 \text{ denier}$. Kevlar also has

excellent strength to weight ratio [25], which is crucial in weight reduction while maintaining high strength as part of the restraint system.

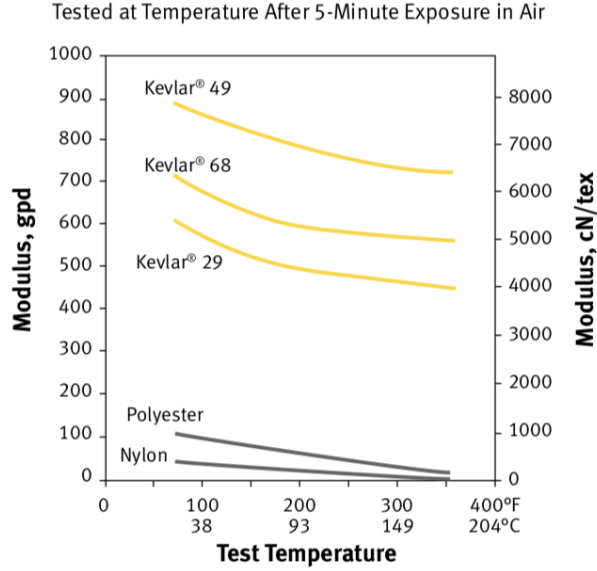


Figure 1.6: Initial modulus of industrial filament yarns versus nylon and polyester. [4]

1.2 Problem Description

The objective of this study is to investigate smart reconfigurable buckles that are able to attach one restraint component to an arbitrary location on a second restraint component. A smart buckle should provide the required strength to restrain an occupant yet be easily released when needed. The materials and design of the smart buckle should resist fatigue for everyday use and endure high loading in a crash. Specifically, this study will develop an understanding of different methods for creating mechanical interlocking between two restraints. This will be achieved

by investigating existing and bio-inspired approaches to latching, developing new concepts, and evaluating concepts through simplified modeling and calculations as well as fabricating and testing proof-of-concept coupon samples.

Due to the lack of regulations on injury criteria and strength requirements of restraint systems, the current work is a comparative study. Also, the complexities of this project make it a long-term project and as such, further investigations beyond this research will be required.

In this circumstance, the objectives of this study are to develop new latch and buckle designs for a new class of smart restraint systems; select candidate materials for a conceptual restraining net and calibrate the material properties in LS-DYNA; test existing and bio-inspired approaches to latching; and fabricate and test proof-of-concept coupon samples.

The concept designs of smart buckle and smart latch are shown in Figures 1.7, 1.8 and 1.9.

The first concept design will deploy a net from a containment inside the seat using a deployed telescopic post. The net is installed on the shoulder that is unrestrained by the seat belt. The tip of the telescopic post will try to attach to a D-ring on the car wall or an anchor on the seat.

The second concept design involves a smart buckle on the seat belt and another belt will deploy from the top of the seat and attach to the buckle in the middle of the seat belt. The smart buckle can also be used in combination with the deployed net from the first concept design.

The third concept design changes the deployment method, instead of an intrusive telescopic post, posts are installed inside the headrest which deploy using the same

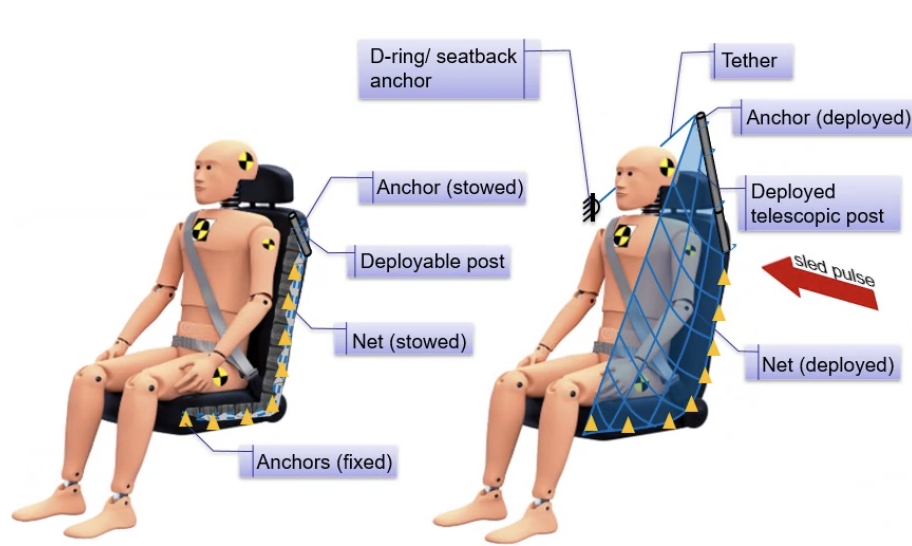


Figure 1.7: First concept design with deployable net.

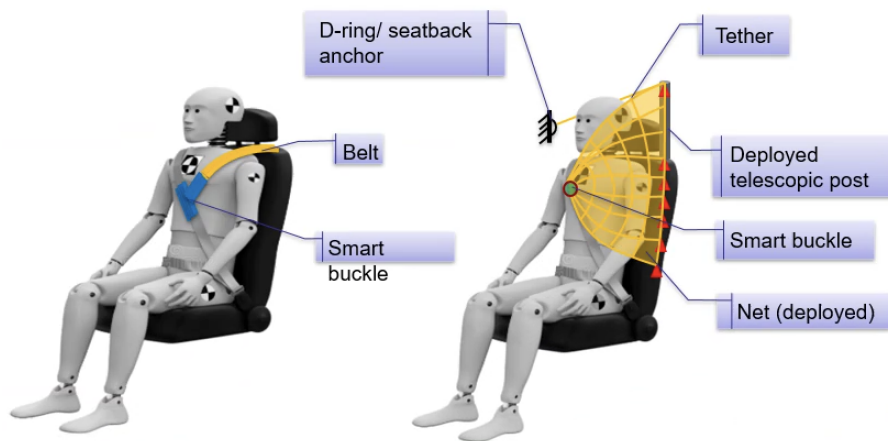


Figure 1.8: Second concept design with smart buckle.

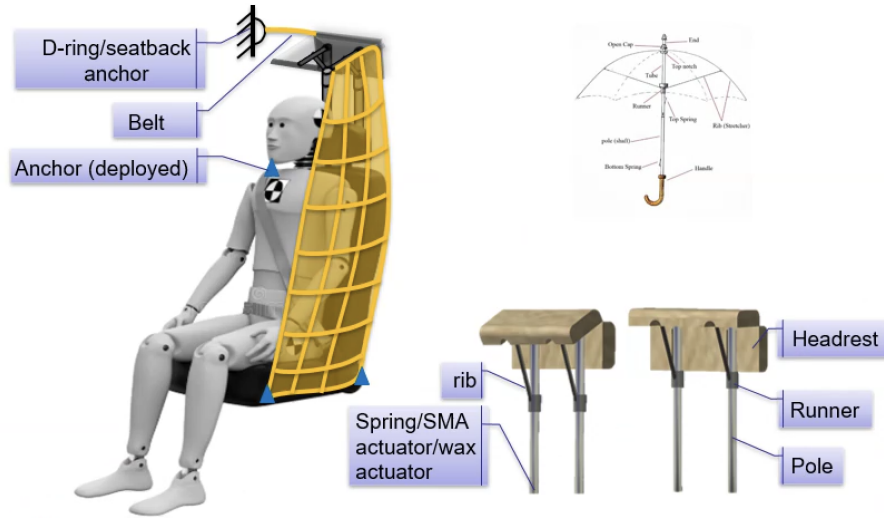


Figure 1.9: Third concept design with deployable net.

mechanism as an umbrella. The actuation of the post can be spring, shape memory alloy or coiled fishing line. This thesis conducts fundamental testing and design of materials and latch design involved.

Coiled fishing lines were presented by Haines et al. [14]. The inexpensive polymer fibers used for fishing line can be transformed to scalable and nonhysteretic actuators by twist insertion. Figure 1.10 shows the muscle and precursor structures using nylon 6,6 monofilament sewing thread. Haines et al. [13] formed smart textiles using traditional textile fabrication methods (Figures 1.11 and 1.12).

Coiled fishing line can also be integrated with fabrics as a smart fabric for a restraint net. Madden et al. [24] made a woven fabric from coiled nylon threads, Figure 1.13. Haines [15] proposed a closed-loop temperature control of nylon muscles by electrothermal heating, Figure 1.14. A wire-wrapped artificial muscle under this

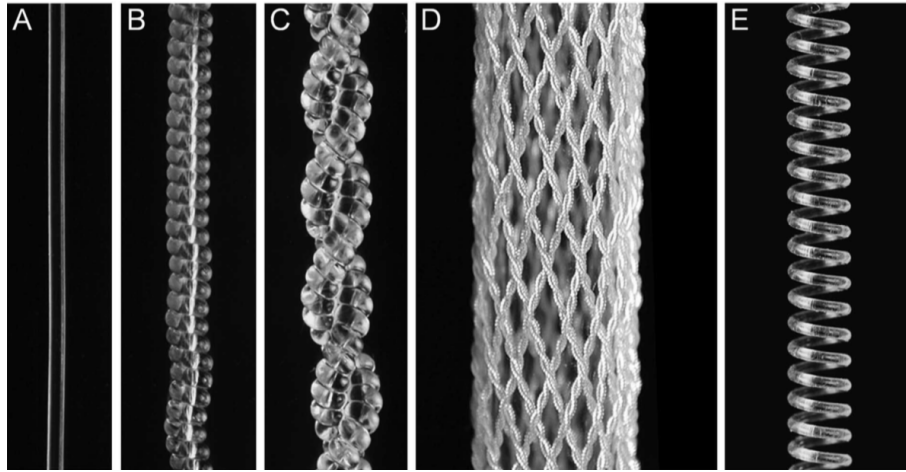


Figure 1.10: Coiled nylon 6,6 sewing thread (a) nontwisted, (b) after coiling by twist insertion, (c) a two-ply muscle, (d) braided two-ply muscle, and (e) mandrel coiled muscle. [14]

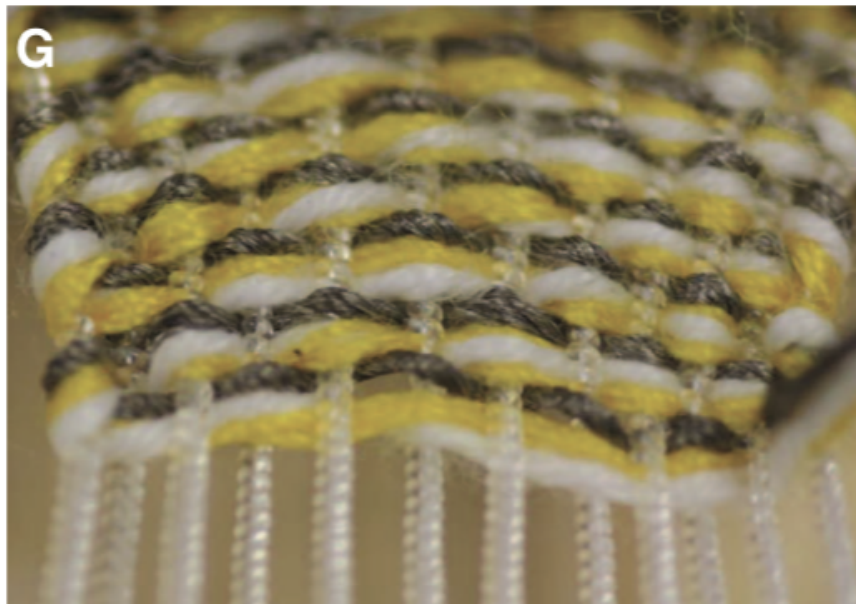


Figure 1.11: A textile woven from polyester, cotton, and silver-plated nylon yarn. [14]

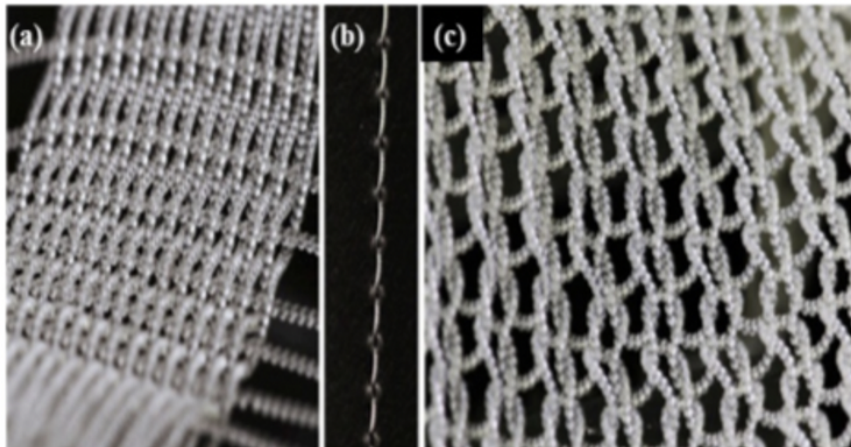


Figure 1.12: (a) Woven fabric made from coiled fishing line, (b) stitches made by sewing the coiled fishing line into a polymer sheet, and (c) machine-knitted textile. [13]



Figure 1.13: Fabric woven from coiled fishing line (extending vertically). [24]

control method is able to provide overheat protection and artificial muscle function over a temperature range of 0 °C to 180 °C.

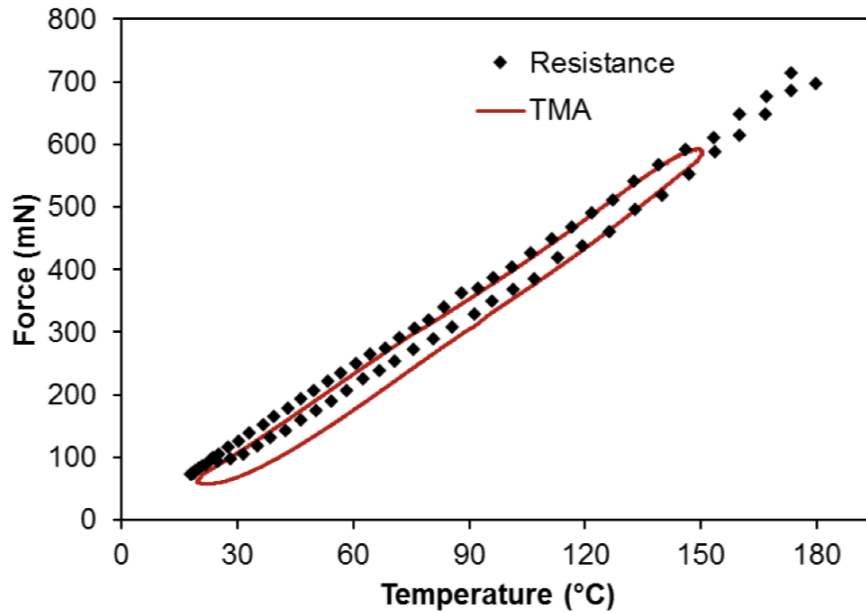


Figure 1.14: Force versus temperature of a wire-wrapped artificial muscle made by coiling fishing line. [15]

1.3 Thesis Organization

This thesis presents simulation and testing of Kevlar fabrics, design and fabrication of smart latches. The discussions of these topics are covered in 3 chapters. Chapter 2 reviews applications of reversible adhesion, actuation of fishing lines and the testing standards for dry fabrics and hook-and-loop fasteners. Chapter 3 summarizes results of tensile testing of Kevlar 49 fabrics, and also disengagement tests, shear tests and T-peel tests of dual locks. Chapter 4 shows new designs and fabrication of

metal and plastic latches. Concluding remarks in conjunction with future work are presented in Chapter 5.

Chapter 2: Background

2.1 Material Properties

2.1.1 Commonly Used Materials for Seat Belts

Materials that are commonly used for seat belts are polyester fibers such as polyamide 6 (PA 6), polyamide 66 (PA 66), and polyethylene terephthalate (PET) [5]. These polyester fibers have high strength and rigidity to prevent inertial movement. Nylon is used for its low friction and wear.

Little research was disclosed with regard to tensile tests of the materials of seat belts, such as polyester and nylon. Muszyński et al. [28] tested the seat belt strap in a child safety seat. Three narrow and five wide seat belt strap samples were tested, with 25.4 mm by 1.56 mm and 38.6 mm by 1.23 mm cross-sections respectively. The test specimens were subjected to quasi-static axial tensioning, which was increased until the breaking point was reached. The piston of the tensile-testing machine moved at a rate of 100 mm/min, shown in Figure 2.1.



Figure 2.1: Seat belt tensile test. [28]

2.1.2 Woven Design of Fabrics

Apart from materials selection, woven design and areal density of fabric also play a role in the performance of seat belts. Matt weave design is better than twill / plain-matt combination weaves, seen in Figure 2.2. In terms of the areal density of fabrics, the higher the density, the higher the breaking strength. The optimum structure is PNT [28]. The effect of weave design for the net used in the restraint system can be studied after the structure of the restraint system is determined. As of now, plain weave fabrics are considered.

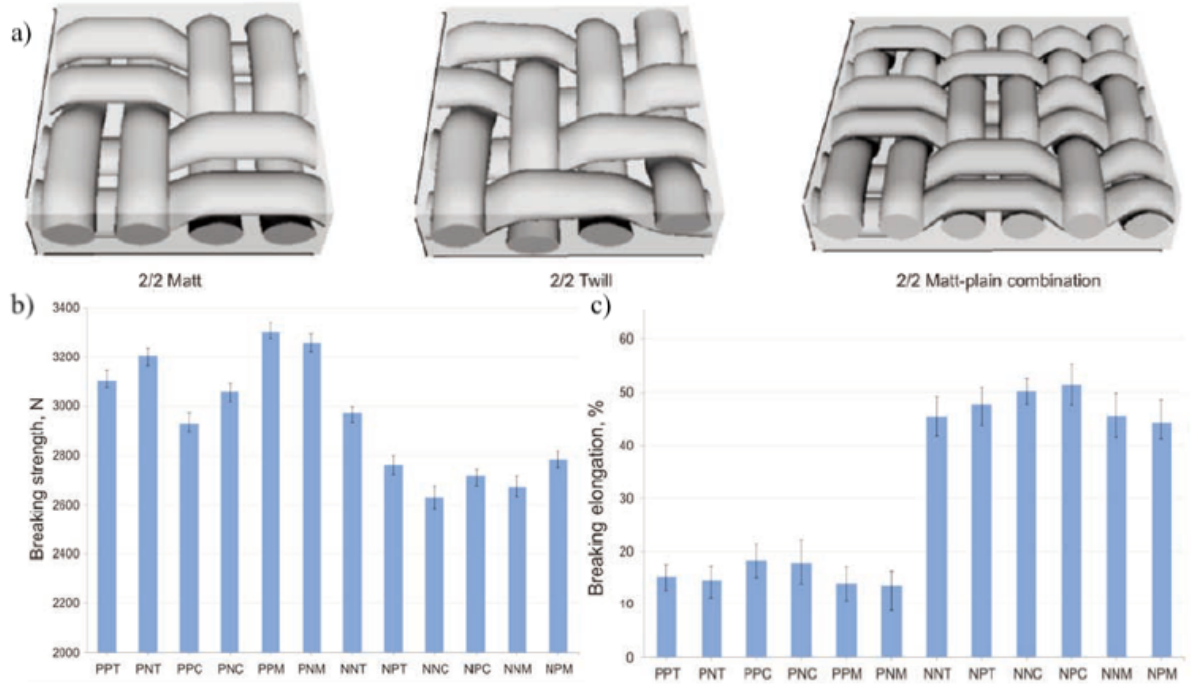


Figure 2.2: (a) Schematic view of matt, twill and combined weaves; (b) breaking strength of seat belts with different material structure; and (c) elongation of the seat belt samples with different material structures where N represents polyamide (nylon), P for polyester, T for 2/2 twill, M for 2/2 matt and C for 2/2matt-plain combo. [46]

2.2 Reversible Adhesion

2.2.1 Adhesion Strength of Reversible Adhesion

Micro or nano pillar arrays are extensively investigated to represent the microstructure of gecko feet and beetle wings, which exhibit strong adhesion strength. Known materials for pillar arrays include high-aspect-ratio shape memory polymers (SMPs) (see Figure 2.5), identical random nanowires and complementary ripples. Gecko-foot-mimetic nanopillar arrays combined with a mussel-adhesive-protein-mimetic polymer invented by Lee et al. will provide strong (90 kPa) but temporary adhesion force in both dry and wet conditions [23] (see Figure 2.6). Interweaved high-aspect-ratio shape-memory polymer (SMP) pillar arrays present about 540 kPa dry adhesion force in the normal direction and 720 kPa in the shear direction based on buckling and interlocking mechanism [3]. The shear adhesion of interlocked nanowires and pillars is much larger than the normal adhesion. Beetle-inspired high density micro- or nanohairs [31] (see Figure 2.3) made of polyurethane-based materials can achieve maximum shear locking force of 400 kPa [13, 31]. Such bioinspired adhesives even outweigh the adhesion strength of gecko feet.

Similarly, microscale architectures made of polyurethane acrylate (PUA) with protruding tips on their cylindrical stems are proved to have maximum adhesion strengths of 775 ± 64 kPa and 447 ± 71 kPa in the shear and normal direction respectively [37]. Biphasic microneedle (MN) array adhesive interlocks with tissue through swellable microneedle tips (see Figure 2.4). Adhesion strength reaches 14 kPa after 10 minutes [5]. Michal et al. (2016) constructed a lap joint by bonding two glass slides together. Shear stress required to break lap joints is above 1 MPa and the top slide will rotate to generate a slight bend in the joint[8]. An electrical surface fastener

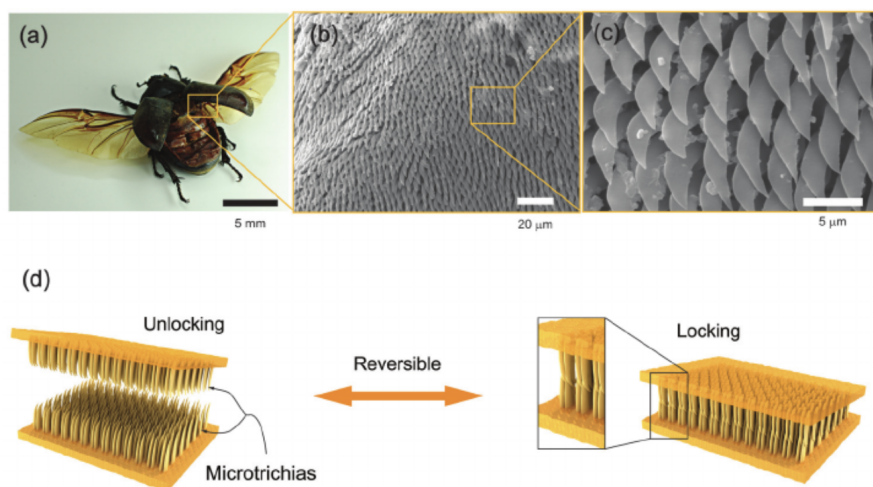


Figure 2.3: (a) Wing-locking device of the beetle, (b,c) SEM images of microtrichia on the cuticular surface with two different magnifications, and (d) schematic of folding and unfolding states of the wing-locking device. [31]

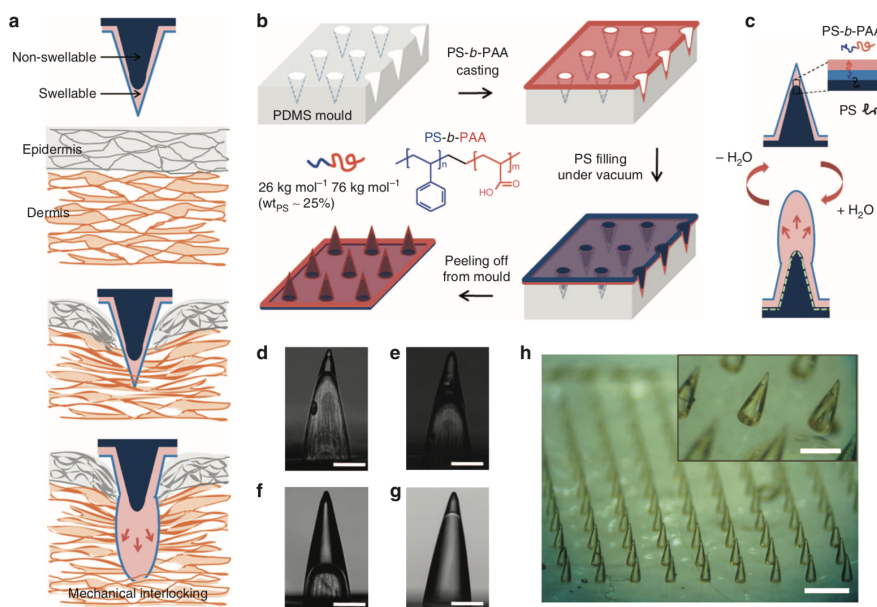


Figure 2.4: Concept and fabrication of the bio-inspired microneedle adhesive. [42]

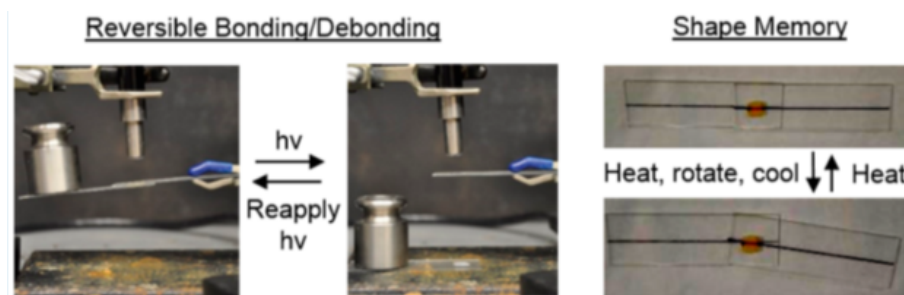


Figure 2.5: Shape memory reversible bonding. [27]

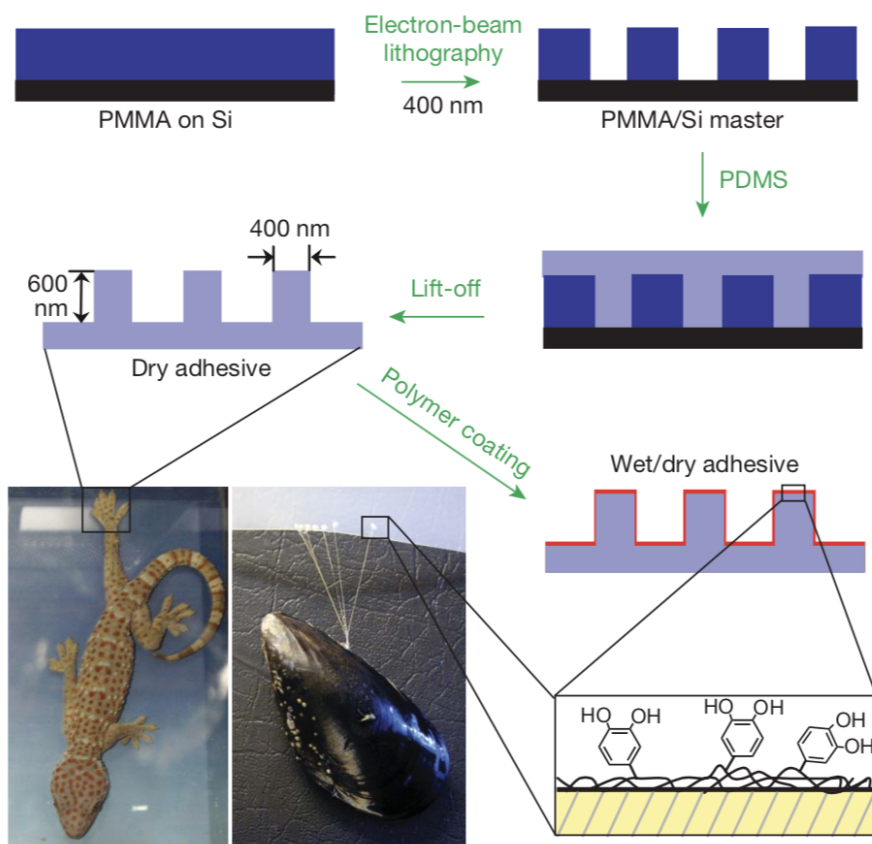


Figure 2.6: Nanoadhesive inspired by gecko feet. [23]

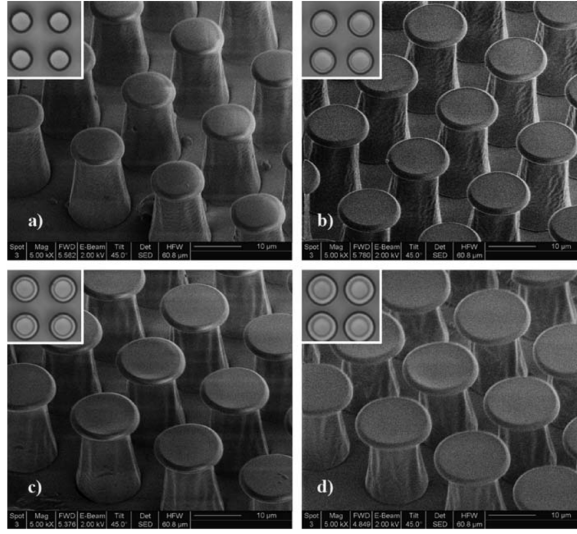


Figure 2.7: SEM and optical images of dry adhesive tips. [34]

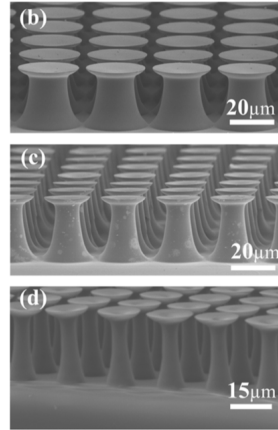


Figure 2.8: (b - d) SEM images of mushroom-shaped pillars with different aspect ratios: (b) 2:1, (c) 3:1, and (d) 6:1. [40]

based on copper/polystyrene core/shell nanowire arrays exhibits high macroscopic adhesion strength (444 kPa) [32]. Various derivatives (e.g., mushroom tips [35, 40] and pyramid shapes) of pillar arrays (see example Figure 2.9) also show promising applications for reversible adhesions. Figures 2.7 and 2.8 are example SEM images of mushroom extrusions of different aspect ratios.

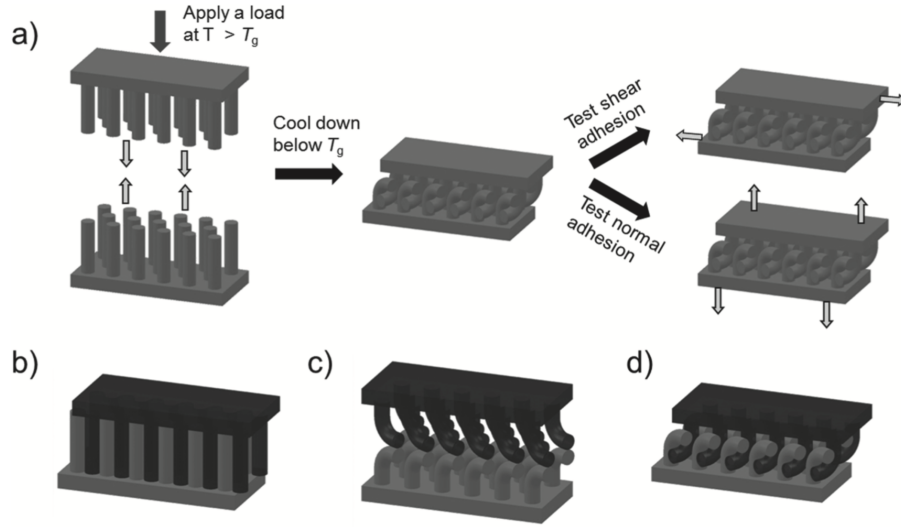


Figure 2.9: (a) Illustration of engaging pillar-to-pillar contact and adhesion measurement, (b–d) Three possible interlocking modes: (b) interdigititation, (c) indenting, and d) interweaving. [3]

2.3 Testing Standards

Testing for Kevlar fabric is conducted in various ways, mostly on yarn level and few on fabric level, covered in Section 2.3.1. Gilat and Seidt [12] tested the Kevlar cloth following a Split Hopkinson Bar (SHB) test and obtained a stress-strain curve as in Figure 2.10.

Testing standards for 3M™ dual lock™ is covered in Sections 2.3.2 and 2.3.3.

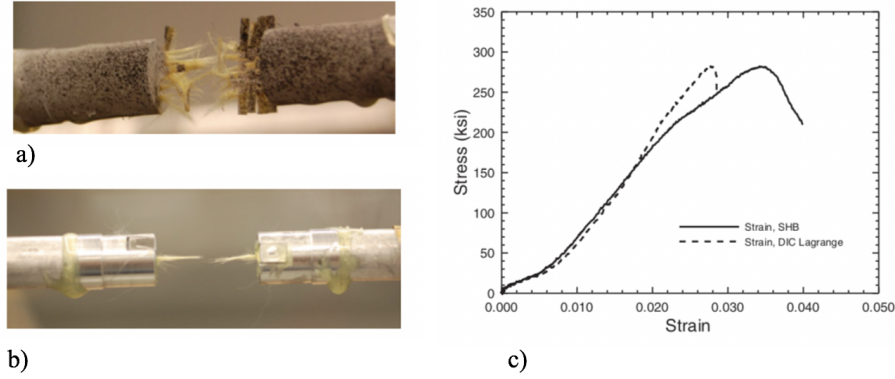


Figure 2.10: (a) Kevlar cloth specimen following a tensile SHB test, (b) Kevlar yarn specimen following a tensile SHB test, and (c) stress strain curve from a tensile SHB test on Kevlar cloth. [12]

2.3.1 Testing Standard for Dry Fabrics – Tensile Test

ISO 13934-1 is a testing standard to determine maximum force and elongation of dry fabrics at maximum force. For materials that elongate less than 8% at maximum force, the standard sample size is 200 mm by 50 mm and the testing rate is 20 mm/min.

Giannaros et al. [10] investigated the quasi-static response of fabric materials under uniaxial tensile loading. All their tests were conducted according to EN ISO 13913-1 except that the sample width was 25 mm instead of 50 mm. This is because specimen width leads to little discrepancy (2%-6%) to Young's Modulus and ultimate strain based on the findings of Zhu et al. [45]. Plain weave Kevlar fabric with areal density 200 gr/m² reached 2000 N before it ruptured, and plain weave Kevlar fabric with areal density 200 gr/m² reached 3000N. Tria et al. [39] tested high and low

velocity impacts against thickening fluid (STF) impregnated weave fabrics (in Figure 2.11).

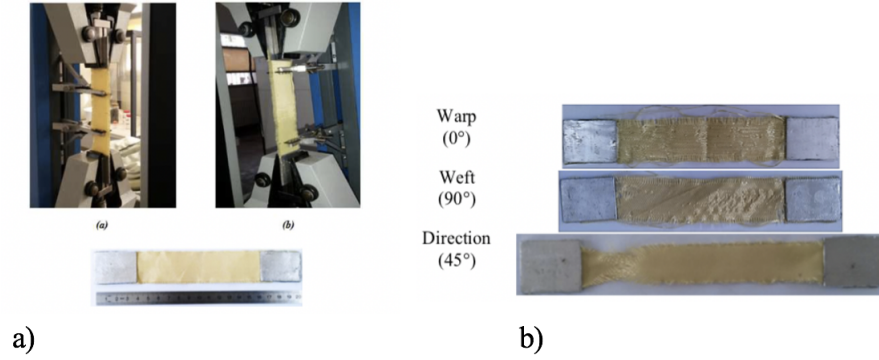


Figure 2.11: (a) Tensile test on Kevlar 29 in warp and weft direction testing, and (b) tensile specimens after tensile test. [39]

2.3.2 Testing Standard for Hook and Loop – Shear Test

ASTM D5169 measures the shear strength of hook and loop touch fasteners using a tensile testing machine. The hook and loop touch fastener comprises of two mating strips, one covered by tiny, stiff protruding shaped hooks, and another covered by pliable loops. Since there are no available testing standards for dual lock, this testing standard for hook and loop is adopted to test the shear strength of 3M™ dual lock™.

The 3M™ dual lock™ is not perfectly symmetric on the strip, causing differences in dynamic shear tests on each configuration. Four configurations of 3M™ dual lock™ fasteners were tested, with each specimen marked with an arrow pointing in the direction that the specimen is unwound from the roll (see Figure 2.12). The arrow

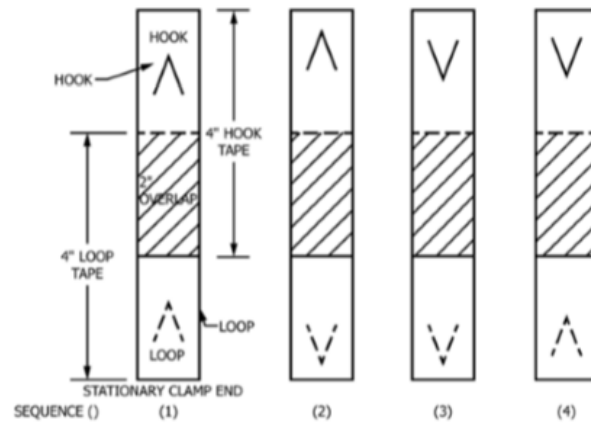


Figure 2.12: Shear direction definitions from D5169

indicates the direction of the hook and loop of the specimens. An average is taken as the final shear strength.

2.3.3 Testing Standard for Hook and Loop – T-peel Test

According to ASTM D5170, the T-peel test is conducted to test the peel strength of hook and loops. Like D5169, each specimen is marked with an arrow pointing in the direction that the specimen is unwound from the roll (see Figure 2.13).

The average peel force of the sample is calculated using the average of the five highest peaks. Five successive equal portions are marked on the plot excluding the first and last inch of separation, then five highest peak values are determined and an average is taken as the peel force.

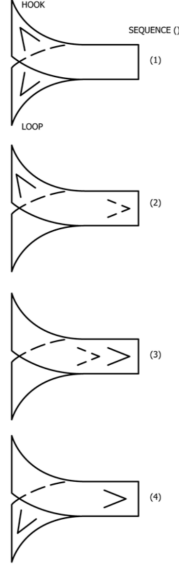


Figure 2.13: T-peel direction definitions from D5170.

2.4 Modeling of Nonlinear Materials

2.4.1 Modeling of Kevlar

As a high-strength material, Kevlar has been tested and modeled for decades at the fabric level (macroscopic), yarn level [19, 22, 9] (mesoscopic) and filament level (microscopic) [30] (see Figure 2.15). Figure 2.14 illustrates three different levels of the fabric. A micromechanical approach represents the actual geometry of the fabric by modeling each yarn and the weave pattern. It is computationally heavy [38] if the component using this material is just a simple piece of the system. A mesomechanical model of Kevlar 129 is utilized by Hill and Braun [19] to implement and evaluate a high fidelity material model of dry fabrics.

A representative volume cell or unit cell is used in fabric level simulations to improve computational efficiency while keeping necessary material properties. The

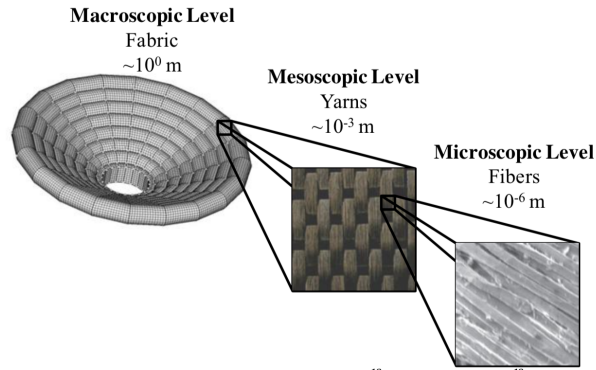


Figure 2.14: Fabric level, yarn level, and filament level model. [19]

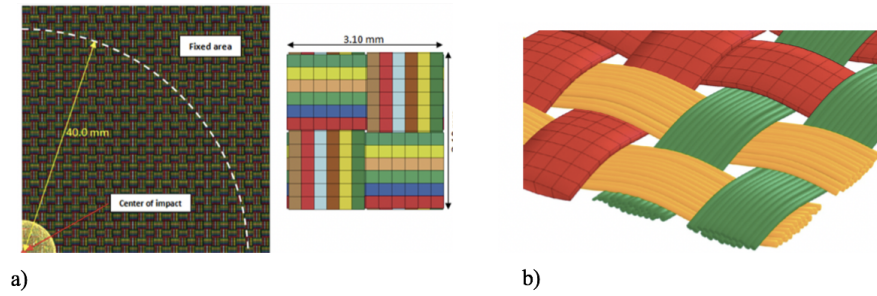


Figure 2.15: Kevlar modeled in (a) yarn level. [9], and (b) filament level. [30]

fabric is assumed to be a continuum material. Figure 2.16 from Hill et. al [19] shows a representative volume cell of fabric.

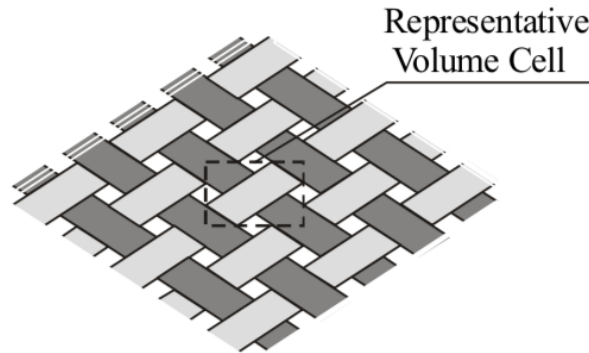


Figure 2.16: Representative volume cell (RVC) of fabric. [19]

Material properties of Kevlar fabric such as Young's Modulus in warp and weft directions, shear strength and crimp ratio have been tested by Bansal [1], Naik [29] and Fein et al. [7]. They conducted tensile tests and shear tests to characterize essential properties needed to represent Kevlar in simulations. Figure 2.17 shows Kevlar 49 in simulation from [1].

2.4.2 Kevlar in LS-DYNA

Woven fabrics are made of strands of synthetic fibers. The characteristics of the yarn material have been widely studied, but dry fabric as a bulk fabric is still under investigation. The woven structure complicates the behaviors of dry fabric, leading to material nonlinearity and making modeling dry fabrics a challenging task.

Conducting impact experiments on fabrics can be costly and challenging. Finite element analysis is an effective way of testing fabric behaviors under large impacts.

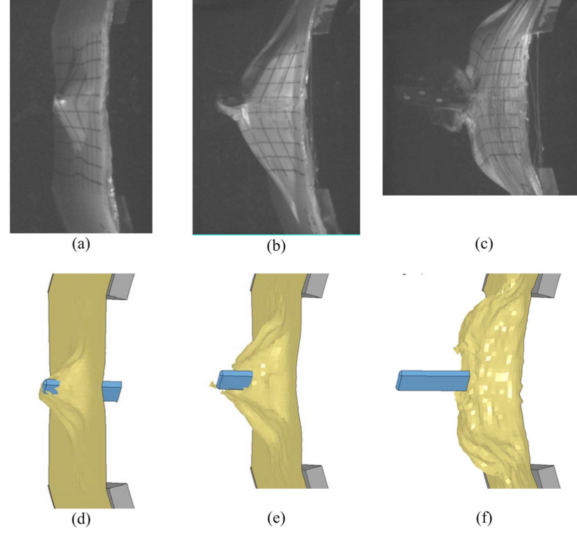


Figure 2.17: Ballistic simulation results compared with experiments on Kevlar fabric. [1]

He et al. [18] wrap Kevlar fabric on containment systems. The performance of Kevlar fabrics resisting impacts and penetrations in applications of aircraft engine containment structure was evaluated.

Figure 2.18 is the stress-strain curve of Kevlar 49 in the warp direction. It can be seen that Kevlar has three distinct regions. The first region has a rather small modulus of elasticity, which is also called the crimp region. The second region is the elastic region, where increase of strain leads to a large increase in stress. The third region is the post-peak region, with a sharp decrease of load-carrying capacity.

A viscoelastic material model of Kevlar fabric is first established and calibrated to fit the material nonlinearities of Kevlar fabric. MAT324 (*MAT_VISCOELASTIC_LOOSE_FABRIC) is chosen to represent the elastic and viscoelastic behavior of Kevlar fabrics. This material type considers the crimp phenomenon of Kevlar fabric,

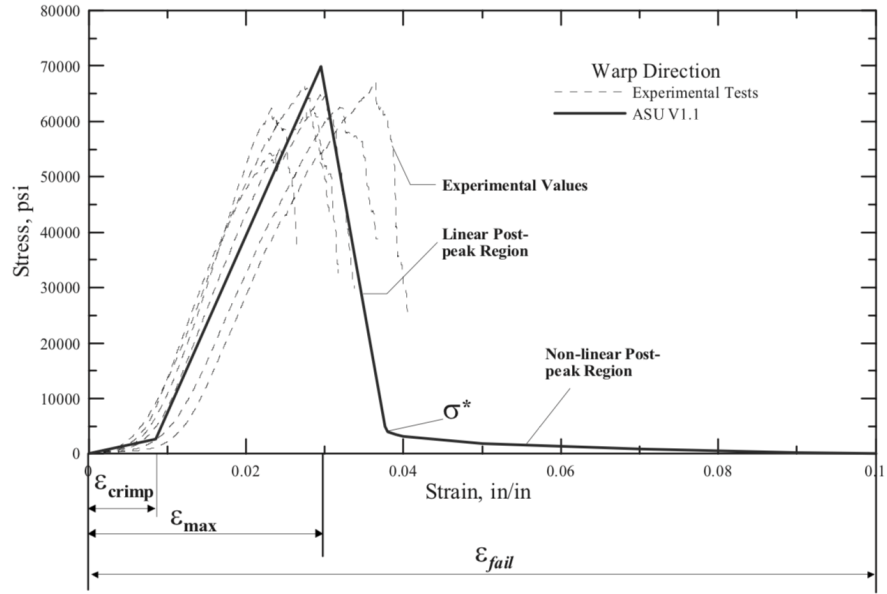


Figure 2.18: Kevlar 49 warp direction uniaxial stress-strain results. [45]

and strain rate effects. The stress versus strain relationship is based on a three-element of model as depicted in Figure 2.19.

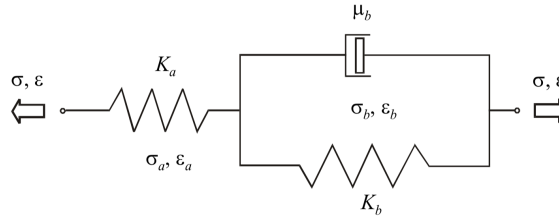


Figure 2.19: Three-element viscoelastic model. [16]

A combination of a Maxwell element without the dashpot, a , and a Kelvin-Voigt element, b , describes the material behavior of the Kevlar yarn. The element a (spring)

accounts for primary bond failures, and element b accounts for the secondary bond failure [6]. The differential equation of viscoelasticity can be derived from the model equilibrium as follows:

$$(K_a + K_b)\sigma + \mu_b\dot{\sigma} = K_a K_b \varepsilon + \mu_b K_a \dot{\varepsilon}. \quad (2.1)$$

Table 2.1 shows properties values used for Kevlar 49. Fang et al. [6] use MAT214, Zhenhua [44] and Fein [7] use MAT234 for Kevlar 49. Detailed names for properties are shown in Table 3.3. All the values are converted to SI units for consistency.

Table 2.1: Material properties used in LS-DYNA.

Properties	Fang, H [6]	Zhenhua, Z [44]	Fein, J [7]	This study	Unit
RO	1440	1440	1440	1440	kg/m ³
E_1	9.60E+10	5.79E+10	5.79E+10	5.80E+10	Pa
E_2	7.40E+09	6.90E+09	6.90E+09	6.93E+09	Pa
G_{12}	2.50E+09	1.64E+10	1.64E+10	1.64E+10	Pa
G_{23}	2.50E+09	N/A	1.64E+10	1.64E+10	Pa
EU	0.033	0.033	0.042	0.042	N/A
W	3.20E-04	1.24E-03	1.24E-03	1.24E-03	m
L	9.09E-04	N/A	N/A	N/A	m
t	8.00E-04	2.793-4	2.79E-04	2.79E-04	m
H	1.41E-04	1.58E-04	1.55E-04	1.55E-04	m
S	6.48E-08	1.79E-06	1.10E-07	4.50E-08	m ²
THL	35	16.9	17	17	N/A
HI	45	45	45	45	N/A
TA	3	3	3	3	N/A
EKA	1.92E+11	1.16E+11	8.10E+10	6.90E+10	Pa
EKB	1.92E+11	N/A	2.03E+11	3.65E+11	Pa
EUA	0.027	0.027	0.023	0.033	N/A
$VM B$	3.50E+07	2.24E+07	2.24E+07	8.62E+06	N/A
C	0.41	0.18	0.2	0.2	N/A
s	N/A	N/A	1.49E-03	1.49E-03	m

Chapter 3: Testing and Simulation Results

3.1 Dry Fabric Tensile Testing

Tensile testing of Kevlar 49 is based on ISO 13934-1. Conventional grips cannot grip the Kevlar fabric directly without slippage and large clamping force (as it may crush the fabric). To prevent any slippage, a double-sided two by two inch aluminum end tab was made to add friction between the Kevlar fabric and the grips. A few trials proved that 0.005-inch-thick aluminum sheet would not be crushed. To prepare for testing, the aluminum surface was abraded with sandpaper, increasing the friction coefficient to allow for adequate adhesion of epoxy between the aluminum surface and Kevlar fabric.

Table 3.1: Properties of Kevlar 49.

Properties	Value
Weight	5 oz./yd ²
Fiber	Kevlar 49, 1140 denier
Thickness	0.010" (0.254 mm)
Weave	Plain
Count	17x17
Warp	624
Fill	643

Testing was conducted on an MTS Criterion Series 40 tester at a rate of 20 mm/min. Testing samples were plain weave 1140 denier Kevlar 49 (shown in Figure

3.1). The data sheet shows there are 17 yarns in the warp direction and 17 yarns in the weft direction. Other properties are listed in Table 3.1. The standard size of the Kevlar sample is eight by two inches, and an eight by one inch sample is also tested to match the force versus strain curve in Figure 3.2.

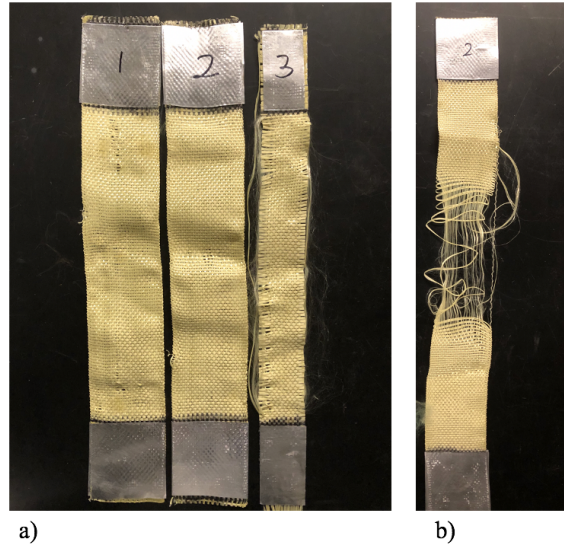


Figure 3.1: Kevlar samples (a) after tensile test, (b) after extended tensile test.

From Table 3.1, the weight of Kevlar 49 is 5 oz./yd², approximately 170 g/m² in areal density. Giannaros et al. [10] tested Kevlar 29 fabric and plotted the stress versus strain curves. It can be seen in Figure 3.2 that areal density of 400 g/m² plain weave Kevlar 29 has larger maximum force than areal density of 200 g/m² plain weave Kevlar 29. It is reasonable to infer that the areal density of 170 g/m² plain weave Kevlar 29 withstands a lower maximum peak force, at least lower than 2500 N for a one-inch wide and eight-inch long testing sample. PW-200-K is defined as plain

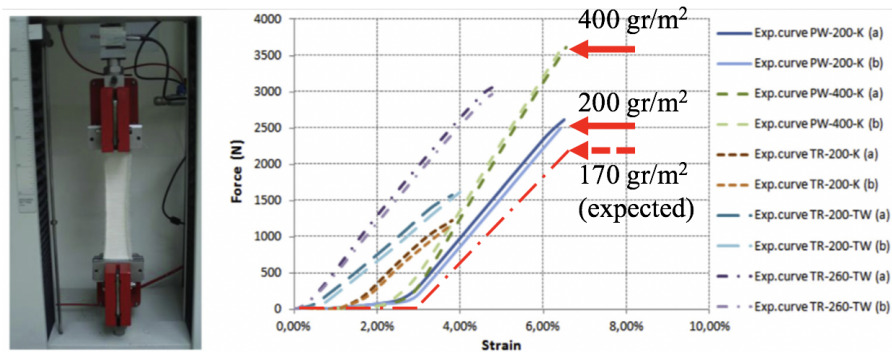


Figure 3.2: Kevlar 29 tensile test of 8 by 1 inch. [10]

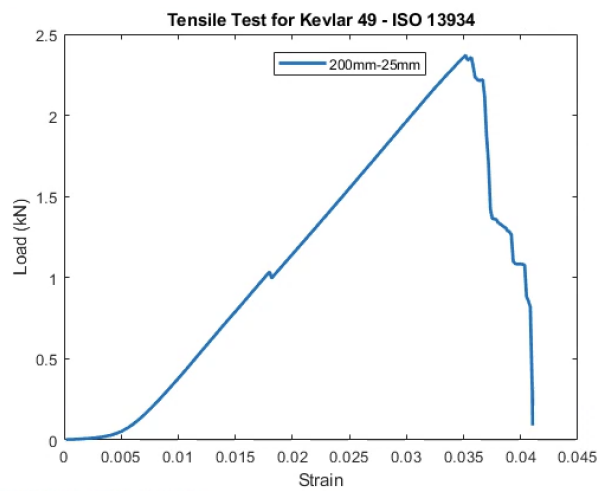


Figure 3.3: Force-strain curve of Kevlar 49 - one-inch wide.

weave Kevlar 29 with an areal density of 200 g/m², and TR-200-TW is defined as tri-axially braided Twaron fabrics with areal density 200 g/m².

The maximum force of one-inch wide Kevlar 49 is 2371 N, just below 2500 N. This is expected from Figure 3.2 although Kevlar 29 and Kevlar 49 are slightly different. Based on tensile strength of Kevlar 29 and Kevlar 49 fibers given by Saleh [34] in Table 3.2, the maximum force difference is within 2.7%; hence comparing tensile test results of Kevlar 49 with Kevlar 29 is acceptable.

Table 3.2: Mechanical properties of aramid fibers.

Fibers	Tensile Strength (MPa)	Modulus of Elasticity (GPa)
Kevlar 29	2920	83-100
Kevlar 49	3000	124

Other differences between Kevlar 29 and Kevlar 49 shown in Figures 3.2 and Figure 3.3 show the strain at maximum force, Kevlar 49 is 3.5%, smaller than that of Kevlar 29, which is about 6.5%. The zigzag in Figure 3.3 is due to the fracture of a single yarn.

Testing results of standard width (50mm) Kevlar 49 samples are shown in Figure 3.4 together with simulation results. The upper subplot is a load-crosshead curve. Crosshead is the displacement of stretching distance. The maximum force is approximately 5 kN at a displacement of 8.9 mm. Crimp behavior started from a displacement of 1.2 mm. A nonlinear region occurred after peak force was reached and yarns in warp direction stopped carrying most of the load one after another. Before reaching zero force, the Kevlar fabric still looks like a) in Figure 3.1 for a long time under stretching. The end of the curve does not represent the situation shown in Figure 3.1 post-extended tensile test because it was kept to continue stretching after the MTS

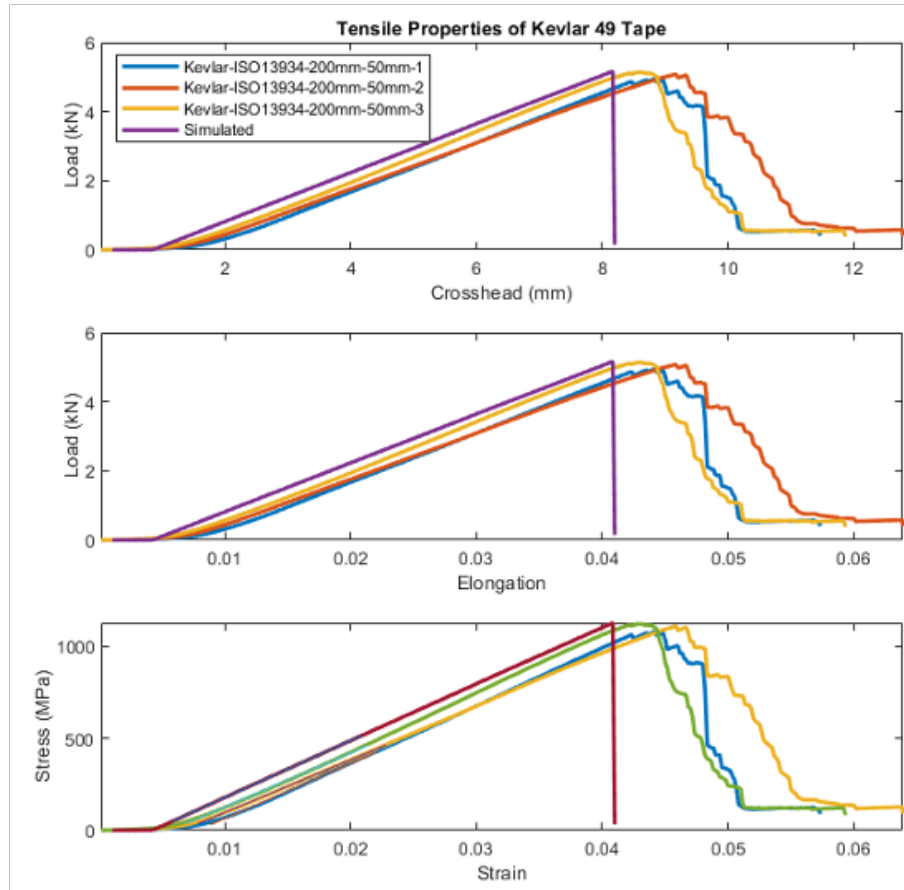


Figure 3.4: Kevlar tensile test load-crosshead curve, load-elongation curve and stress-strain curve.

machine detected failure. If the failure detection is turned off, the end of the nearly zero curve will extend to larger strains while still above zero. The area under the stress-strain curve is the amount of energy absorbed. Although the tensile test stops at a small strain, Kevlar fabric can absorb much more energy after a few yarns fail. The Kevlar yarns fail one by one and after a long stretch Kevlar fibers still tangle together.

The middle subplot in Figure 3.4 is a load versus elongation curve, where percentage elongation is calculated the same as strain. The bottom subplot is stress versus strain curve, where it is observed that the tensile strength of Kevlar 49 fabric reached 1125 MPa at a strain rate of 3.5%.

3.2 Simulation Verification of Fabric Testing

In the current work, a numerical model of Kevlar fabric was created in LS-DYNA under axial tensile testing conditions. A representative volume cell (RVC) is used to model the plain weave Kevlar fabric as with many other studies [18, 19]. The fabric has negligible stiffness, so the coupling effect between warp and weft directions is neglected, the Poisson's ratio is assumed to be zero [7]. The goal of simulating mechanical behavior of Kevlar fabric is to fit the modulus, i.e., the slope of the stress versus strain curve.

Because locking is a gradual process, transitioning from the crimp region to the elastic region is a gradual process in experiments. In simulation, however, the transition is sharper because the crimp region and the elastic region are assumed to be almost bilinear with the transition angle (TA) to locking set to 3° .

The nonlinear failure behavior of Kevlar fabric is neglected assuming each yarn is uniform. Once an element of the Kevlar fabric meets the failure criteria and is deleted, the adjacent elements experience stress concentration and get deleted soon afterwards. The failure criteria can be set via ultimate strain (UA), or the ultimate strain for spring ' a ' (EKA) in MAT234. In experiments, however, each yarn may experience different loading conditions. When one yarn is taking on load in the elastic region, another yarn may not start taking on load given that it is still in the crimp region.

It is worth noting that defining the material direction of an anisotropic material like Kevlar is crucial in simulation. According to the MAT234 in the LS-DYNA manual, the material direction in each element is defined as the diagonal direction of warp yarns and weft yarns (as the horizontal direction illustrated in the trellis mechanism in Figure 3.5). If not explicitly specified, the material direction is assumed to be the same as the element direction, which is from the smallest node number to the second smallest node number. For example, for a 4-node shell element, the element direction is defined as the direction from node 1 to node 2.

Hence, the material direction has to rotate 45 degrees relative to the element direction so that the yarns are aligned with the tensile direction in simulation. Tests of positive 45 degrees and negative 45 degrees to the element direction have been conducted. The force-displacement curve of the simulation proved that positive or negative 45 degrees does not affect the results. This result is expected because whichever yarn rotates to the pulling direction is assumed to be a warp yarn with E_1 elastic modulus; the yarns perpendicular to the pulling direction after rotation are assumed to be the weft yarns with E_2 elastic modulus.

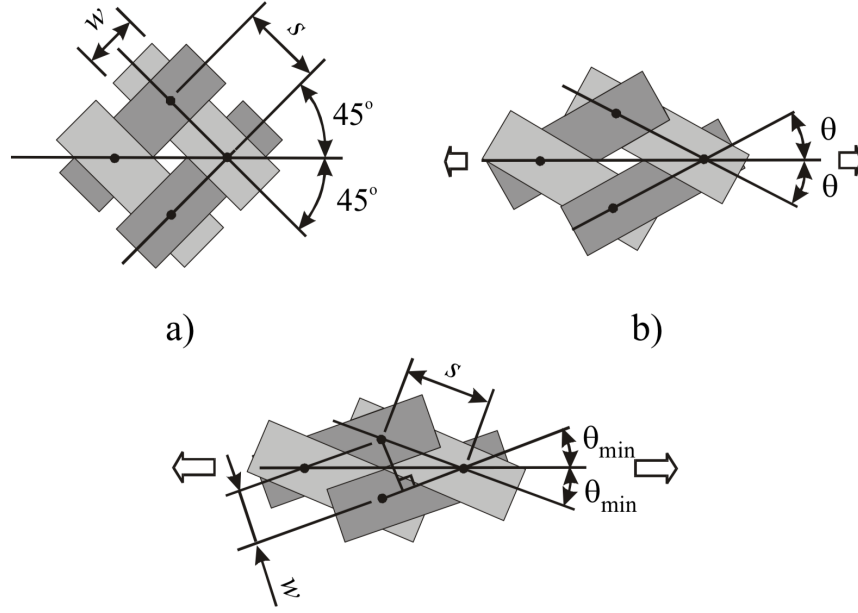


Figure 3.5: Trellis mechanism (a) initial state, (b) slightly stretched in bias direction, and (c) stretched to locking. [16]

The parameters used in MAT234 for Kevlar 49 are given in Table 3.3 and the following lists with SI units.

1. Mass density (ρ)

The mass density of plain weave denier 1140 Kevlar 49 is 1440 kg/m³. Data is read from the product data sheet.

2. Young's modulus in axial direction (E_1)

Young's modulus in axial direction is defined at 5.8E10 Pa.

3. Young's modulus in transverse direction (E_2)

The value of Young's modulus in transverse direction cannot be determined experimentally because of the limitation of the Kevlar tape size. It is usually

Table 3.3: Parameters used in MAT234 for Kevlar 49.

Properties of Kevlar 49	Symbol	Value	Unit
Mass density	RO	1440	kg/m ³
Young's modulus in axial direction	E_1	5.80E10	Pa
Young's modulus in transverse direction	E_2	6.93E9	Pa
Shear modulus	G_{12}	1.64E10	Pa
Transverse shear modulus	G_{23}	1.64E10	Pa
Ultimate strain at failure	EU	0.042	N/A
Yarn width	W	1.2446E-3	m
Actual yarn thickness	t	2.54E-4	m
Effective yarn thickness	H	1.55E-4	m
Yarn cross-sectional area	S	4.5E-8	m ²
Yarn locking angle	THL	17	°
Initial yarn angle	HI	45	°
Yarn transition to lock angle	TA	3	°
Elastic constant for element a	EKA	6.895E10	Pa
Elastic constant for element b	EKB	36.5271E10	Pa
Ultimate strain for element a	$EU A$	0.033	N/A
Damping coefficient for element b	$VM B$	8.61E6	kg/s
Friction coefficient for yarn-yarn interaction	C	0.2	N/A
Span between the yarns	s	1.494E-3	m

much smaller than the Young's modulus in the axial direction, so about 12% of E_1 , 6.93E9 Pa is adopted.

4. Shear modulus (G_{12})

Longitudinal shear modulus is determined experimentally [7] by measuring torsional response of a mass suspended from a known length of Kevlar yarn. The shear constant in the longitudinal direction is determined from the torsional response. The value of 1.64E10 Pa is used.

5. Transverse shear modulus (G_{23})

The transverse shear modulus is expected to be the same value as the longitudinal shear modulus. A value of 1.64E10 Pa is used.

6. Ultimate strain at failure (EU)

The ultimate strain at failure is 0.042, determined by tensile test of a 200 mm by 50 mm Kevlar fabric. EU represents the strain at maximum stress.

7. Yarn width (w)

The yarn width is calculated by measuring the geometry of the undeformed state of Kevlar yarns; w is taken as 1.2446E-3 m.

8. Actual yarn thickness (t)

The actual yarn thickness is retrieved from the product data sheet, being 0.01 inch (2.54E-4 m).

9. Effective yarn thickness (H)

The effective yarn thickness is specified as areal density divided by mass density. The value of effective yarn thickness is 1.55E-4 m.

10. Yarn cross-sectional area (S)

Volume divided by length is the effective cross-sectional area of a Kevlar yarn required by MAT234. Only the yarns in the warp direction take load in the actual cross-sectional area. The Kevlar testing sample has 17 yarns by 17 yarns per square inch, therefore half the effective cross-sectional area was adopted first. The volume of the Kevlar was obtained by subtracting the total volume of epoxy from total volume in the beaker. The weight of Kevlar and epoxy were also measured for calculation. In Figure 3.6, the volume of epoxy is measured three times as the epoxy was added to the beaker, each addition of epoxy was denoted as 'e1', 'e2' and 'e3', respectively. Three Kevlar 49 fabric samples were added after e1, denoted as 'k'. A vacuum pump was used to reduce entrapped

bubbles in the epoxy. The volume measured for each Kevlar 49 fabric was 1.4649 ml. The cross-sectional area of Kevlar samples was calculated at $1.19\text{E-}7 \text{ m}^2$ and $1.06\text{E-}7 \text{ m}^2$. Details of calculations can be found in Appendix B. However, the actual sum of the length of warp yarns and weft yarns for an eight by two inch Kevlar sample is $(272 + 432 = 704)$ inch, instead of equal length addition (see Figure 3.7). The length of warp yarns is calculated by 8 inch by 17 yarns/inch times 2 in = 272 in. The length of weft yarns is obtained by folding the weft yarn in half four times and measuring the folded length as 34 inch. The length of weft yarns is 16 times 34 inches = 432 inches, assuming this fabric is made of a single yarn with total length (L) of 704 inches. The volume measured (V) is 1.4649 ml. The cross-sectional area of a single yarn (S) is obtained by dividing the volume by the total length:

$$S = \frac{V}{L} = \frac{1.4649}{1788.2} \text{ cm}^2 = 8.19\text{E-}8 \text{ m}^2, \quad (3.1)$$

where

$$V = 1.4649 \text{ ml} = 1.4649 \text{ cm}^3,$$

$$L = 704 \text{ in.} = 1788.2 \text{ cm.}$$

The cross-sectional area is in fact specified at $4.5\text{E-}8 \text{ m}^2$ due to measurement errors. The volume might be larger than the actual Kevlar volume because of the space taken by air in the epoxy.

11. Yarn locking angle (THL)

The yarn locking angle is the starting angle that warp yarns and weft yarns interlock. The value of this angle is determined by width and span of the yarn.

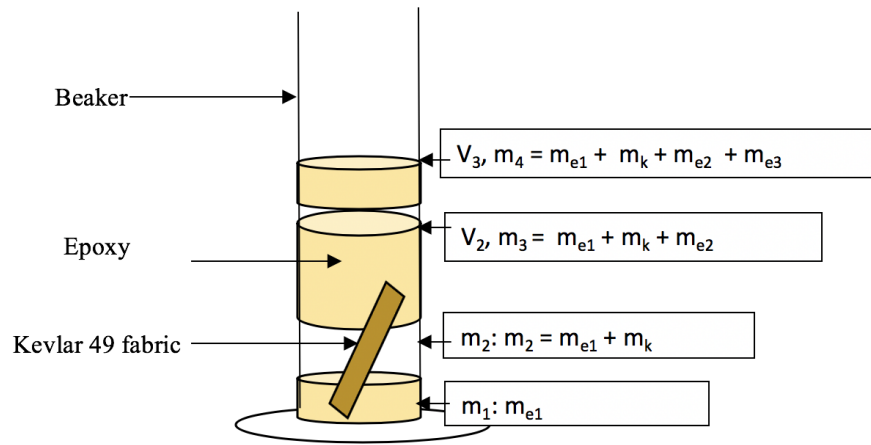


Figure 3.6: Measurement of volume of Kevlar samples.

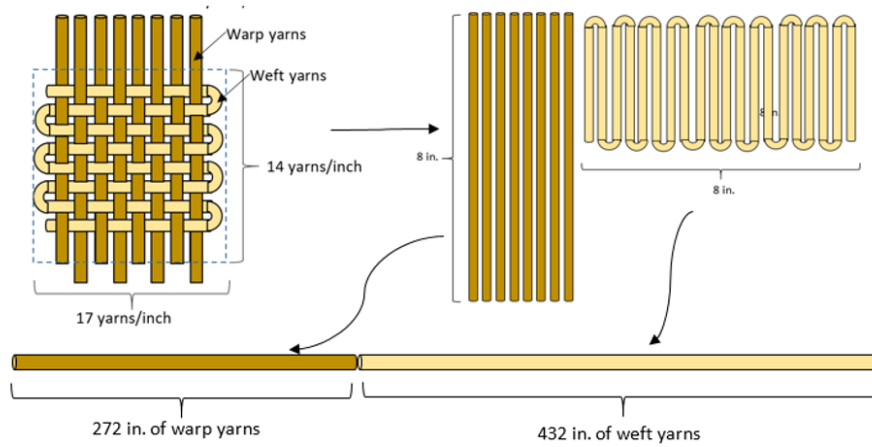


Figure 3.7: Ratio of warp yarns and weft yarns.

The minimum braid angle (θ_{min}) is calculated as follows:

$$\sin(2\theta_{min}) = \frac{W}{s}, \quad (3.2)$$

where

$$W = 1.2446\text{E} - 3 \text{ m},$$

$$s = 1.494\text{E} - 3 \text{ m},$$

$$\theta_{min} = \frac{1}{2} \sin^{-1}\left(\frac{W}{s}\right) = \frac{1}{2} \sin^{-1}\left(\frac{1.2446\text{E} - 3}{1.494\text{E} - 3}\right) = 28.21^\circ.$$

The locking range angle (θ_{lock}) is determined by

$$\theta_{lock} = 45^\circ - \theta_{min} = 45^\circ - 28^\circ = 17^\circ. \quad (3.3)$$

The maximum braid angle (θ_{max}) is defined as

$$\theta_{max} = 45^\circ + \theta_{lock} = 45^\circ + 17^\circ = 62^\circ. \quad (3.4)$$

12. Initial yarn angle (HI)

The initial yarn angle is set to be 45° because the initial yarn angle is half of the total angle between warp yarns and weft yarns, which is orthogonal.

13. Yarn transition to lock angle (TA)

The transition angle to lock ($\Delta\theta$) is a small angle that locking occurs and warp yarns start to show large force resistance. In Figure 3.8, ($\Delta\theta$) is set to be 3° .

14. Elastic constant for element a (EKA)

The value of linear elastic constant for element ‘a’ is specified at $6.89480\text{E}10$ Pa. Both EKA and EKB are rate-dependent parameters. Fein et al. [7] selected the optimal values for EKA and EKB by fitting the curve at different strain

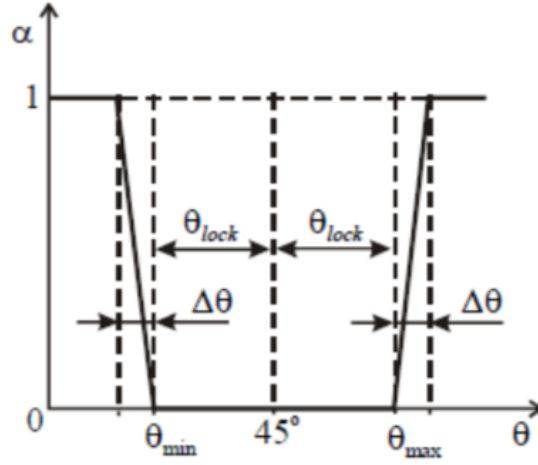


Figure 3.8: Lateral contact factor α as a function of braid angle θ . [16]

Table 3.4: Optimal values of EKA and EKB for various strain rates.

Strain Rate (/s)	EKA (Pa)	VMB (kg/s)
0.1	6.89480E10	8.618E6
1	7.44634E10	1.034E7
1000	8.1013E10	2.068E7
2000	8.1013E10	2.241E7

rates. Strain rate of tensile test is closest to 0.1 /s. Hence, EKA is assumed to be 6.895E10 Pa.

15. Elastic constant for element b (EKB)

The value of the second elastic constant for element b is calculated at 36.5271E10 Pa (shown in equation 3.5).

$$K_b = \frac{K_a E_1}{K_a - E_1}, \quad (3.5)$$

where K_a is the elastic constant for element a (EKA) and E_1 is the static Young's modulus in the axial direction,

$$K_a = 6.89480\text{E}10 \text{ Pa},$$

$$E_1 = 5.80\text{E}10 \text{ Pa},$$

$$K_b = \frac{6.89480\text{E}10 * 5.80\text{E}10}{6.89480\text{E}10 - 5.80\text{E}10} = 36.5271\text{E}10 \text{ Pa}.$$

16. Ultimate strain for element a (EUA)

The ultimate strain for element a is determined by the quotient of maximum stress and stiffness of element a . The maximum stress in the tensile test is shown to be 1.12 GPa, so EUA is 0.0162.

$$EUA = \frac{\sigma_{max}}{EKA} = \frac{1.12\text{E}10}{6.895\text{E}10} = 0.0162.$$

However, the value of 0.0162 will cause Kevlar fabric to fail earlier than expected.

The value of 0.33 is adopted to fit the strain value of 0.042.

17. Damping coefficient for element b (VMC)

The value for damping coefficient is 8.61E6 kg/s. It is determined also by curve fitting and the value is taken from Table 3.4.

18. Friction coefficient for yarn-yarn interaction (C)

The friction coefficient between yarns is specified at 0.2. This value is from fabric friction testing [1].

19. Span between the yarns (s)

The span between the yarns is calculated by dividing 1 inch by the number of yarns within 1 inch, which is 17 yarns per inch. The value of 1.494E-3 m is used.

The error in the tensile test result on Kevlar 49 fabric is approximately 8% in terms of maximum force, maximum strain at max force and modulus of elasticity. Compar-

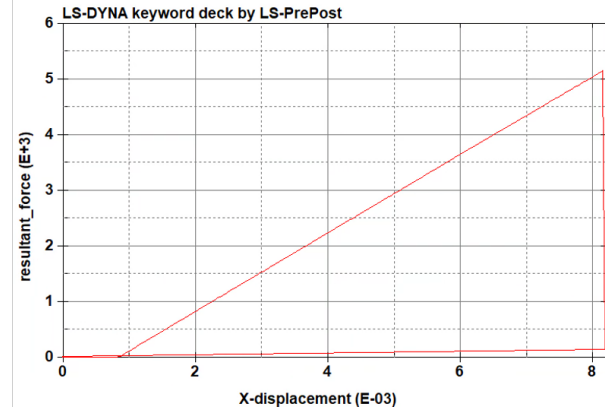


Figure 3.9: Kevlar 49 force-displacement curve in LS-DYNA for the tensile test.

ison of testing results and simulation is shown in Table 3.5. Force-displacement curve of Kevlar 49 tensile test in LS-DYNA is in Figure 3.9.

Table 3.5: Testing results and simulation.

	Max disp.	Max force	Max stress	Strain at max stress	E_1
Sample1	8.84	4.95	0.04	1083.00	29.95
Sample2	9.17	5.08	0.05	1112.00	28.67
Sample3	8.74	5.11	0.04	1125.00	29.48
Average	8.91	5.04	0.04	1106.67	29.37
Simulation	8.20	5.16	0.04	1130.00	31.01
Error/%	-8.01	2.36	-5.26	2.11	5.60

3.3 Actuation by Coiled Fishing Line

Coiled fishing lines are made by twisting a fishing line while a moderate amount of weight is applied at the end of the fishing line. The value of the weight is based on

the diameter of the fishing line. The thicker the diameter, the more weight is needed for the fishing line to start coiling. In the experiment, a tube is used to prevent the fishing line from releasing the twist shown in Figure 3.10 (b), which is already twisted. Spinning is provided by a drill and a hook shown in Figure 3.10 (a), which is not twisted.

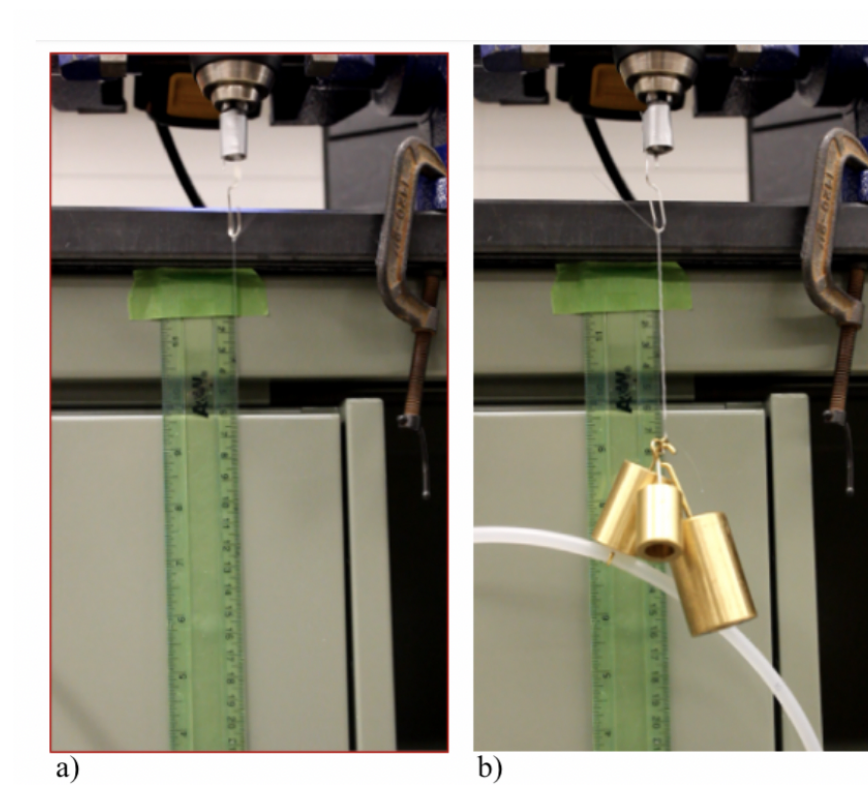


Figure 3.10: Fabrication of self-coiling fishing line, (a) not twisted, and (b) twisted.

To actuate the fishing line, a heat gun is used to evenly distribute heat along the coiled fishing line. All the self-coiling fishing lines are homochiral, which indicates it will contract under heat. Mandrel coiling is able to produce both homochiral and heterochiral coils.

Mandrel coils formed by twisting and winding the monofilament in the same direction are referred to as homochiral coils, given that the chirality of the twisted monofilament matches the chirality of the resulting coil. Homochiral coils will contract under heat, while heterochiral coils will expand under heat. Figure 3.11 (a) are fishing lines warped on a rod homochirally and heterochirally from left to right before heating under 250 F for an hour, and (b) shows the same coiled fishing line after heat treatment.

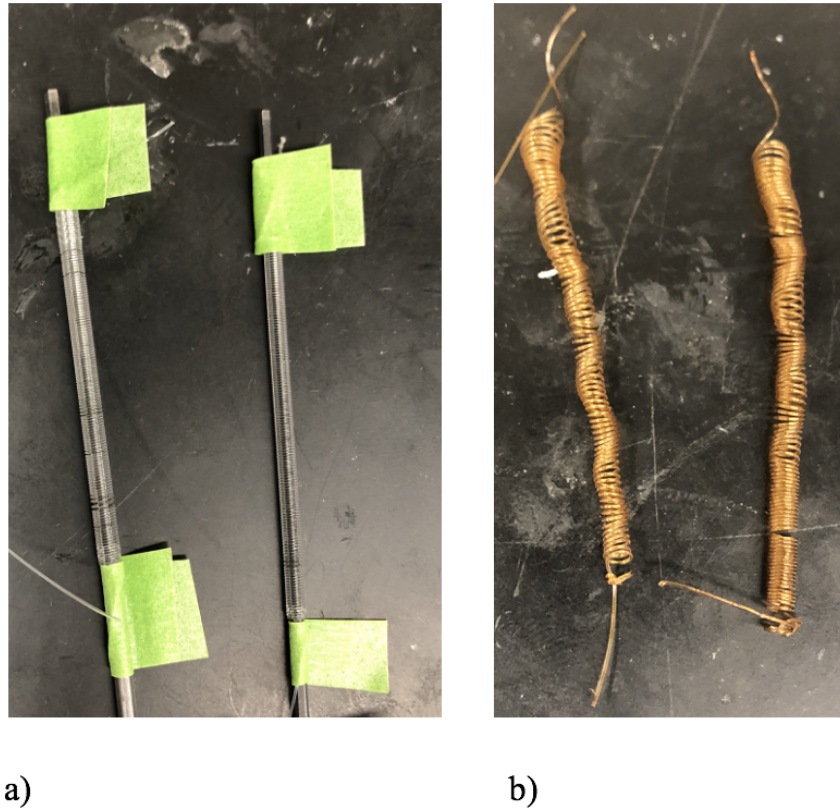


Figure 3.11: Fabrication of mandrel-coiling fishing line, (a) before heat treatment, and (b) after heat treatment.

Chapter 4: Characterization of Latching Mechanisms

4.1 Tests for 3M™ Dual Lock™

3M™ Dual Lock™ can be made of any orientable thermalplastic resin, preferably polypropylene (PP) and polyethylene (PE) [26]. The strongest 3M™ Dual Lock™ is expected to have a shear stress of up to 41 N/cm^2 [4]. To verify the actual strength of the Dual Lock™ products bought from 3M™ retailers, tensile, shear, and disengagement tests are conducted.

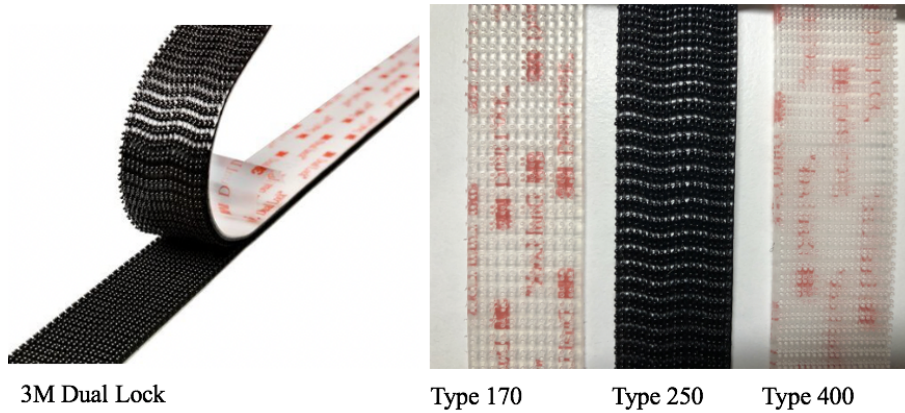


Figure 4.1: 3M™ Dual Lock™ stripes and type 170, 250 and 400.

Given that the testing standard used by 3M is modified from standard testing and not open to the public, available testing standards from ASTM are adopted. Minor differences of testing results are expected when comparing the results to the product data sheet 3M company discloses.

For reversible adhesion, shear strength plays the most important role, followed by normal strength and peel strength. Even though disengagement tests and peel tests are performed as well, shear strength is the dominant strength. A testing standard for disengagement tests is customized as covered in Section 4.1.1. ASTM D5169 and D5170 are used for shear test and peel tests, respectively. These two testing standards are for hook and loop fasteners, but are also used to test dual lock because of their similar working mechanism and lack of available testing standard on the dual lock.

Table 4.1: 3M™ Dual Lock™ stem density combinations.

Stem Density (per sq/in)	Combinations
Strongest	250:400
Stronger	250:250
Strong	170:250
Not Recommended	170:170 or 400:400

Unlike Velcro-type adhesives, the 3M™ Dual Lock™ is insensitive to pressure. Once engaged, the strength of the 3M™ Dual Lock™ remains the same regardless how much pressure is applied to engage the mushrooms of the 3M™ Dual Lock™. Hence, test procedures are not strictly following D5169 and D5170 in terms of pressure requirement.

3M™ Dual Lock™ Reclosable Fasteners are available in three stem densities. It can be seen from Table 4.1 that the strongest combination is type 250:400. The stem density can neither be too sparse as in the 170:170 combination nor too dense as in the

Table 4.2: Strength of 3M™ Dual Lock™ and hook and loop. [4]

Combination	Dynamic Tensile (Disengage)	Dynamic Shear	T-peel
170:250	18.5	9.8	1.2
250:250	29.6	15	3.3
170:400	29.6	14.5	2.5
250:400	41.4	41.3	2.6
250/SJ3571 loop	N/A	112	N/A

Note: The unit for dynamic tensile (disengage) is N/cm²; the unit for dynamic shear is N/cm²; the unit for T-peel is N/cm width.

400:400 combination. With the less dense combination, engagement is weak; heavy distortion results in one-time use with the 400:400 density combination. Therefore, the best combination of 250:250 is chosen as main testing samples, which is the most accessible 3M™ Dual Lock™ on the market.

Most testing samples are 3M™ Dual Lock™ Type 250 Dual Lock Reclosable Fasteners, unless specified elsewhere. The testing rate is 100 mm/min for disengagement test, shear test (D5169), and T-peel test (D5170).

4.1.1 Disengagement Test

The disengagement test is to test the normal force for disengagement over a certain area of the Dual Lock. The disengagement test sequence is shown in Figure 4.4 (d-f). In sample preparations of the disengagement test, samples stick to the fixture with its own adhesives. Its own adhesives do not fail before Dual Lock's failure. The gap between two two-by-one inch strips comprising a two-by-two square is negligible (see Figure 4.2). Fixtures are clamped on the MTS machine and move in opposite directions at a rate of 20 mm/min until all mushroom extrusions of Dual Lock disengages.

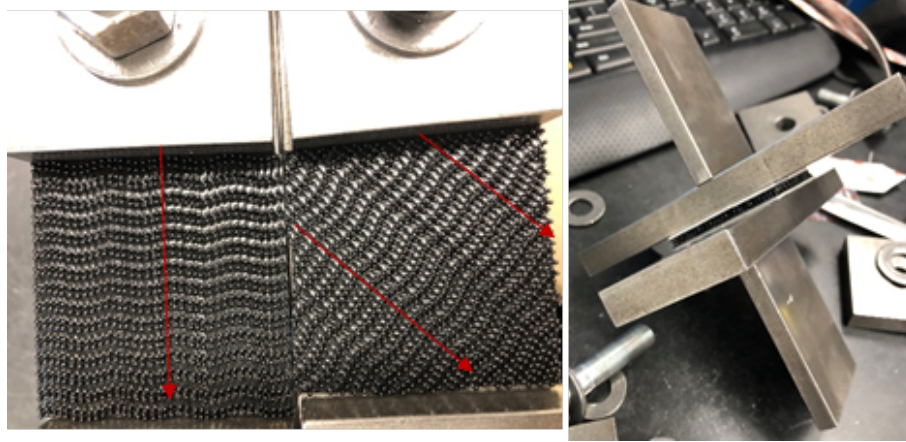


Figure 4.2: Sample arrangement and disengagement test fixture.

Because of the wavy pattern of the 3M™ Dual Lock™, the angle of engagement may have an impact on the disengagement strength. The angle of each specimen is defined as the direction that the specimen is unwound from the roll; 0°, 45°, 60° and 90° engagement angles are investigated. Table 4.3 refers to Figure 2.12 for marking position 1, 2, 3 and 4.

When 3M™ Dual Lock™ samples are snapped at 90° to each other, they have the largest disengagement force, followed by 0°, 60° and 45°. Table 4.3 shows the disengagement force required to detach a 2 by 2 inch 3M™ Dual Lock™ specimen.

4.1.2 Shear Test

Shear test is to measure the shear strength of hook and loop fasteners. According to D5169, the average shear strength of four different engagement combinations are taken as the shear strength. Four engagement combinations are drawn in Figure 2.12. The samples for the shear test is shown in Figure 4.3. In Table 4.5, the plus sign and minus sign are used to define the strip direction that the specimen is unwound from

Table 4.3: Results of disengagement test of 250:250 3M™ Dual Lock™.

Angle (°)	Position	Force (N)	Pull Strength (N/cm ²)
45	1	784	29.0
45	1	725	
45	1	733	
45	2	742	
45	2	698	
45	2	704	
45	3	620	23.1
45	3	605	
45	3	566	
45	4	519	
45	4	538	
45	4	566	
60	1	704	27.0
60	1	690	
60	1	693	
60	2	734	
60	2	718	
60	2	715	
60	3	711	25.6
60	3	651	
60	3	622	
60	4	681	
60	4	688	
60	4	628	
90	1	919	34.0
90	1	874	
90	1	843	
90	2	787	
90	2	824	
90	2	709	
0	1	802	29.0
0	1	722	
0	1	724	
0	2	797	
0	2	756	
0	2	713	

the roll. Take the average force of all strip direction combinations, the average shear strength is obtained as 12.3 N/cm².

Table 4.4: Comparison of experimental dynamic shear strength with literature.

Category	Combination	Literature [4]	Experiment
3M™ Dual Lock™	170:250	9.8	N/A
3M™ Dual Lock™	250:250	15	12.3
3M™ Dual Lock™	170:400	14.5	N/A
3M™ Dual Lock™	250:400	41.3	26.34
3M Hook and Loop	250:SJ3571 loop	77.22	51.57

Note: The unit is N/cm².

The strongest combination (250:400) is also tested and the shear strength is obtained as 26.34 N/cm². The results are compared with data retrieved from Literature [4] in Table 4.4. It can be seen that the testing results are close in the 250:250 combination, but for the 250:400 combination, there are larger difference. This is probably because the combination of different areal density of mushroom extrusions create different engagement patterns. Tighter engagement in the shear direction might yield higher shear strength. Besides, 3M Hook and Loop products (250:SJ3571) are also tested, the shear strength is obtained as 26.34 N/cm². It is higher than 3M™ Dual Lock™, but the difficulty to detach the strip and the existence of minor movement in the shear direction after engagement makes make it a less promising candidate for this application.

4.1.3 Peel Test

Peel test (D5170) is to measure the peel strength. The T-peel test sequence is shown in Figure 4.4 (a-c).

Average of the highest peaks in five successive regions excluding the first and last 1-inch region is taken as the peel strength. From Table 4.6, the average peel strength of 7 repeated tests is 6.2N.

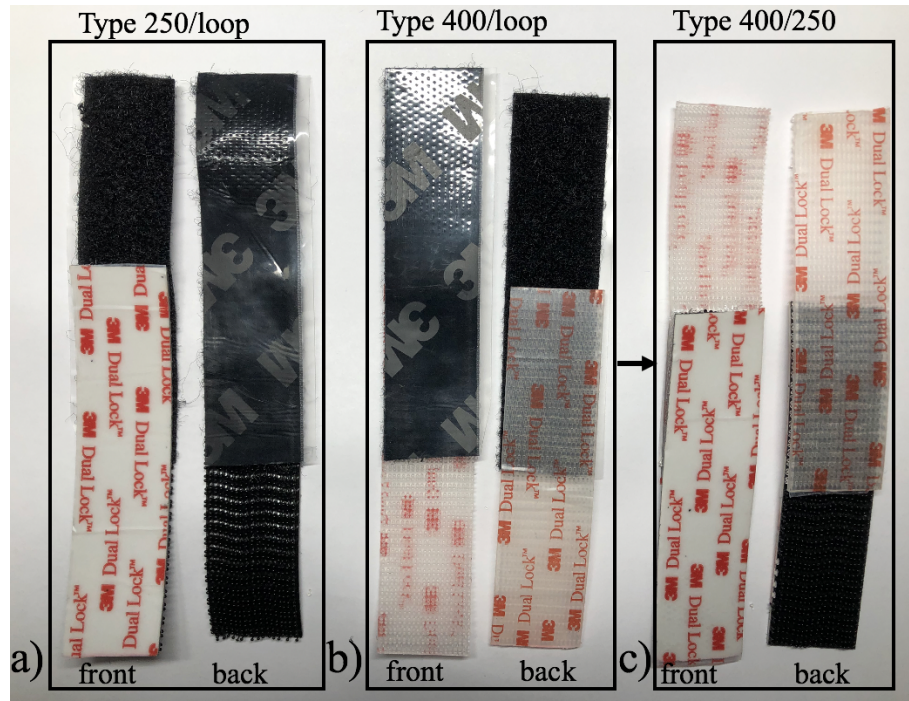


Figure 4.3: Samples for the shear test.

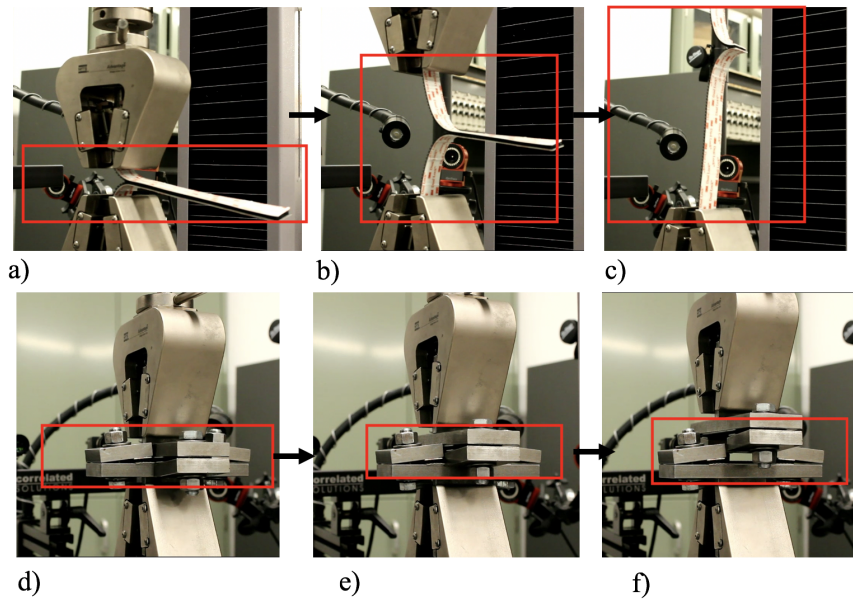


Figure 4.4: (a-c) T-peel test sequence, and (d-f) disengagement test sequence.

Table 4.5: Result of shear test of 250:250 3M™ Dual Lock™.

Upper strip dir.	Lower strip dir.	Force (N)
+	+	153
+	+	148
+	+	161
+	-	113
+	-	132
+	-	122
-	-	196
-	-	217
-	-	195
-	+	155
-	+	154
-	+	161

Table 4.6: Result of peel test of 250:250 3M™ Dual Lock™.

Test No.	Avg. of largest 5 peaks (N)
1	6.095
2	6.121
3	5.694
4	5.703
5	3.850
6	7.769
7	8.166

4.2 Metal Dual Lock

4.2.1 Steel Pin Lock Fabrication

Metal dual locks can have stronger shear strength since each metal mushroom is more difficult to deform compared to plastic mushrooms. A metal mushroom dual lock sample is fabricated using steel pins with round heads resembling a mushroom head. Steel pins are commonly-used size 17 dressmaker pins. The total length is 1 1/16 inch. Steel pins are first pinned vertically on a piece of foam, then a layer of epoxy is applied to fix the position of the pin. The foam extends to the edge as a frame to prevent epoxy from overflowing. A layer of silicone rubber is added to

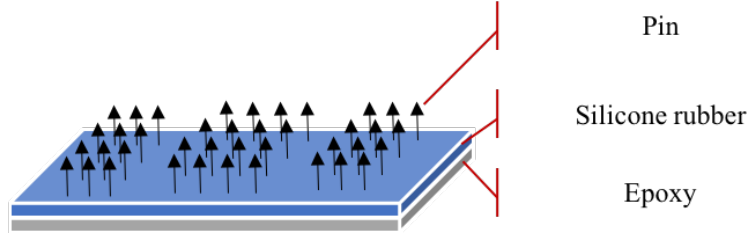


Figure 4.5: Layers of unaligned pin lock.

allow bending of each pin so that they can deform elastically at the rubber layer while engaging with the opposite metal mushroom heads. The layer information is in Figure 4.5 and the fabrication process is illustrated in Figure 4.6.

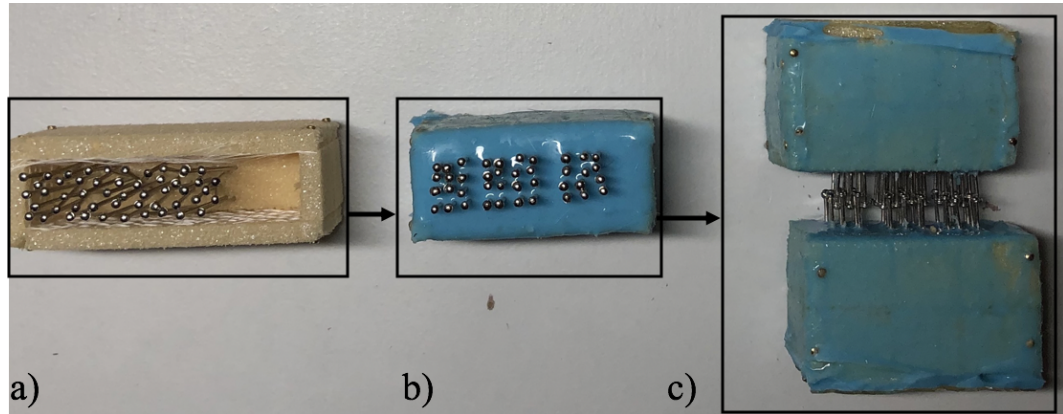


Figure 4.6: Initial steel pin lock fabrication process: (a) insert pins into the foam, (b) fill resin and then rubber in the gaps of foam wall and cure, and (c) engage pins.

The metal mushroom dual lock has a significant improvement in disengagement strength, almost 3 times that of the 3M plastic dual lock (see area of 0.5 by 1 inch in Table 4.8). However, the alignment of each pin becomes an issue given that each

pin is inserted into the foam by hand. The visual method of alignment is far from satisfactory.

Table 4.7: Laser cutting material comparison.

Material	Card Stock	Cardboard	Acrylic
Thickness (in.)	0.016	>0.1	0.096
Resolution	Very high	High	Low
Cutting time (Holes/min)	216	1000	30

Laser-cutting proves to be helpful for alignment. Holes are drilled on card stock and piled up as a guide for fixing the pins. Table 4.7 shows the comparison among three candidate materials for laser cutting. To keep resolution, materials used for laser cutting cannot be too thick like acrylic plates because heat concentration along the depth ruins resolution. It also takes a long time to drill holes on acrylic plates. However, card stock is not the best solution. Even if it is quick to drill a hole on card stock with high resolution, a single guide requires more than 35 pieces of card stock for secure standing of $1 \frac{1}{16}$ inch length pins. It is still time-consuming to mass-produce a guide for pins. With the past sample creations, cardboard results as a plausible alternative. Figure 4.7 and Figure 4.8 shows steel pin lock fabrication process and contact areas, respectively.

The spacing lengthwise is $\frac{1}{13}$ inch and spacing along width is $\frac{1}{10}$ inch. This is deliberate to enable tighter engagement in one direction and loose engagement in the orthogonal direction for easy release in applications. The waviness of the cardboard along depth adds about 12 times the thickness of card stock while the equivalent thickness is just 3 times the thickness of card stock. Two layers of card stock are adequate to support the standing of pins with no performance loss. This means the laser cutting time is reduced by 5-7 times.

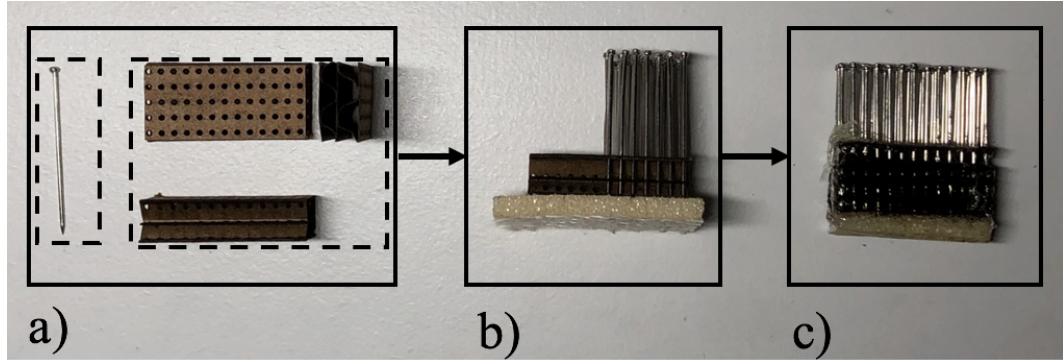


Figure 4.7: Steel pin lock fabrication process (a) prepare pin and cardboard, (b) insert pin into cardboard and foam, and (c) fill resin in the gaps of cardboard and cure.

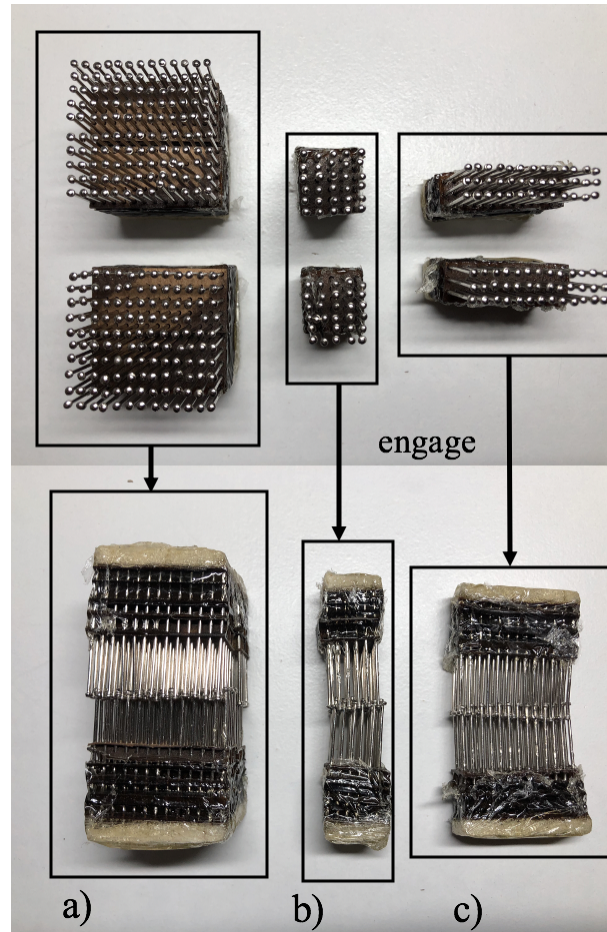


Figure 4.8: Steel pin lock with contact area of (a) 1 by 1 inch, (b) 0.5 by 0.5 inch, and (c) 1 by 0.5 inch.

4.2.2 Comparison of Metal and Plastic Dual Lock

Table 4.8 shows that alignment actually reduces the disengagement strength of metal mushroom dual lock. However, the aligned metal mushroom dual lock is almost twice as strong as the plastic dual lock on average in terms of disengagement strength. The average disengagement strength of the aligned pin lock is 51.4 N/cm², and the average of the 90° crossed metal pin lock is 57.5 N/cm². Tighter spacing will give a slightly higher disengagement strength. The highest pull strength is 72.5 N/cm².

Table 4.8: Result of pull test of metal pin lock.

Area (in.x in.)	Direction	Force (N)	Pull Strength (N/cm ²)
1 x 1	aligned	296	45.9
1 x 1	aligned	450	69.8
1 x 1	aligned	205	31.8
1 x 1	crossed	468	72.5
1 x 1	crossed	324	50.2
1 x 1	crossed	156	24.2
0.5 x 0.5	aligned	97	60.1
0.5 x 0.5	aligned	92	57.0
0.5 x 0.5	aligned	71	44.0
0.5 x 0.5	crossed	115	71.3
0.5 x 0.5	crossed	103	63.9
0.5 x 0.5	crossed	101	62.6
0.5 x 1	not aligned	292	90.5

The life cycle of the pin lock is less than 10 times because of the plastic deformation of pins. Continuing testing with the same pin has little resistance to disengagement force. This is not comparable to the plastic dual lock, which is expected to have a cycle life of 1000 [26] before losing 50% of the original strength. For the 1 by 1 in. metal pin lock sample, the pull strength decreases dramatically in the crossed combination because of severe deformation of pins. This phenomenon is not obvious for the 0.5 by 0.5 in. pin lock sample. This implies that slightly larger spacing among

pin head blocks might increase the disengagement strength because it avoids severe deformation.

4.2.3 Discussion

Overall, the metal dual lock is about two times stronger in the normal direction than the plastic dual lock. However, due to the inflexibility of each mushroom head, engagement can be challenging when the spacing gradually changes as permanent deformation occurs. The reduced life cycle of the metal dual lock also poses a threat to human life if the dual lock is used as a safety measure. Therefore the engagement mechanism is retained, but plastics are favored as a mushroom-type lock.

4.3 2D Bistable Compliant Mechanism Lock

4.3.1 Mushroom-type Compliant Mechanism

Arrays of mushroom heads are not uncommon in reversible adhesion to enable strong engagement. The aim of a new design is secure locking and easy unlocking. For simplicity, a 2D design is investigated first. To mimic a mushroom head, a simple

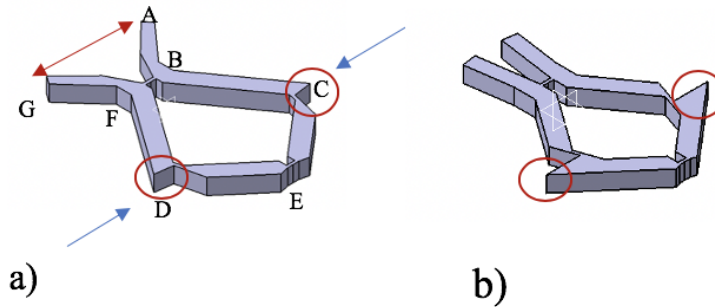


Figure 4.9: First design of four-bar linkage with modified sharp edges.

4-bar linkage design is created (illustrated in Figure 4.9). The loop B-C-E-D-F can either expand or shrink if there is force or displacement actuation on the bars at the end A and G. Actuation can also be done by applying a parallel force with E in the middle or torque on link CE, depending on the application. This design will lock only based on friction on the surface area of link BC and FD when the actuation force or displacement is large, which is impractical. Later the teeth on C and E are modified to the adjacent link in order to prevent the opposite loop from shrinking and unhooking. Also, a smaller angle between AB and FG will enable force or displacement amplification on CE in the loop. The loop itself is bistable, but cannot be achieved by actuation at the AG end. Later designs will use bistability to achieve easy locking. Figure 4.9 shows the first rendering of the four-bar linkage latch. Figure 4.10 shows the physical bistable latch with two bistable loops. Figure 4.11 illustrates the physical symmetric bistable latch.

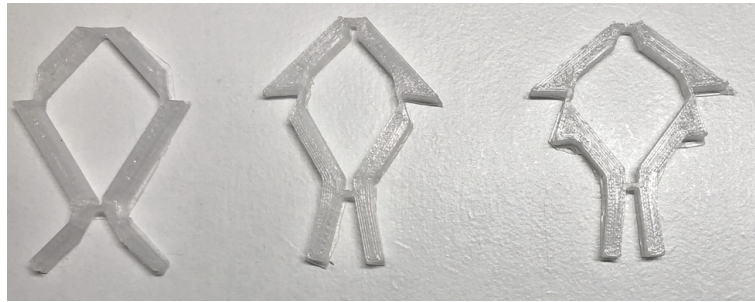


Figure 4.10: Physical bistable latch.

In fabrication, polypropylene (PP) rather than PLA is used in 3D-printing to test the functioning of the design based on its low flexural modulus and flexural strength. Joints can be made with thin PP, and it functions well if the length is about half the

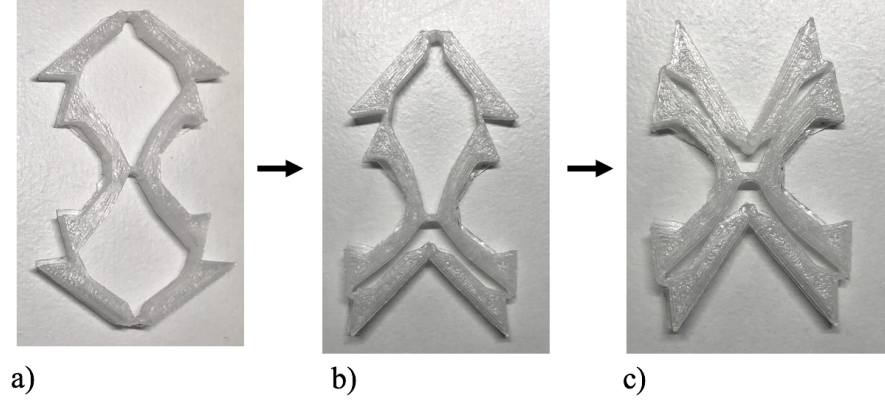


Figure 4.11: Physical symmetric bistable latch.

perimeter of a circle with radius being the thickness. Thicker PP will add stiffness to the link but retain some flexibility of the link. This is how the design allows for a compliant mechanism.

Actuation on both sides could pose a problem given that arrays of mushroom-type extrusions leave little for local control on each mushroom head, which will be investigated in the future. Given this issue, one side of the mushroom head is set to be fixed with the minimum function of the teeth for hooking. A ratchet-like tooth is presented next section.

4.3.2 Ratchet Compliant Mechanism

A ratchet-like teeth design is sketched with the same angle as the teeth on the flexure. Once the B-C-E-D-F loop is squeezed and goes in the ratchet, the flexure will be locked and cannot slip. The only way the flexure can go backwards is that the loop is squeezed again by force or displacement actuation, thus unlocking with the ratchet-like teeth. In addition, another pair of teeth is added that is wider than

the upper teeth. This ensures unlocking by hiding the upper teeth when the loop is shrinking. Otherwise, the teeth are likely to interfere with the ratchet when unlocking. Figure 4.12 shows a ratchet and a latch with an added row of teeth. Figure 4.13 is the physical ratchet latch. Figure 4.14 shows the modified ratchet latch for better latching.

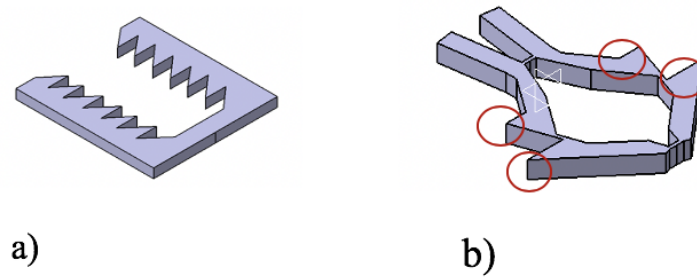


Figure 4.12: Second design of four-bar linkage with modified ratchet and teeth (a) ratchet, and (b) two rows of teeth.

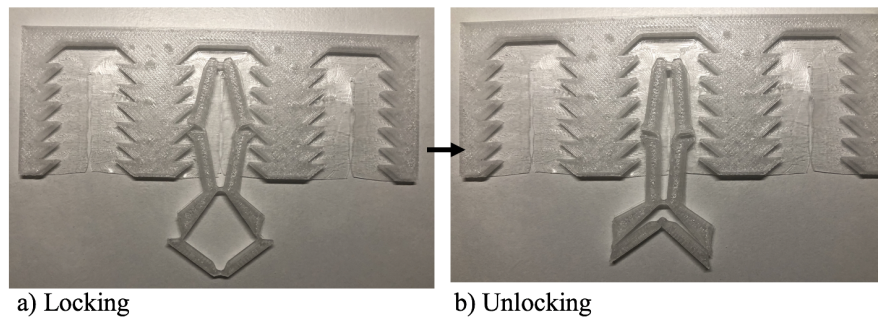


Figure 4.13: Physical ratchet latch.

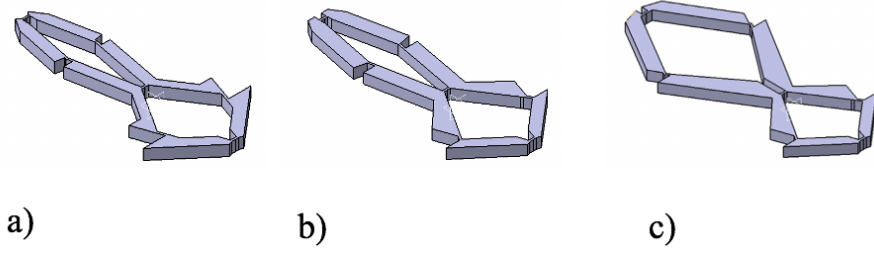


Figure 4.14: Modified ratchet latch.

4.3.3 Theoretical Equations of a 2D Compliant Mechanism

Since the length of the flexure is small, being around 2 mm compared to the length of rigid segments being about 20 mm, the flexure itself is modeled as a short-beam pseudo rigid body (PRB) model with a torsional spring on the joint in the middle (see Figure 4.15). The torsional spring will represent the deformation of the flexure. The stiffness of the torsional spring is defined by $\frac{E \cdot I}{l}$ where E is the modulus of elasticity of flexure, I is the moment of inertia and l is the length of the flexure. The connections of the short beam with adjacent beams are fixed, so the length of the links of the pseudo rigid body is defined. For example, the length L_2 is the sum of the length of rigid segment 2 and two times half of the length of flexure 1 and flexure 3. When extracting the slider rocker model from the latch sketch, details of converting the link length are omitted. The position of torsional spring is approximately at the center of the flexure. Figure 4.15 shows the complete model from one stable position (initial position, i.e., fabrication position) to another stable position (actuated position).

A symmetric 2D compliant mechanism can be simplified as a symmetric slider-rocker four-bar linkage with four torsional springs on the joints mirrored at a shared

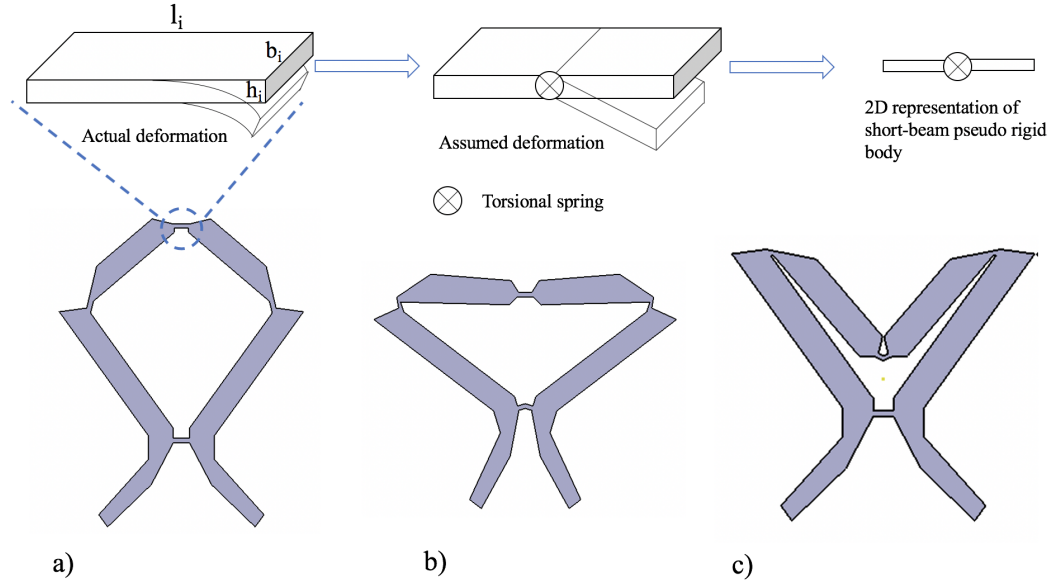


Figure 4.15: Short-beam pseudo rigid body illustration and physical latch in (a) stable position, also the initial position, (b) instable position, and (c) second stable position after snap-through.

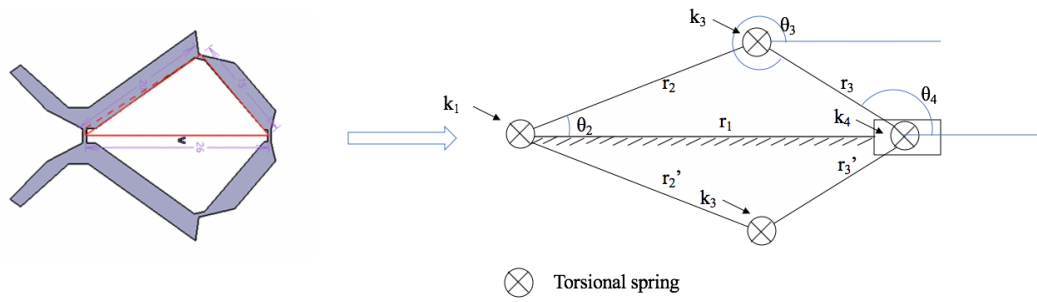


Figure 4.16: Slider rocker mechanism abstraction: four-torsional-spring assumption.

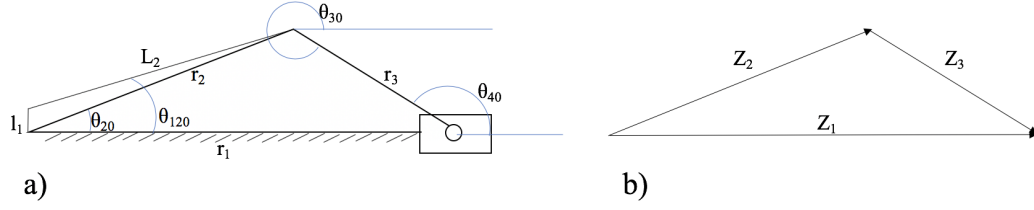


Figure 4.17: (a) Initial angle position, and (b) vector loop.

ground link and a shared slider. Figure 4.16 illustrates the modified slider rocker mechanism.

The length of each link is measured from the sketch of the latch. Based on geometric constraints, the equivalent length of link 2 (r_2) in slider-rocker four-bar linkage is

$$r_2 = \sqrt{((L_1 + L_2 * \sin(\theta_{120}))^2 + (L_2 * \cos(\theta_{120}))^2)},$$

where r_2 and r'_2 are equal, and r_3 and r'_3 are equal based on symmetry; L_1 is half the length of flexure 1; L_2 is the length of link 2 and θ_{120} is the angle between L_2 and r_1 . The undeformed position is shown in Figure 4.17 a); r_3 is the length of link 3.

The values of latch parameters are listed in Table 4.9. The angles are defined from the right horizontal direction to the link direction defined in Figure 4.17 b), and the generalized vector loop equation is

$$\vec{Z}_1 + \vec{Z}_2 = \vec{Z}_3, \quad (4.1)$$

where Z_i represents link i , $i = 1, 2, 3$.

First, the position analysis will give the relationship between unknown angles and position of the slider. Solving vector loop equations in Equations 4.2 and 4.3 will give

Table 4.9: Dimensions of slider-rocker mechanism.

Properties	Value	Unit
E	1.7E9	Pa
l_1	2.00E-3	m
l_3	1.56E-3	m
l_4	2.075E-3	m
L_1	l1/2	m
L_2	16.80E-3	m
L_3	14.59E-3	m
r_{10}	25.716E-3	m
b	3E-3	m
h_1	0.5E-3	m
h_3	0.6E-3	m
h_4	0.569E-3	m
θ_{20}	32.856	°
θ_{120}	29.99	°
θ_{30}	319.906	°
θ_{40}	139.90	°

$\theta_4(\theta_3)$ and $r_1(\theta_3)$; Assume θ_3 is the driver. The vector loop equations, which can be decomposed into horizontal and vertical directions, from Figure 4.16 b) are

$$r_2 * \cos(\theta_2) + r_3 * \cos(\theta_3) = r_1, \quad (4.2)$$

$$r_2 * \sin(\theta_2) + r_3 * \sin(\theta_3) = 0, \quad (4.3)$$

where θ_2 is the angle between link 2 and ground; θ_3 is the angle between link 3 and ground, illustrated in Figure 4.16 b).

θ_4 is less than θ_3 by π based on the geometry, calculated as

$$\theta_4 = \theta_3 - \pi. \quad (4.4)$$

From Equation 4.3, $\theta_2(\theta_3)$ is calculated as

$$\theta_2 = \sin^{-1} \left(-\frac{r_3 * \sin(\theta_3)}{r_2} \right). \quad (4.5)$$

Then $r_1(\theta_3)$ is obtained by substituting θ_2 with a function of θ_3 in Equation 4.2.

Next, the velocity analysis will give the relationship between the angular velocities of different links. Angular velocities of link 2, link 3, and the velocity of the slider are denoted as w_2 , w_3 and \dot{r}_1 , respectively. An instance center approach is adopted for velocity analysis. Instance center of rotation, also known as the instantaneous velocity center, is a common point where two or more rigid bodies have the same velocity.

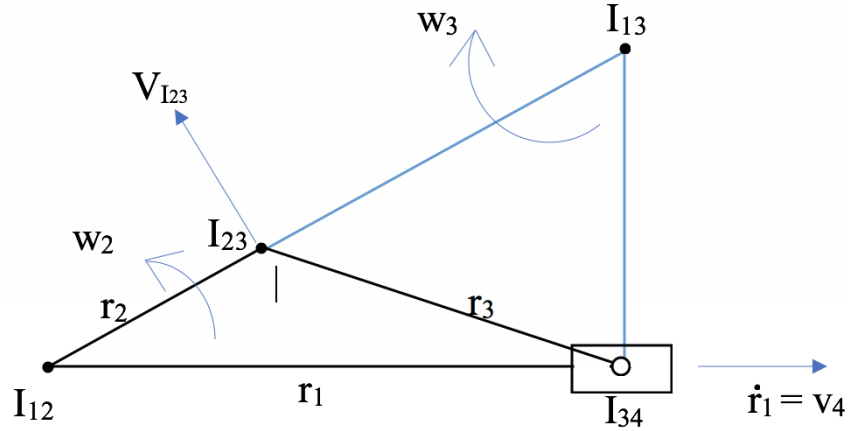


Figure 4.18: Instance center of different links, denoted as I_{ij} , $i, j = 1, 2, 3, 4$.

The joint of two links are the instance center of these links, such as I_{12} , I_{23} and I_{34} . Given that the instance center of three rigid bodies must be on the same line, the position of I_{13} is determined accordingly. Geometric relationships yield

$$|I_{13}I_{34}| = r_1 * \tan(\theta_2), \quad (4.6)$$

$$|I_{13}I_{23}| = \frac{r_1}{\sin(\theta_2) - r_2}. \quad (4.7)$$

The velocity of instance center I_{13} is zero because it is the instance center of link 3 and ground, and that the velocity of the ground is zero. Triangle $\Delta I_{13}I_{23}I_{34}$ is seen as a rigid body with angular velocity of w_3 . I_{23} is the joint of link 2 and link 3, so the velocity of I_{23} can be expressed as

$$V_{I_{23}} = w_2 * r_2 = -w_3 * |I_{13}I_{23}|. \quad (4.8)$$

The rotation direction of link 2 and link 3 is opposite. This explains the negative sign.

The velocity of the slider is expressed as

$$v_4 = w_3 * |I_{13}I_{34}| = \frac{-r_2 * |I_{13}I_{34}|}{|I_{13}I_{23}|} w_2. \quad (4.9)$$

The potential energy (V) of the latch model is the potential energy of four torsional springs. The torsional deflection of each spring can be expressed as:

$$\phi_2 = 2(\theta_2 - \theta_{20}), \quad (4.10)$$

$$\phi_3 = (\theta_2 - \theta_{20}) - (\theta_3 - \theta_{30}), \quad (4.11)$$

$$\phi_4 = 2(\theta_4 - \theta_{40}). \quad (4.12)$$

The potential energy for a complete latch is

$$V = \sum \frac{1}{2} k_i \phi_i^2 = \frac{1}{2} k_1 \phi_2^2 + 2 * \frac{1}{2} k_3 \phi_3^2 + \frac{1}{2} k_4 \phi_4^2. \quad (4.13)$$

If link 3 is actuated by torque T , T is expressed as:

$$T = \frac{\partial V}{\partial \theta_3} = 4k_1(\theta_2 - \theta_{20}) \frac{\partial \theta_2}{\partial \theta_3} + 2k_3((\theta_2 - \theta_{20}) - (\theta_3 - \theta_{30})) \left(\frac{\partial \theta_2}{\partial \theta_3} - 1 \right) + 4k_4(\theta_4 - \theta_{40}) \frac{\partial \theta_4}{\partial \theta_3}, \quad (4.14)$$

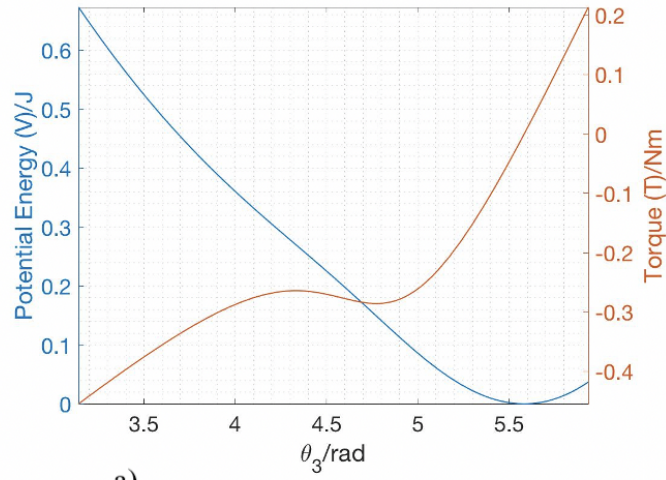
where $\frac{\partial \theta_2}{\partial \theta_3} = \frac{w_2}{w_3}$, $\frac{\partial \theta_2}{\partial \theta_4} = \frac{w_2}{w_4}$.

To ensure the latch is bistable, the potential energy curve has to have two minima representing two stable positions, one of which is the initial position with known initial angle and zero potential energy.

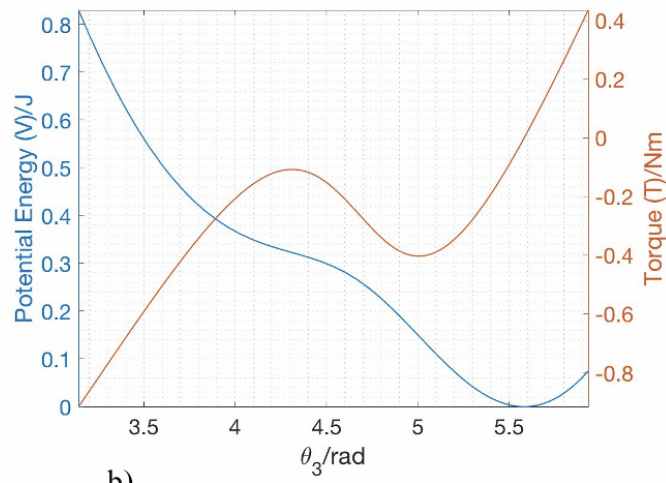
The plot of potential energy (V) and torque (T) is shown in Figures 4.19. Figure 4.19 (a) is obtained using $k_1 = \frac{EI}{L} = 26.6$ Nm/rad. Figure 4.19 (b) and Figure 4.19 (c) used hypothetical $k_1 = 266$ Nm/rad and $k_1 = 2660$ Nm/rad to explore the relationship among k_1 , k_3 and k_4 .

When the torque is zero, the position is stable, and the potential energy is the extreme value. Since T is the first derivative of V , the inflection point on V represents a stable position. The unstable position is the point when torque is the extreme value. It can be seen that when θ_3 is 5.58 rad (319.9°) and 3.84 rad (220.0°), the latch is in a stable position in Figure 4.19 (c). Figure 4.19 (a) and 4.19 (b) do not indicate bistable behavior but as k_1 becomes relatively larger than k_3 and k_4 , bistable behavior occurs at a critical k_1 value before $k_1 = 2660$ Nm/rad.

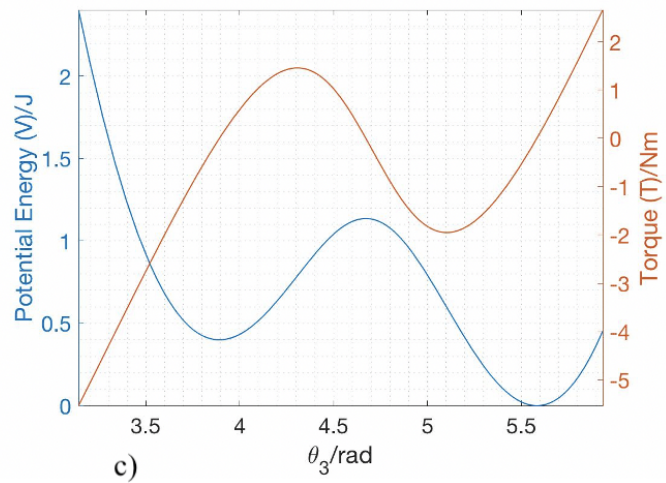
Results show that the spring constant of k_1 has to be much larger than k_3 and k_4 to ensure the existence of bistable behavior. However, k_1 , k_3 and k_4 are on the same scale in calculation and the physical latch is able to snap through. Hence the assumption that all the four flexures bend the same way does not hold true. One reason could be that the rigid segment is actually flexible and it increases the effective k_1 , hence storing potential energy when the latch is deforming. It is also possible that flexure 3, 3' and 4 do not act like a torsional spring in reality, while flexure 1 stores the most potential energy. Flexure 4 does not snap in along the symmetric axis might reduce energy restoration of k_4 torsional spring.



a)



b)



c)

Figure 4.19: Potential energy (V) versus θ_3 and torque (T) on L_3 versus θ_3 when (a) $k_1 = 26.60$ Nm/rad, (b) $k_1 = 266$ Nm/rad, and (c) $k_1 = 2660$ Nm/rad.

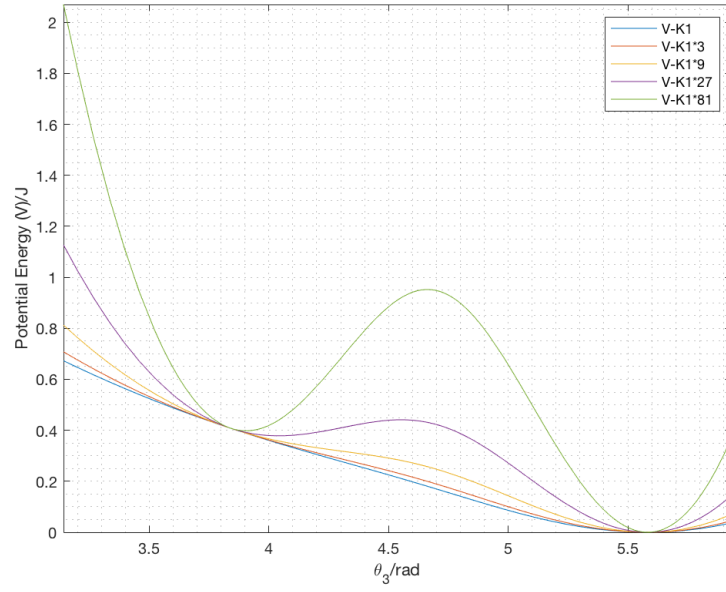


Figure 4.20: Potential energy (V) versus θ_3 - varying k_1 .

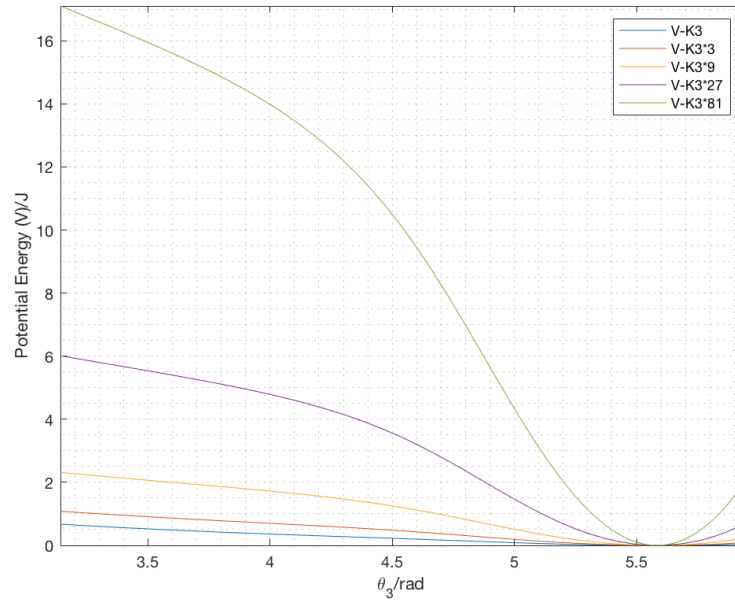


Figure 4.21: Potential energy (V) versus θ_3 - varying k_3 .

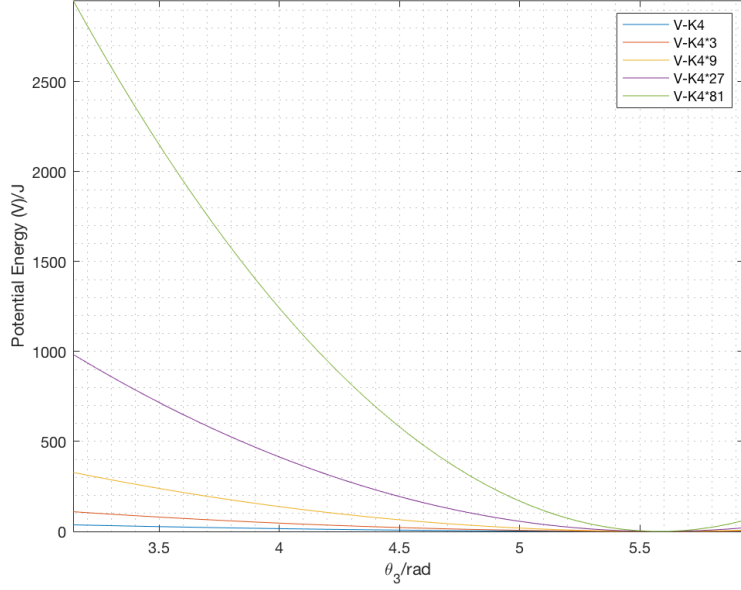


Figure 4.22: Potential energy (V) versus θ_3 - varying k_4 .

Sensitivity analysis is done by varying k_1 , k_3 and k_4 separately and plot their effect on potential energy. Results are presented in Figures 4.20, 4.21 and 4.22 where the basic value of $k_1 = 26.6$ Nm/rad, $k_3 = 58.8$ Nm/rad, $k_4 = 37.7$ Nm/rad, and 3, 9, 27, 81 on the legend are the varying multipliers. It is clear that k_1 is most sensitive among all torsional springs to the potential energy curve. Theoretically, only k_1 of all the torsional springs is capable of determining the trend of potential energy because potential energy stored by k_3 and k_4 is monotonic in the given range of θ_3 .

In this case, to best fit the actual physical latch behavior, a modified model with only one torsional spring connecting r_2 and r'_2 worked well. As illustrated in the DAS-2D symmetric model (see Figure 4.24), if torsional spring 3 and 4 are removed that connect r_2 and r_3 , r_3 and r'_3 , the potential energy of the model has two minima, when θ_3 is at 320° and 220° .

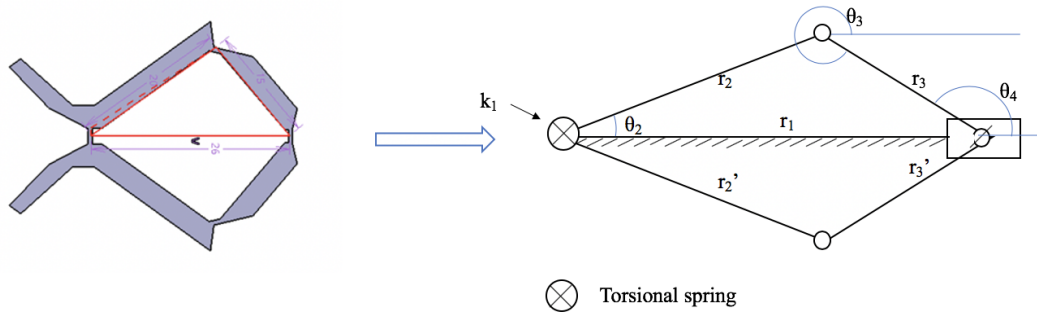


Figure 4.23: Slider rocker mechanism abstraction: one-torsional-spring assumption.

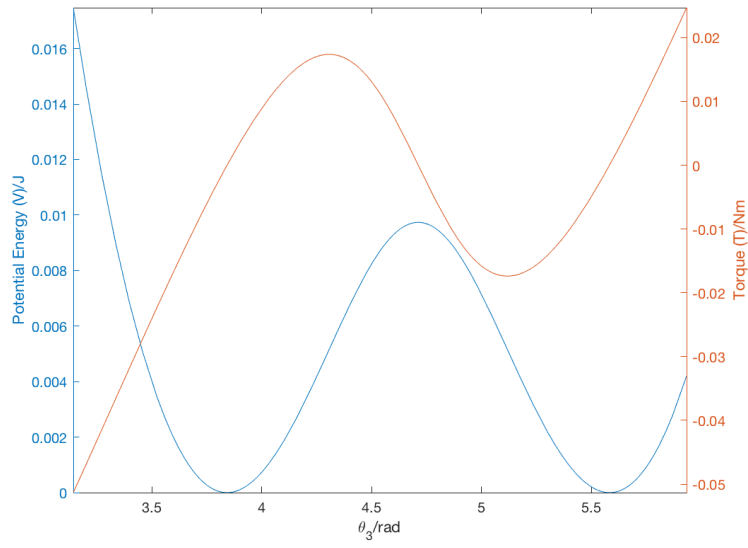


Figure 4.24: Potential energy (V) versus θ_3 and torque (T) on L_3 versus θ_3 - one-spring assumption.

If the latch is driven by force, by principle of virtual work,

$$F * \delta r_1 - \frac{\partial V}{\partial \theta_3} * \delta \theta_3 = 0, \quad (4.15)$$

$$\delta r_1 = \frac{\partial r_1}{\partial \theta_3} \delta \theta_3, \quad (4.16)$$

$$F = \frac{\frac{\partial V}{\partial \theta_3}}{\frac{\partial r_1}{\partial \theta_3}}. \quad (4.17)$$

Figure 4.25 shows the variation of F versus θ_3 . When θ_3 is between 5.58 rad (319.9°) and 4.62 rad (264.7°), the required force to actuate L_3 is small, ranging from -2 N to 4 N.

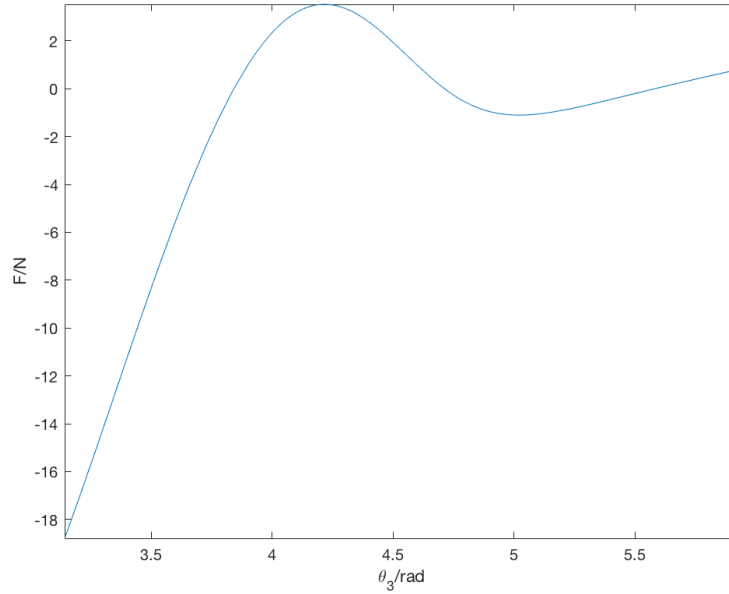


Figure 4.25: Force (F) vs θ_3 .

4.3.4 2D Compliant Mechanism in DAS-2D

Software DAS-2D (Design, Analysis and Synthesis) established by Innovation and Simulation Laboratory at Ohio State University integrates the most recent developed

pseudo rigid body models and synthesis theories for compliant mechanisms. It is a useful tool to evaluate and validate the theoretical model in a faster fashion than other commercial simulation packages.

In DAS-2D, length and angles of r_1 , r_2 and r_3 are the same from Table 4.9. Symmetry is guaranteed by adding an extra link as a ground link (see Figure 4.27). The translation direction of the slider is specified at 0° , which is also the direction of ground link (see Figure 4.29).

First, four torsional springs were added with values previously calculated. Just like plots from the MATLAB calculation, four-torsional-spring assumption did not imply bistability. Even with a simple four-bar linkage assumption of the latch, the potential energy curve still does not indicate bistable behaviors (see Figure 4.27).

After only k_1 was kept, the potential energy curve (see Figure 4.26) indicates bistability and validate the plots from MATLAB in Figure 4.24.

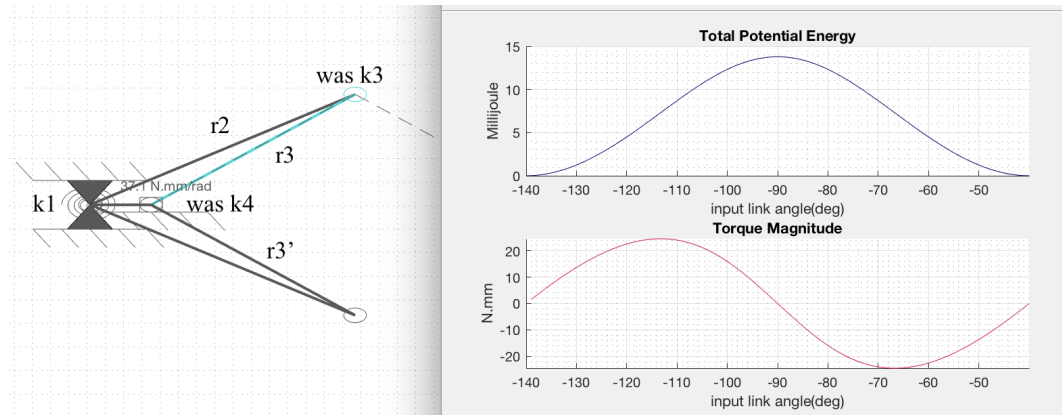


Figure 4.26: Potential energy (V) versus θ_3 and torque (T) on L_3 versus θ_3 - one-spring assumption.

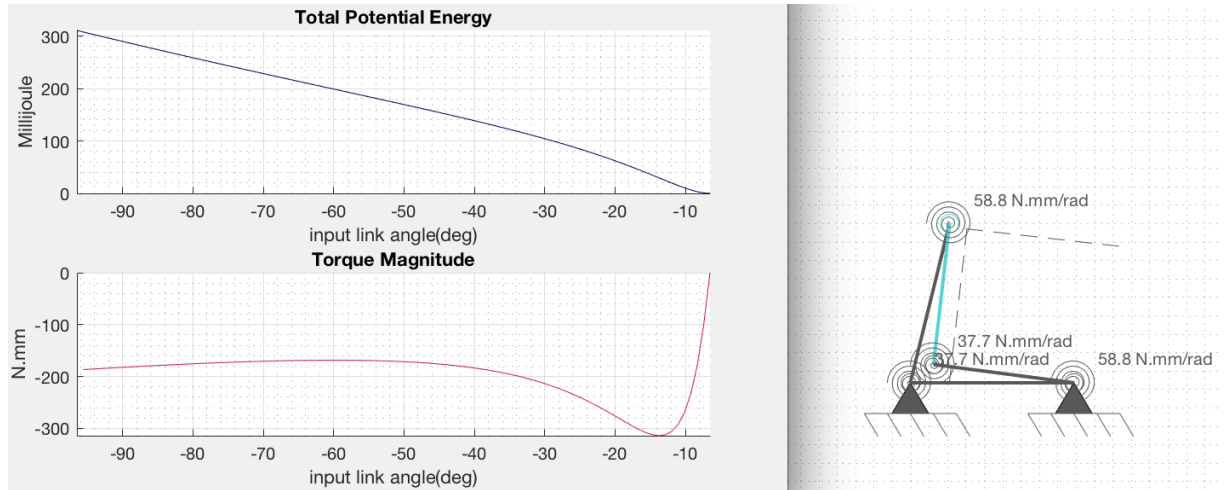


Figure 4.27: Four-bar linkage bistable model (a) potential energy and torque, and (b) deformed position.

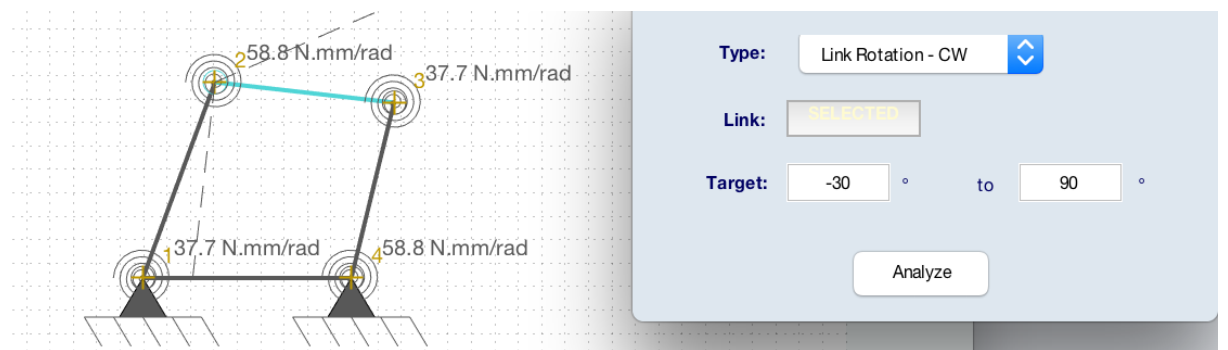


Figure 4.28: Four-bar linkage bistable model - undeformed position.

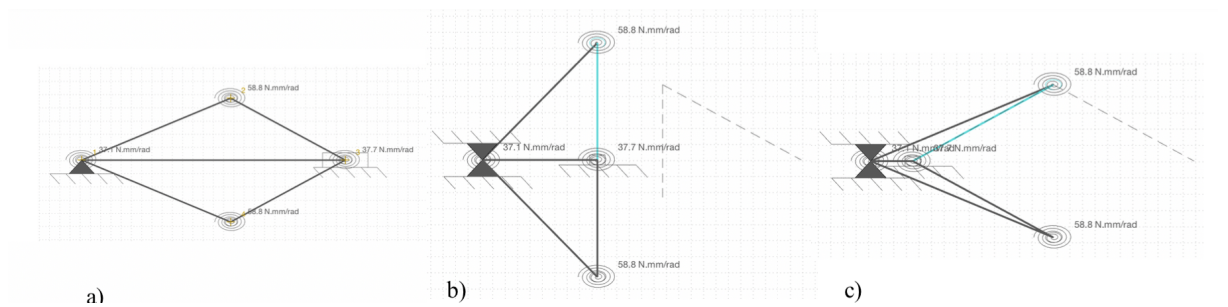


Figure 4.29: Bistable model in (a) stable position 1, also the initial position, (b) unstable position, and (c) second stable position after snap-through.

Chapter 5: Summary and Future Work

5.1 Summary

Concept designs on smart buckle and smart latch using Kevlar fabrics are given to supplement current seat belts.

Studies on material testing of Kevlar and calibration in simulation software LS-DYNA show that the tensile strength reaches 1100 MPa at a strain rate of 3.5% in quasi-static conditions. Kevlar can be modeled using MAT 234 in LS-DYNA with crimp behavior. As a viscoelastic material model, MAT 234 considers the strain rate effect, which can be useful in crash simulations. Coiled fishing line is capable of lifting 3 times its own weight and can contract or expand based on its coiling chirality, therefore makes it an excellent candidate for actuation.

Testing on dual locks shows advantages and disadvantages of plastic and metal dual locks. Metal dual locks are able to endure higher disengagement, almost twice of plastic dual locks, but are less durable with a cycle life of less than 10 times.

Further exploration on compliant mechanisms that gives another option for smart latches. Bistable behavior on a symmetric slider rocker design makes easy locking and fast unlocking possible. Feasibility of bistable mechanism is analyzed on the proposed

design by assuming the flexure a short-beam pseudo rigid body. This assumption is validated with DAS-2D.

5.2 Contributions

Initial concepts of novel restraint systems were brought up to supplement three-point seat belt; properties of Kevlar fabrics were tested and calibrated in LS-DYNA for future use in modeling vehicle crash scenarios; possible smart latch locking mechanisms using metal dual locks and bistable dual locks were prototyped, tested and analyzed.

5.3 Future Work

More work will be done in terms of human model crash simulation, actuation design, origami design and smart latch design.

Crash simulation on the human body model will give a sense of how the designed restraint system works. Human body models of different body dimensions, be it men, women, children, may be examined in LS-DYNA. Also, seating positions and seating angles may be simulated. Modifications can be done easily in simulation without testing numerous trials on cadavers. Material calibration on Kevlar fabric has been done in static fashion, a few adjustments are required based on the crash speed.

Actuation design will be the integration of coiled fishing line or shape memory alloy with the net for deployment. More work can be done on how to precisely control the temperature so that the coiled fishing line is trained to exhibit expansion or contraction predictability.

Origami design is for folding and unfolding of the net so that the net can be manufactured and folded in a smallest possible containment and deploy successfully to a desired position.

The goal of the smart latch design is to lock the net or the seat belt. Material selection and structure design will be done for the smart latch to resist fatigue and high loading. Stress distribution of the smart latch will be investigated.

Appendix A: LS-DYNA Setup

LS-DYNA setup for 2D fabric tensile test LS-PrePost does not specify units. In this study, all the units are SI units by default.

The whole simulation process can be divided into pre-processing, running, and post-processing. Pre-processing and post-processing are done in LS-PrePost, and running is done by submitting the model to a licensed LS-DYNA server.

Pre-processing includes several steps:

1. Decide element type (shell/solid etc.)
2. Mesh (start from coarse mesh)
3. Specify boundary conditions (support, load etc.)
4. Assign materials to part
5. Specify termination time, timestep, hourglass control etc.
6. Specify database output (stress, reaction force etc.) at time intervals

Post-processing includes the following steps.

1. Evaluation animation and energy ratio
2. Validate outputs

A.1 Pre-processing

A.1.1 Mesh-ShapeM

The first step in LS-PrePost is to create element type and specify size. Since the length and the width of Kevlar fabric (200 mm x 50 mm x 0.0254 mm) is much larger than the thickness, 2D shell elements are adopted. Element size of 5 mm in x and y direction is sufficient for a coarse mesh.

For simple geometry, entity can be created in a shape mesher. Otherwise, creating geometry in other CAD software will be a better option. Select ‘4N Shell in Entity’ specify the coordinates of the geometry to be created, usually in counterclockwise order. Specify the number of elements in the x direction and y direction in NxNo and NyNo. Hit Create and check if the mesh is acceptable. If yes, hit Accept and Done. If not, hit Reject and repeat this step.

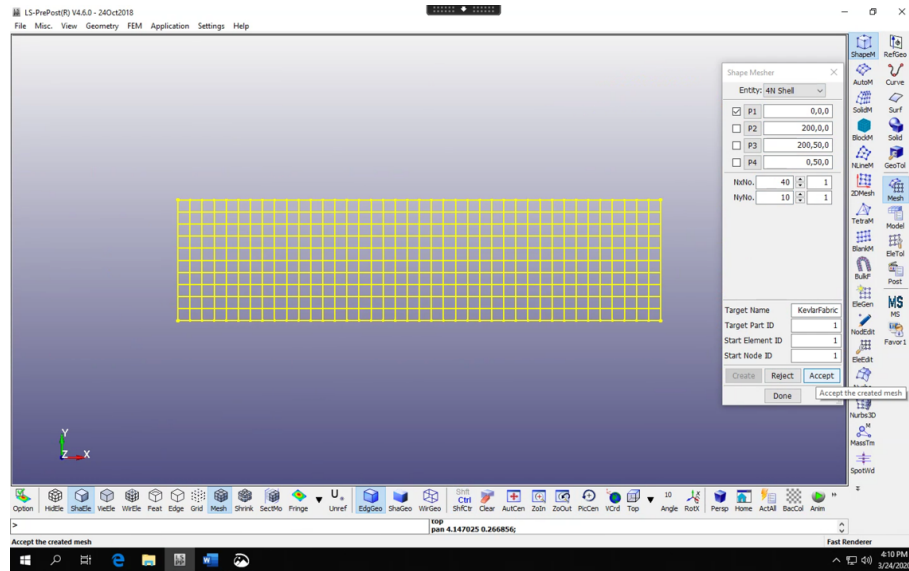


Figure A.1: Select element type and specify geometry

Remesh can be done in Mesh-AutoM after hitting Accept. Also, as the demand for the accuracy of the model improves, remesh is necessary.

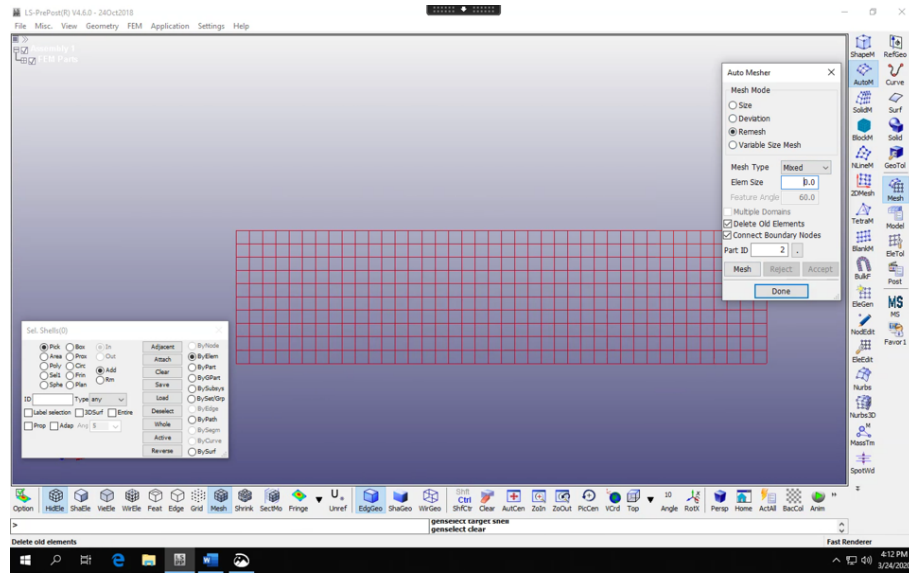


Figure A.2: Remesh

A.1.2 Boundary Conditions

Boundary conditions are defined in Model – CreEnt. Expand Boundary -Spec. Specify Set or Node as the same boundary. Specify each degree of freedom (DOF) of the selected nodes. Hit Apply before hitting Done.

If there are plenty of nodes, set is a better option to manage. Each node inherently has 6 DOF, 3 translational and 3 rotational, in 3D space.

Select VAD = 3 (displacement driven). VAD = 1 is velocity, VAD = 2 is acceleration. Load curve is defined in LCID, explained later.

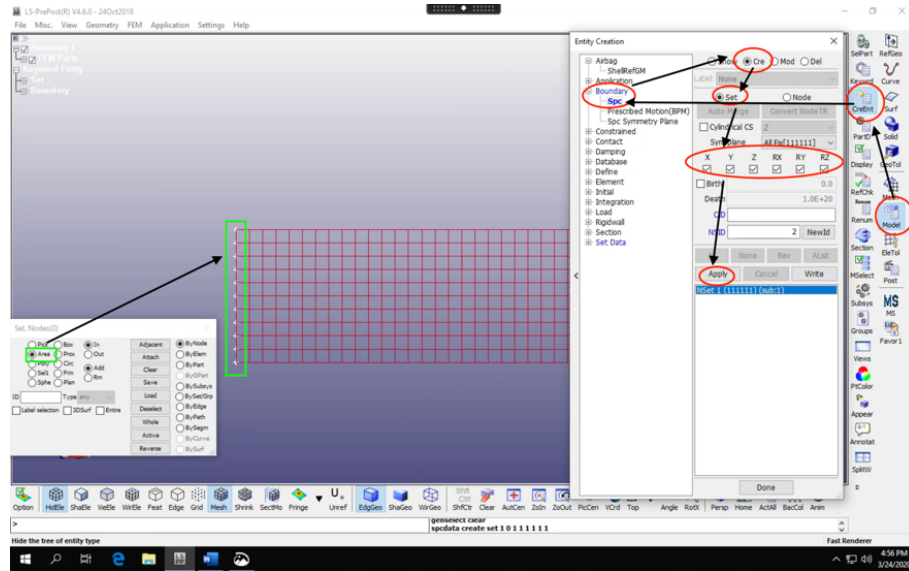


Figure A.3: Create a fixed boundary

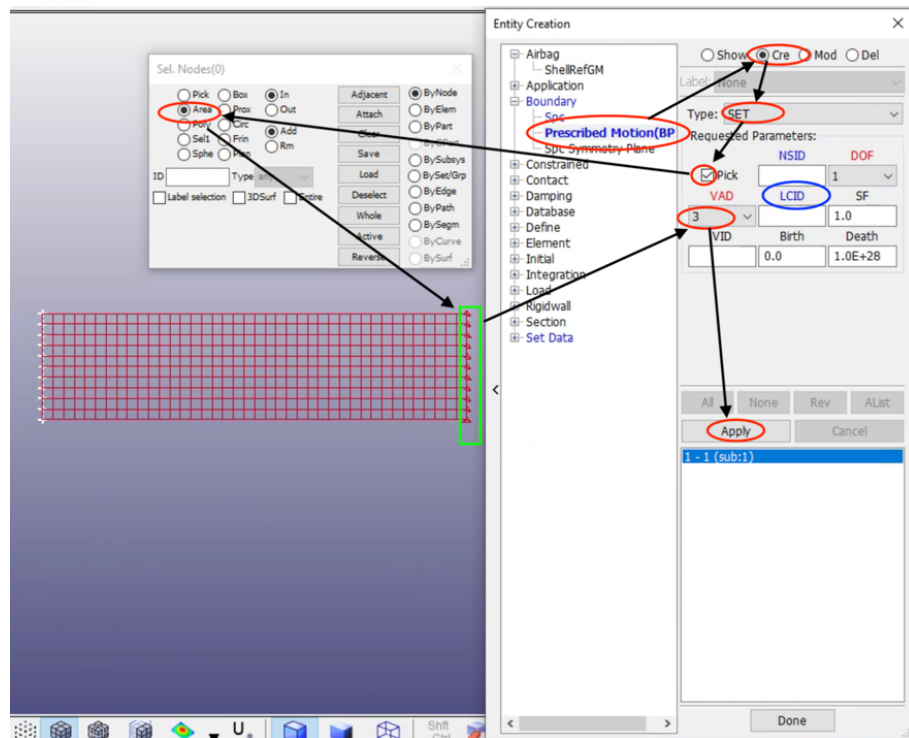


Figure A.4: Create a displacement boundary

Click on LCID, create a new keyword. Define – Curve. The software will automatically assign a load curve ID for the defined curved if the LCID is blank. Type in data points that determines the desired load curve. A1 is x axis. Q1 is y axis. The units are consistent with the desired unit system. Remember to hit insert after every data point. Then hit Accept and Done to return.

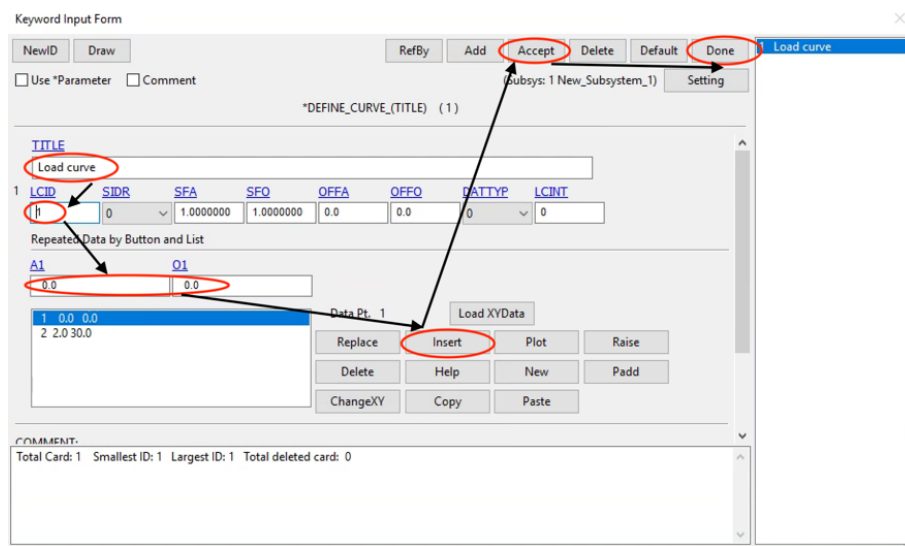


Figure A.5: Define a load curve

A.1.3 Material Type

Select a material type from Manual 2. Kevlar fabric is defined in *MAT234, MAT_VISCOELASTIC_LOOSE_FABRIC. Parameters are defined as follows.

Keyword Input Form

Buttons: NewID, MatDB, RefBy, Pick, Add, Accept, Delete, Default, Done, Setting

Options: ☐ Use *Parameter ☐ Comment (Subsys: 1 11.k)

*MAT_VISCOELASTIC_LOOSE_FABRIC,(TITLE) (1)

TITLE: Kevlar

1	MID	RO	E1	E2	G12	EU	THL	THI
	3	1440.0000	5.800e+10	6.930e+09	1.641e+10	0.0420000	17.000000	45.000000
2	TA	W	S	I	H	S	EKA	EUA
	3.0000000	0.0012446	0.0014940	2.794e-04	1.550e-04	4.500e-08	6.895e+10	0.0330000
3	VMB	C	G23	EKB	AOPT			
	8.618e+06	0.2000000	1.640e+10	2.290e+10	-1			
4	Xp	Yp	Zp	A1	A2	A3		
	0.0	0.0	0.0	0.0	0.0	0.0		
5	V1	V2	V3	D1	D2	D3		
	-0.2588000	0.0	0.9659000	0.0	0.0	0.0		

COMMENT:

Total Card: 1 Smallest ID: 3 Largest ID: 3 Total deleted card: 0

Figure A.6: MAT234 for Kevlar fabric

A.1.4 Control

Determine termination time in Model – keywrd – All – CONTROL - TERMINATION. Set ENDTM to an approximate number and adjust it later based on trial termination time. In this study, $ENDTIM = 0.5$ (sec).

Determine timestep in Model – keywrd – All – CONTROL - TIMESTEP. If not specified, minimum timestep is calculated automatically by the solver. The smaller time step, the faster it solves. However, there is a threshold that the front-line nodes move the front line forward right after calculating the local deformation.

A.1.5 Hourglass Energy

Hourglassing is a state of strain that has zero energy. Hourglass modes are likely to occur if the nodes are not fully integrated and under concentrated loads. *CONTROL_HOURLASS in LS-PrePost inhibits hourglass modes. In default, $IH1 = 1$.

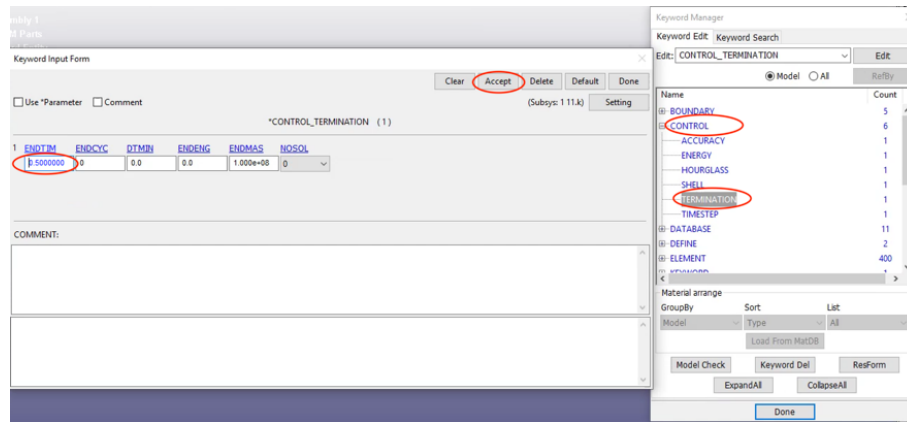


Figure A.7: Define termination time

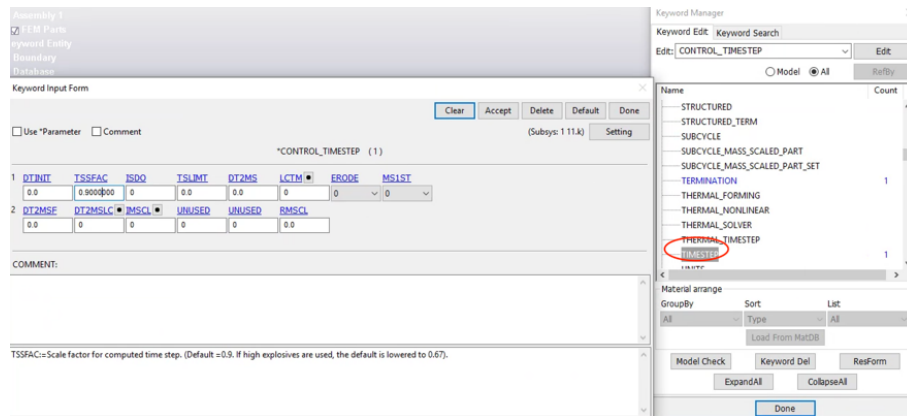


Figure A.8: Define timestep

Fully integrated nodes typically cost more computation resources, so it is a tradeoff between fully integrated and computation costs.

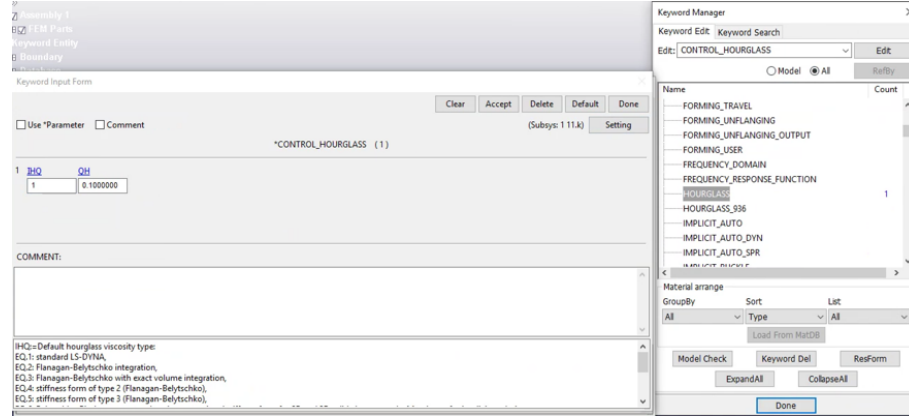


Figure A.9: Hourglass control

A.1.6 Output

For desired output results, click check boxes in *DATABASE_OPTION. DT is the time interval to output data. BINARY = 2, meaning data written to a binary database “binout”, which contains data that would otherwise be output to the ASCII file.

The most common outputs are listed below: ELOUT GLSTAT MATSUM NC-FORC NODFORC

STRFLG is a strain flag to output strain tensor, plastic strain, thermal strain. MSSCL is for checking mass scaling. MSSCL = 2 outputs percentage increase in nodal mass. Mass scaling is a feasible measure to reduce timestep. Although it is not physically correct for the particular points, it is worthwhile to sacrifice a few

nodes for significant improvement in computation time. Identifying the nodes that are impractical in mass is important.

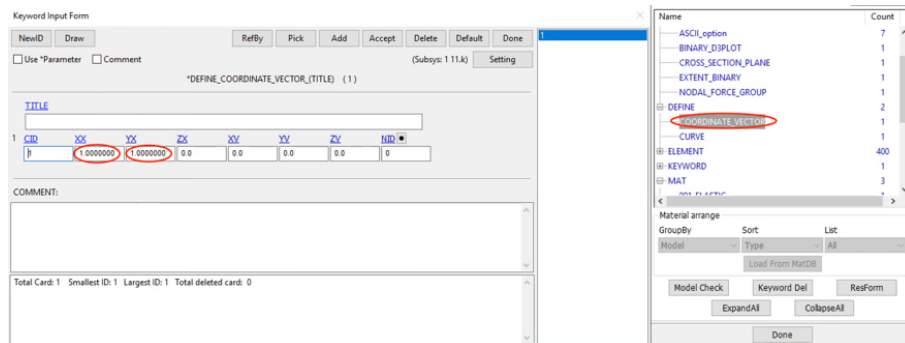


Figure A.13: Define coordinate vector

Coordinate vector is defined for specifying directions such as material directions and element directions. Here, a 45-degree vector from positive x axis is defined to rotate.

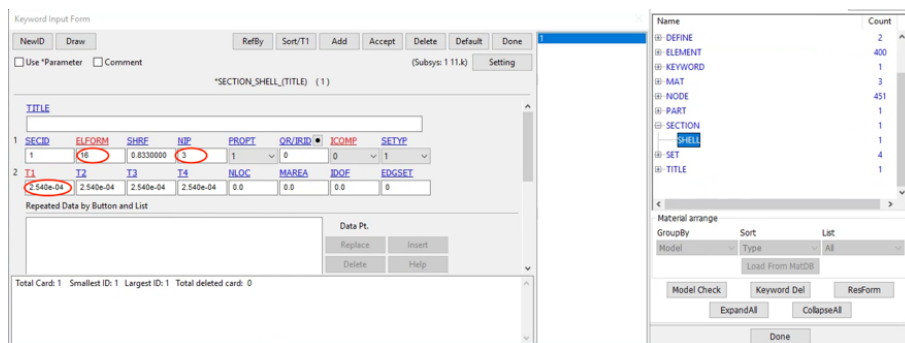


Figure A.14: Define *SECTION_SHELL

The final steps in preprocessing: check if there is large error by Model Check in Keyword Manager. No errors allowed before submitting k file to solver. Warnings could be fine.

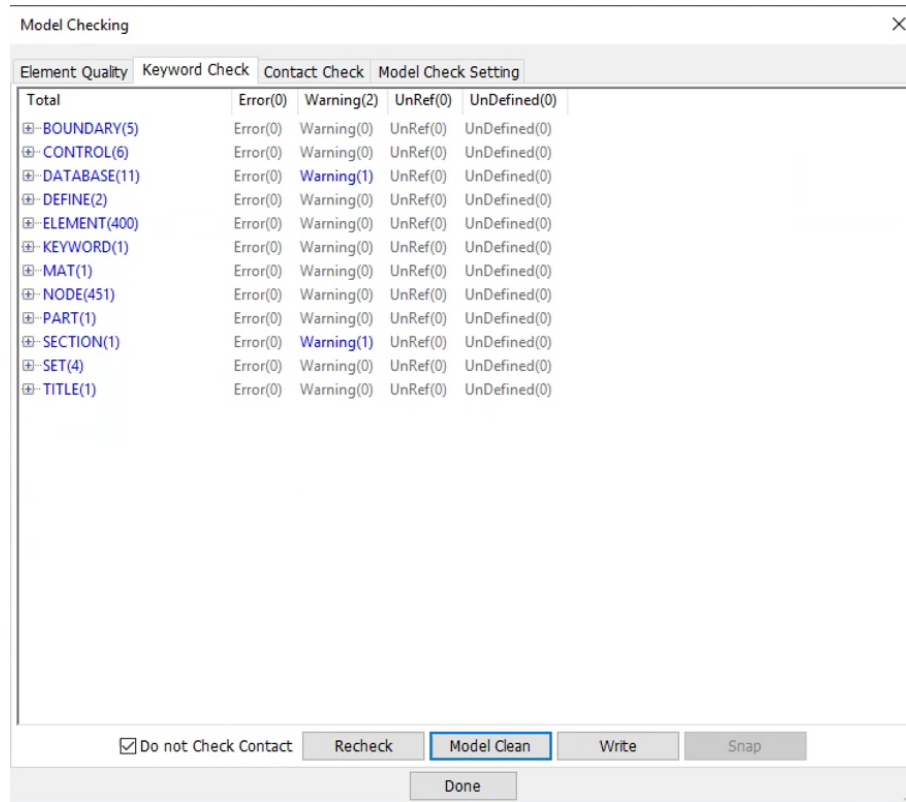


Figure A.15: Model checking

A.1.7 Run the Model

The manuals [16] are the official guide for LS-PrePost setup. Manual 2 is a collection of material types.

Browse the file location to run k file and store database. Set number of CPU (NCPU) to 8, which is the maximum and maximizes CPU resources. Then hit RUN.

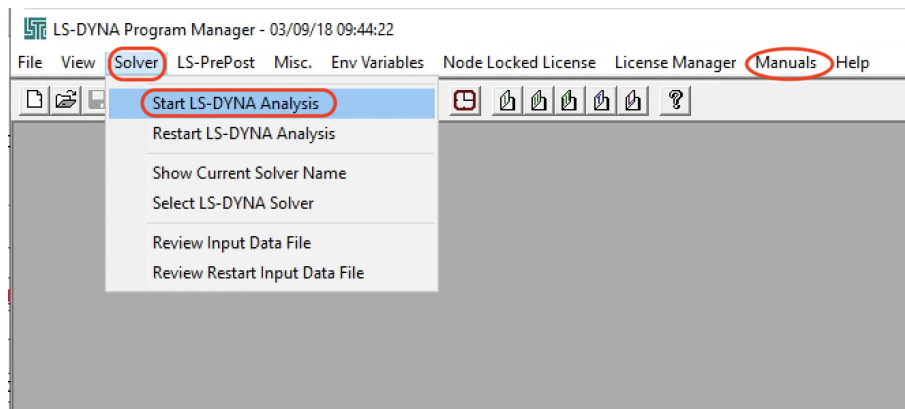


Figure A.16: Start LS-DYNA Solver

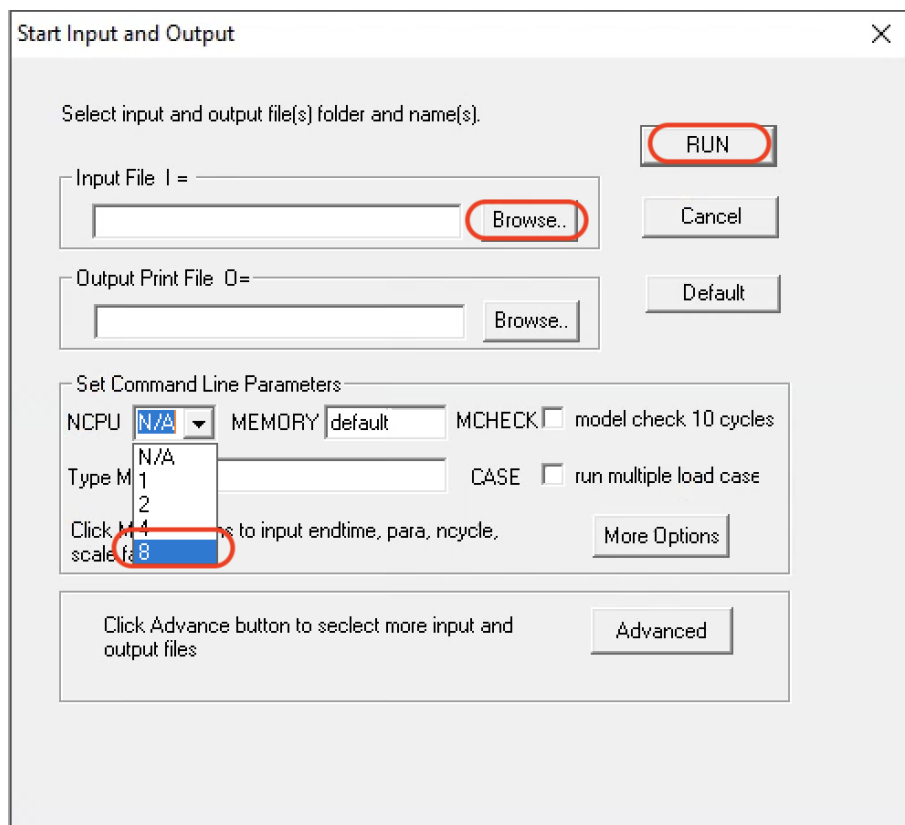


Figure A.17: Select number of CPU utilized

It is a good idea to separate different k files in different folders so that output will not overwrite that of the previous run.

Before normal termination, which may take a while, the d3plot file can be loaded to LS-PrePost for preliminary evaluation and validation.

A.2 Post-processing

The first step of post-processing is evaluation. Observe the animation to check if the simulated process is logical, then evaluate energy ratio. The energy ratio is the total energy after a time frame over initial total energy. According to energy equilibrium, the energy ratio is supposed to be as close to 1 as possible. Energy ratio = 0.998 is acceptable, while energy ratio = 0.5 is unacceptable.

Each time the binout file is updated, it is crucial to load the binout file again. The software will not automatically update the binout file when opening a new/updated d3plot file.

If the energy ratio is far from 1, this means something is wrong. Check energy equilibrium by plotting external work, internal energy, kinetic energy, total energy, hourglass energy etc. and diagnose possible reasons. Invert changes the plot background color to white if it was black.

Tick SetID to see the total resultant force of the moving end. Otherwise, resultant force is for a single node. Total resultant force is the sum of resultant force of each node involved.

Default plot is resultant force versus time. To see the force-displacement curve, save this force-time curve and displacement-time curve, and then replot in Post – X-Y Plot. Make sure the output frequency of force and displacement is the same so

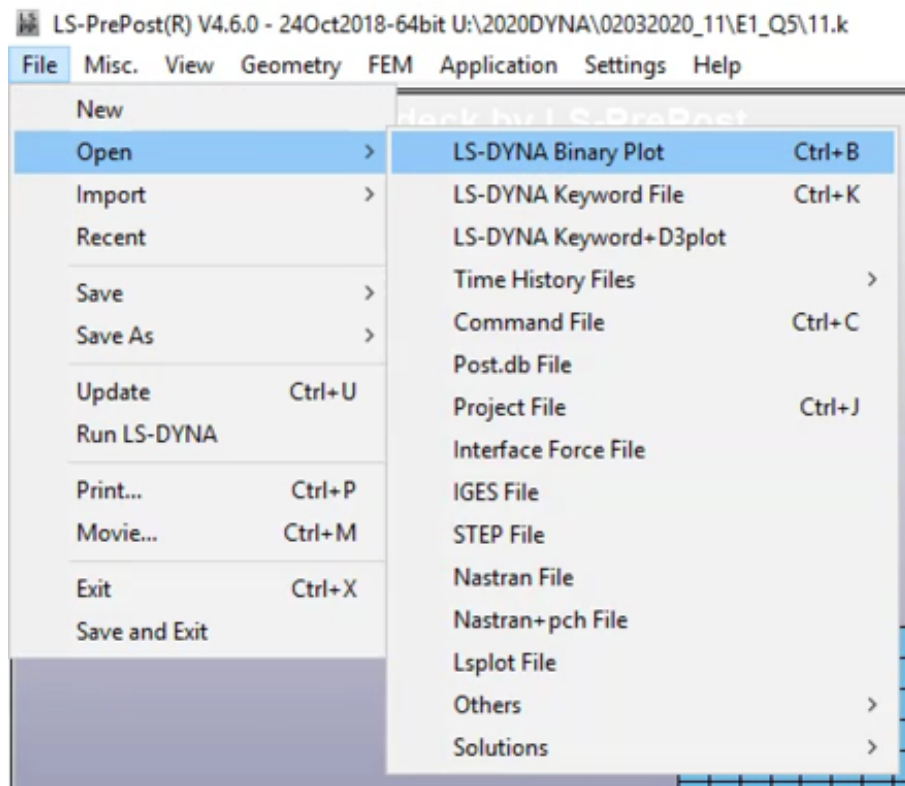


Figure A.18: Open the binary plot

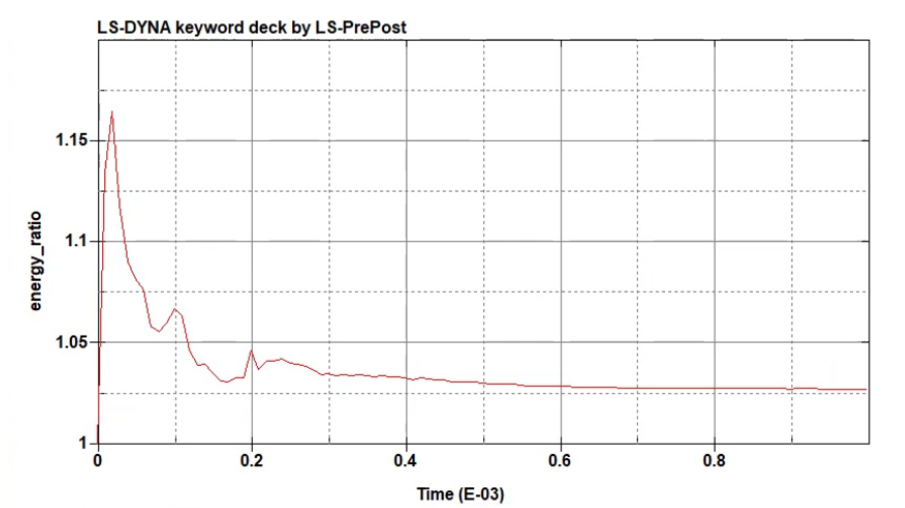


Figure A.19: Check energy ratio

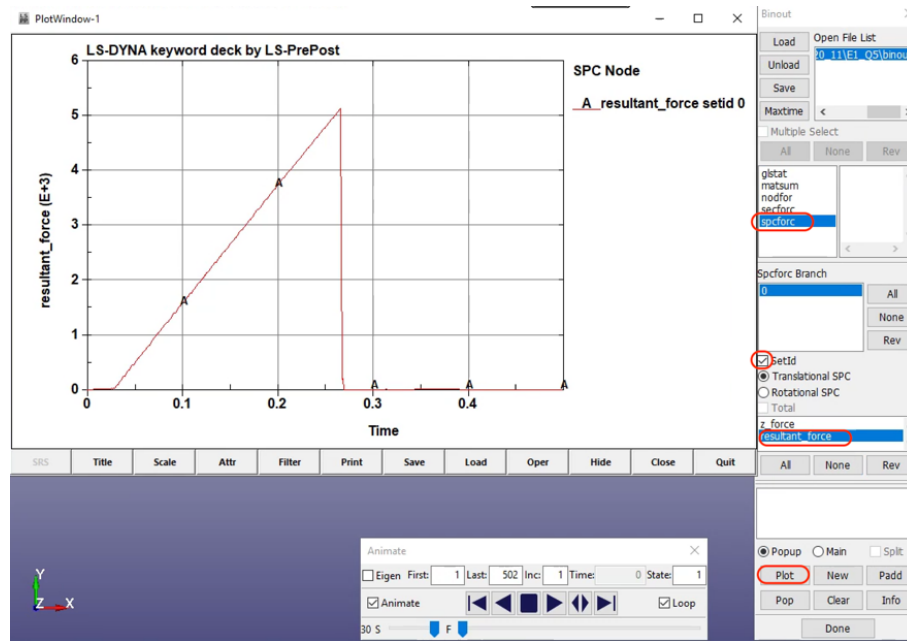


Figure A.20: Plot resultant force

that data points are extracted and stored at the same time. This avoids unnecessary troubles. If the x-y plot does look peculiar, one way to get around is clip each curve at same point and save each curve again and replot x-y.

Post – History stores time relevant output, such as displacement, velocity, acceleration.

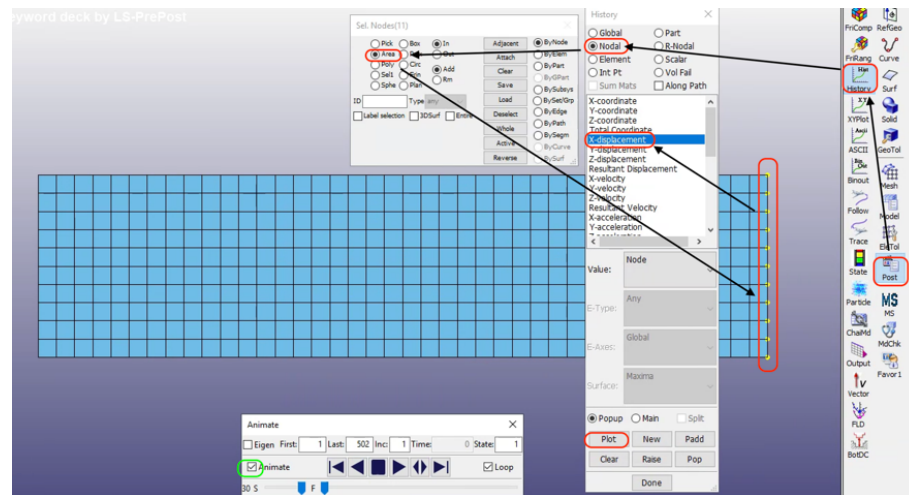


Figure A.21: Plot history data – x displacement of the moving end

Appendix B: MATLAB Calculations

B.1 Cross-sectional Area of Kevlar 49 Yarn

Measurement of Kevlar 49 fabric volume and calculation for cross-sectional area is listed below.

```
1 %% cross-sectional area of Kevlar 49 samples
2 % Size: 200 mm * 50 mm.
3 clc;close all;clear;
4
5 m1 = 11.50; %g
6 m2 = 16.90;
7 m3 = 33.82;
8 m4 = 49.47;
9 mk = m2 - m1
10 me = m4 - mk
11 V2 = 30.0; %ml
12 V3 = 44.1;
13 rou_epoxy = (m4-m3)/(V3-V2)
14 Ve = me/rou_epoxy
15 Vk = V3 - Ve
16 rou_kevlar = mk/Vk
17
18
19 n = 34
20 l_weftyarn = 16*27*2.54; % inch to cm
21 l_warpyarn = 8*n*2.54;% inch to cm
22 l = (l_warpyarn + l_weftyarn) % cm
23
24 L = 60.96; % Length of Kevlar(3 samples), unit: cm, or L = 24inch
25 A = Vk/L*10^-4 %cross-section area, unit: m^2
26 A_yarn = A/n*l_warpyarn/(l_warpyarn + l_weftyarn)
27 A_theory = mk/1.44/L*10^-4/n*l_warpyarn/(l_warpyarn + l_weftyarn)
```

```

28
29
30 %%
31 massDensity = 1228.7; %kg/m^3
32 arealDensity = mk/1000/(3*8*0.0254*2*0.0254)
33 effYarnTk = arealDensity/massDensity
34
35
36 %A = 8.19E-8
37 sig_max = 0.617e9; %Pa, average max stress of testing
38 Ka = 6.895e10; %Pa, elastic stiffness of element a
39 EUA = sig_max/Ka
40 %%
41 L = (432+272)*2.54; % Length of Kevlar(1 samples), unit: cm = ...
    (432+272)inch
42 A_yarn = Vk/3/L*10^-4 %cross-section area, unit: m^2 from cm^2

```

B.2 Potential Energy, Torque and Force Calculation

Measured dimensions of latch design and calculation of potential energy, torque and force are listed below.

```

1 clear;clc;close all;
2 global k1 k3 k4 th20 th30 th40 r2 r3
3 E = 1.7E9; %Pa, modulus of elasticity of PP
4 l1 = 2.00e-3; %m, length of compliant segment
5 l3 = 1.56e-3;
6 l4 = 2.075e-3;
7
8 % Dimensions for rigid segments
9 L1 = l1/2; %m, length of rigid segment after using 1R PRBM
10 L2 = 16.80e-3;
11 L3 = 14.59e-3;
12 r10 = 25.716e-3; % redundant parameter
13
14 % geometry of compliant beam, b is out-of-plane thickness, h is ...
    in-plane thickness, I is area moment of inertia.
15 b = 3e-3;
16 h1 = 0.5e-3
17 h3 = 0.6e-3;
18 h4 = 0.569e-3;
19 I1 = b*h1^3/12;
20 I3 = b*h3^3/12;

```

```

21 I4 = b*h4^3/12;
22
23
24 % stiffness of torsional spring representing short beam
25 k1 = E*I1/l1;
26 k3 = E*I3/l3;
27 k4 = E*I4/l4;
28
29 % angle of undeformed structure
30 th20 = deg2rad(32.856);
31 th120 = deg2rad(29.99);
32 th30 = deg2rad(139.906+180);
33 th40 = deg2rad(139.906);
34
35 % Dimensions for Psudo Rigid Body Model (PRBM)
36 r2 = sqrt((L1+L2*sin(th120))^2 + (L2*cos(th120))^2);
37 r3 = L3;
38
39 syms th3 dVdth3 T F
40     dVdth3 = diffV(th3) % symbolically
41     T = dVdth3;
42     F = diffF(th3);
43
44
45 function dVdtheta3 = diffV(theta3)
46 global k1 k3 k4 th20 th30 th40 r2 r3
47
48     syms theta2 theta4 PHI2 PHI3 PHI4 VV theta22 theta32 theta42 ...
        PHI32 PHI42
49     theta2 = asin(-r3*sin(theta3)/r2);
50     theta4 = theta3 - pi;
51     % Potential energy V. PHI is torsional deflection for each ...
        torsional spring
52     PHI2 = 2*(theta2-th20);
53     PHI3 = (theta2-th20) - (theta3-th30);
54     PHI4 = 2*(theta4-th40);
55     % upper latch, k1*1, k3*2, k4*1
56     VV = k1*PHI2*PHI2/2 %+ 2* k3*PHI3*PHI3/2 + k4*PHI4*PHI4/2
57
58     yyaxis left
59     xlabel('\theta_3/rad');
60     ylabel('Potential Energy (V)/J');
61     set(gcf,'color','w');
62
63     fplot(VV,deg2rad([180 340])); grid minor;hold on;
64
65
66     yyaxis right
67     xlabel('\theta_3/rad');
68     ylabel('Torque (T)/Nm');
69     dVdtheta3 = diff(VV,theta3);

```

```

70     fplot(dvdtheta3,deg2rad([180 340]))
71     set(gcf,'color','w');
72
73 end
74
75 function F = diffF(theta3)
76 global k1 k3 k4 th20 th30 th40 r2 r3
77 syms r1 th2 I13I34 I13I23 T F
78     theta2 = asin(-r3*sin(theta3)/r2);
79     r1 = r2*cos(theta2) + r3*cos(theta3);
80 %velocity analysis
81     I13I23 = r1/sin(theta2) - r2; % distance between instance ...
        center I13 and I23
82
83     % Principle of Virtual Work. (P.O.V.W)
84     dth2dth3 = -I13I23/r2;
85     dr1dth3 = -r2*sin(theta2)*dth2dth3 - r3*sin(theta3);
86
87     dVdth3 = diffV(theta3)
88     F = dVdth3/dr1dth3;
89     figure()
90     set(gcf,'color','w');
91     fplot(F,deg2rad([180 340]));%grid minor;
92     xlabel('\theta_3/rad')
93     ylabel('F/N')
94 end

```

Bibliography

- [1] S. Bansal, B. Mobasher, S. Rajan, and I. Vintilescu. Development of fabric constitutive behavior for use in modeling engine fan blade-out events. *Journal of Aerospace Engineering*, 22(3):249–259, 2009.
- [2] M. Boström, OS, B. Aldman, H. Hansson, Y. Håland, P. Lövsund, T. Seeman, A. Säljö, and T. Örtengren. A new neck injury criterion candidate-based on injury findings in the cervical spinal ganglia after experimental neck extension trauma. In *Proceedings of The 1996 International Ircobi Conference On The Biomechanics Of Impact, September 11-13, Dublin, Ireland*, pages 123–136, 1996.
- [3] C. Chen, C. Chiang, C. Lai, T. Xie, and S. Yang. Buckling-based strong dry adhesives via interlocking. *Advanced Functional Materials*, 23(30):3813–3823, 2013.
- [4] DuPont. Kevlar® aramid fiber: Technical guide. 2000.
- [5] R. Eppinger, M. K, S. Kuppa, R. Saul, and E. Sun. Development of improved injury criteria for the assessment of advanced automotive restraint systems. 1998.
- [6] H. Fang, M. Gutowski, M. DiSogra, and Q. Wang. A numerical and experimental study of woven fabric material under ballistic impacts. *Advances in Engineering Software*, 96:14–28, 2016.
- [7] J. Fein. Improvements in numerical modeling methodology of dry woven fabrics for aircraft engine containment systems. In *Masters Abstracts International*, volume 51, 2012.
- [8] L. Ge, S. Sethi, L. Ci, P. Ajayan, and A. Dhinojwala. Carbon nanotube-based synthetic gecko tapes. *Proceedings of the National Academy of Sciences*, 104(26):10792–10795, 2007.

- [9] E. Giannaros, A. Kotzakolios, G. Sotiriadis, S. Tsantzas, and V. Kostopoulos. On fabric materials response subjected to ballistic impact using meso-scale modeling. numerical simulation and experimental validation. *Composite Structures*, 204:745–754, 2018.
- [10] E. Giannaros, T. Kotzakolios, S. Tsantzas, and V. Kostopoulos. Implementation and calibration of meso-scale modeling technique for simulation of tensile behavior of fabric materials. *Composites Part B: Engineering*, 119:1–9, 2017.
- [11] D. Gierczycka and D. Cronin. Occupant thorax response variations due to arm position and restraint systems in side impact crash scenarios. *Accident Analysis & Prevention*, 106:173–180, 2017.
- [12] A. Gilat and J. Seidt. Recent developments in dynamic testing of materials. In *EPJ Web of Conferences*, volume 26, page 01002. EDP Sciences, 2012.
- [13] C. Haines, N. Li, G. Spinks, A. Aliev, J. Di, and R. Baughman. New twist on artificial muscles. *Proceedings of the National Academy of Sciences*, 113(42):11709–11716, 2016.
- [14] C. Haines, M. Lima, N. Li, G. Spinks, J. Foroughi, J. Madden, S. Kim, S. Fang, M. De Andrade, F. Göktepe, et al. Artificial muscles from fishing line and sewing thread. *Science*, 343(6173):868–872, 2014.
- [15] C. Haines and G. Niemeyer. Closed-loop temperature control of nylon artificial muscles. In *2018 IEEE/RSJ International Conference on Intelligent Robots and Systems (IROS)*, pages 6980–6985. IEEE, 2018.
- [16] J. Hallquist. Ls-dyna® Keyword User’s Manual Volume II Material Models. *Livermore, California, USA*, 2013.
- [17] M. Hassan and S. Meguid. Effect of seat belt and head restraint on occupant’s response during rear-end collision. *International Journal of Mechanics and Materials in Design*, 14(2):231–242, 2018.
- [18] Z. He, H. Xuan, C. Bai, Y. Hu, P. Cong, H. Bai, and W. Miao, Yand Hong. Containment tests and analysis of soft wall casing fabricated by wrapping kevlar fabric around thin metal ring. *Aerospace Science and Technology*, 61:35–44, 2017.
- [19] J. Hill and R. Braun. Implementation of a mesomechanical material model for iad fabrics within ls-dyna. In *AIAA Aerodynamic Decelerator Systems (ADS) Conference*, page 1367, 2013.

- [20] R. Keshavaraj, R. Tock, and D. Haycock. Analysis of fabrics used in passive restraint systems–airbags. *Journal of the Textile Institute*, 87(3):554–571, 1996.
- [21] Y. Kitagawa, S. Hayashi, K. Yamada, and M. Gotoh. Occupant kinematics in simulated autonomous driving vehicle collisions: influence of seating position, direction and angle. Technical report, Stapp car Crash Journal, 31 Oct 2017, 61:101-155 PMID: 29394437.
- [22] M. Komeili and A. Milani. The effect of meso-level uncertainties on the mechanical response of woven fabric composites under axial loading. *Computers & Structures*, 90:163–171, 2012.
- [23] H. Lee, B. Lee, and P. Messersmith. A reversible wet/dry adhesive inspired by mussels and geckos. *Nature*, 448(7151):338–341, 2007.
- [24] J. Madden and S. Kianzad. Twisted lines: Artificial muscle and advanced instruments can be formed from nylon threads and fabric. *IEEE Pulse*, 6(1):32–35, 2015.
- [25] J. Mcloughlin and S. Hayes. Types of fabric and their joining requirements. In *Joining Textiles*, pages 1–44. Elsevier, 2013.
- [26] W. Melbye, S. Nestegard, L. Wood, M. Lindseth, and D. Bychinski. Mushroom-type hook strip for a mechanical fastener, Jan. 7 1992. US Patent 5,077,870.
- [27] B. Michal, E. Spencer, and S. Rowan. Stimuli-responsive reversible two-level adhesion from a structurally dynamic shape-memory polymer. *ACS Applied Materials & Interfaces*, 8(17):11041–11049, 2016.
- [28] A. Muszyński, P. Trzaska, J. Wicher, and Ł. Mazurkiewicz. Analysis of the forces developing in the straps of the belts that restrain a child in a safety seat. *Archiwum Motoryzacji*, 67(1), 2015.
- [29] D. Naik, S. Sankaran, B. Mobasher, S. Rajan, and J. Pereira. Development of reliable modeling methodologies for fan blade out containment analysis–part i: Experimental studies. *International Journal of Impact Engineering*, 36(1):1–11, 2009.
- [30] G. Nilakantan. Filament-level modeling of kevlar km2 yarns for ballistic impact studies. *Composite Structures*, 104:1–13, 2013.
- [31] C. Pang, T. Kim, W. Bae, D. Kang, S. Kim, and K. Suh. Bioinspired reversible interlocker using regularly arrayed high aspect-ratio polymer fibers. *Advanced Materials*, 24(4):475–479, 2012.

- [32] M. Plooiij, G. Mathijssen, P. Cherelle, D. Lefeber, and B. Vanderborght. Lock your robot: A review of locking devices in robotics. *IEEE Robotics & Automation Magazine*, 22(1):106–117, 2015.
- [33] P. Prasad. Injury criteria and motor vehicle regulations. In *Accidental Injury*, pages 793–809. Springer, 2015.
- [34] H. Saleh. *Polyester*. BoD–Books on Demand, 2012.
- [35] D. Sameoto, H. Sharif, and C. Menon. Investigation of low-pressure adhesion performance of mushroom shaped biomimetic dry adhesives. *Journal of Adhesion Science and Technology*, 26(23):2641–2652, 2012.
- [36] K. Schmitt, M. Muser, F. Walz, and P. Niederer. N km—a proposal for a neck protection criterion for low-speed rear-end impacts. *Traffic Injury Prevention*, 3(2):117–126, 2002.
- [37] M. Seong, H. Park, I. Hwang, and H. Jeong. Strong and reversible adhesion of interlocked 3d-microarchitectures. *Coatings*, 9(1):48, 2019.
- [38] D. Shockey, D. Erlich, and J. Simons. Improved barriers to turbine engine fragments: Interim report III. Technical report, SRI International, 2001.
- [39] D. Tria, L. Hemmouche, A. Allal, and A. Benouali. Experimental and numerical analysis of high and low velocity impacts against neat and shear thickening fluid (stf) impregnated weave fabrics. In *EPJ Web of Conferences*, volume 183, page 01044. EDP Sciences, 2018.
- [40] Y. Wang, H. Hu, J. Shao, and Y. Ding. Fabrication of well-defined mushroom-shaped structures for biomimetic dry adhesive by conventional photolithography and molding. *Journal of Adhesion Science and Technology*, 6(4):2213–2218, 2014.
- [41] B. Y. *General Motors announces first center mounted airbags (w/ video)*, 2011. <https://phys.org/news/2011-10-motors-center-mounted-airbags-video.html>.
- [42] S. Yang, E. O’Cearbhaill, G. Sisk, K. Park, W. K. Cho, M. Villiger, B. Bouma, B. Pomahac, and J. Karp. A bio-inspired swellable microneedle adhesive for mechanical interlocking with tissue. *Nature Communications*, 4(1):1–10, 2013.
- [43] L. Zaseck, C. Chen, J. Hu, M. Reed, and J. Rupp. The influence of pre-existing rib fractures on global human body models consortium thorax response in frontal and oblique impact. *Journal of Biomechanics*, 69:54–63, 2018.

- [44] Z. Zhao, L. Liu, W. Chen, and G. Luo. Numerical simulation methodology of multi-layer kevlar 49 woven fabrics in aircraft engine containment application. *International Journal of Crashworthiness*, 24(1):86–99, 2019.
- [45] D. Zhu, B. Mobasher, A. Vaidya, and S. Rajan. Mechanical behaviors of kevlar 49 fabric subjected to uniaxial, biaxial tension and in-plane large shear deformation. *Composites Science and Technology*, 74:121–130, 2013.
- [46] A. Zulifqar, M. UMAIR, K. SHAKER, D. BAITAB, Y. NAWAB, and M. Maqsood. Investigation of multi-layered woven car seatbelts with optimum performance. *DE REDACTIE*, page 77, 2017.